VILNIUS UNIVERSITY

CENTRE FOR PHYSICAL SCIENCES AND TECHNOLOGY

SAULIUS KAZLAUSKAS

CHARGE CARRIER RELAXATION IN FLUORITE-STRUCTURED OXYGEN
ION CONDUCTORS

Doctoral dissertation

Physical Sciences, Physics (02 P)

Vilnius 2015

The dissertation was prepared at Vilnius University in 2011-2015.

VILNIAUS UNIVERSITETAS

FIZINIŲ IR TECHNOLOGIJOS MOKSLŲ CENTRAS

SAULIUS KAZLAUSKAS

KRŪVININKŲ RELAKSACIJA FLUORITO STRUKTŪROS DEGUONIES
JONŲ LAIDININKUOSE

Daktaro disertacija

Fiziniai mokslai, fizika (02 P)

Vilnius 2015

Disertacija rengta 2011 – 2015 metais Vilniaus universitete.

Mokslinis vadovas – doc. dr. Algimantas Kežionis (Vilniaus universitetas, fiziniai mokslai, fizika – 02 P).

Acknowledgements

Contents

Abbreviations

AC: Alternating current.

BIMEVOX: Bismuth metal vanadium oxide.

CaSZ: Calcia-stabilized zirconia.

CPE: Constant phase element.

DC: Direct current.

DRT: Distribution of relaxation times.

DRT function: DRT function of charge carrier.

DTA: Differential thermal analysis.

GA: Genetic algorithm.

GDC: Gadolinia-doped ceria.

GP: Genetic programming.

IS: Impedance spectroscopy.

LAMOX: Lanthanum molybdenum oxide.

LSCF: Lanthanum strontium cobalt ferrite.

MC: Measuring capacitor.

MMC: Model of measuring circuit.

RMS: Root Mean Square.

ScSZ: Scandia-stabilized zirconia.

SEM: Scanning electron microscopy.

SOFC: Solid oxide fuel cell.

XRD: X-ray diffraction.

YSZ: Yttria-stabilized zirconia.

Introduction

Solid electrolytes are materials exhibiting high ionic and negligible electronic conductivities. Focus of this thesis is oxygen ion conductors with fluorite type crystal structure, which are the most extensively studied solid electrolytes because of their applications in solid oxide fuel cells (SOFCs), oxygen pumps and other solid state electrochemical devices. Fluorite-structured oxygen ion conductors usually have a function to transport oxygen ions from anode to cathode and vice versa.

Solid electrolytes in SOFC must possess stability in reducing and oxidising environments, good thermal stability, high ionic conductivity, etc. One of the most difficult challenges is high ionic conductivity. The conductivity of oxygen ion conductors is thermally activated and, consequently, elevated temperatures of 600-1000 °C are required to provide sufficient ionic conductivity. High operating temperature of SOFCs and other devices places severe demands on the materials used for its construction and brings a bunch of other problems.

A number of fluorite-structured oxygen ion conductors is limited and the existing ones have been extensively investigated for several decades. Many efforts have also been made for the improvement of their ionic conductivity. Effects of dopant concentration and processing on electrical properties have been comprehensively studied in the literature. However, the characterization of electrical properties of oxygen ion conductors is challenging as it requires specialized measurement equipment. Most of practical applications utilize electrolytes in the form of polycrystalline ceramics, which are made of many small grains and amorphous glasses or other impurities at the grain boundary medium. Conductivity relaxation processes, occurring within the bulk (often also referred to as grain interior) and grain boundary (also referred to as intergrain) medium of oxygen ion conducting ceramics, have different characteristic time constants and are exhibited at different frequencies. Therefore, impedance spectroscopy (IS) measurements in broad frequency range are needed in order to separate and quantify contributions of bulk and grain boundary medium.

Moreover, even the obtained spectra of electrical properties (i.e. admittance, impedance, electric modulus and permittivity) of solid oxygen ion conductors require further analysis and interpretation. E.g., equivalent circuit fitting, which is one of the most common methods for analysis of raw IS data, requires development of a circuit, the elements of which would represent physical processes occurring in the system under study. It means that this method requires certain a priori knowledge and is adequate only for processes clearly separated in frequency.

In recent years an alternate method has been increasingly used, which bypasses the above mentioned shortcomings. It is based on analysis of dispersion regions of electrical properties, which generally occur as a result of charge carrier relaxation in electrical field. The relaxation times of charge carrier in real materials always have a certain distribution, the shape of which in case of fluorite-structured oxygen ion conductors is close to Gaussian. Width, standard deviation and other characteristics of the distribution of relaxation times (DRT) of charge carrier yield information about its dynamics in the investigated materials.

Numerous relaxation process studies have been performed for various dielectric and conductive systems. However, there have been very few works dealing with frequency response of charge relaxation in fluorite-structured oxygen ion conductors. The main cause of this may have been absence of adequate measurement technique, which would be able to perform high quality IS measurements in broad temperature and frequency ranges.

However, recently a unique measurement technique has been developed at Solid State Ionics laboratory, Vilnius University. It allows broadband impedance measurements at temperatures from room temperature up to 1200 K (maximum tested) and frequencies ranging 100 mHz-~10 GHz [1]. This thesis presents novel data on zirconia (ZrO_2) and ceria (CeO_2) based solid electrolytes, obtained by above mentioned equipment. During the present study, an algorithm for estimation of DRT function of charge carrier from frequency domain impedance data has also been developed. So, the obtained impedance spectra were further analysed in

order to find the DRT function of charge carrier, which further will be called simply DRT function. Combination of novel impedance measurement technique and advanced data analysis tool resulted to original methodology for investigation of oxygen ion conductors, which has potential to be applied to other materials.

In this case advantages of wide frequency and temperature intervals allowed to observe the peculiarities of the DRT function's behaviour with changes in temperature as well as dopant concentration, which were observed in single crystals, bulk and grain boundary medium of ceramics, and even at the vicinity of a structural phase transition in particular ceramic oxygen ion conductor. As it will be shown, these results provided some interesting findings on conduction mechanism in the studied oxygen ion conductors.

Aim and tasks of the work

The aim of this thesis is to estimate behaviour of the DRT function in fluorite-structured oxygen ion conductors.

Tasks of the work are:

1. Estimate the DRT function in oxygen ion conducting yttria-, calcia-, and scandia-stabilized zirconia single crystals and ceramics, as well as in gadolinia-doped ceria ceramics.

2. Determine the effects of temperature and dopant concentration on the DRT function in zirconia- and ceria-based oxygen ion conductors.

3. Determine the DRT function in the vicinity of phase transition in scandia-stabilized zirconia ceramics.

4. Relate the width of the DRT function to directly measurable parameters.

Statements presented for defence

1. The DRT function in oxygen ion conducting ceramics and single crystals can be described by nearly Gaussian curve in logarithmic time scale, the width of which depends on temperature and dopant concentration.

2. Structural phase transition in scandia-stabilized zirconia is accompanied by significant broadening of the DRT function.

3. Width of the DRT function in oxygen ion conductors can be indicated by directly measurable parameters, such as certain characteristic frequencies in electrical modulus and impedance.

Scientific novelty

1. The effects of temperature and dopant concentration on changes in the DRT function in oxygen ion conducting ceramics and single crystals have not been studied up to now.

2. Character of the DRT function was assessed for the first time in the vicinity of structural phase transition in scandia-stabilized zirconia.

3. Two different relaxation processes in the grain boundary medium of 10 mol% gadolinia-doped ceria ceramics were for the first time detected by means of impedance spectroscopy.

4. Relevant relationship was revealed, which relates the directly measurable parameters to the width of the DRT function in oxygen ion conductors.

Articles published in the topic of dissertation

P1. S. Kazlauskas, A. Kežionis, T. Šalkus, A.F. Orliukas, Sintering of oxygen ion conducting ceramics and their electrical properties, Lithuanian Journal of Physics 52(3), 231–237 (2012).

P2. S. Kazlauskas, A. Kežionis, T. Šalkus, A.F. Orliukas, Electrical properties of YSZ and CaSZ single crystals, Solid State Ionics 231, 37–42 (2013).

P3. A. Kežionis, P. Butvilas, T. Šalkus, S. Kazlauskas, D. Petrulionis, T. Žukauskas, E. Kazakevičius, A.F. Orliukas, Four-electrode impedance spectrometer for investigation of solid ion conductors, Review of scientific instruments 84, 013902 (2013).

P4. S. Kazlauskas, A. Kežionis, T. Šalkus, A.F. Orliukas, Charge carrier relaxation in solid $V_O^{\bullet\bullet}$ conductors, Solid State Ionics 262, 593-596 (2014).

P5. S. Kazlauskas, A. Kežionis, E. Kazakevičius, A.F. Orliukas, Charge carrier relaxation and phase transition in scandium-stabilized zirconia ceramics, Electrochimica Acta 134, 176-181 (2014).

P6. A. Kežionis, S. Kazlauskas, D. Petrulionis, A.F. Orliukas, Broadband Method for the Determination of Small Sample's Electrical and Dielectric Properties at High Temperatures, IEEE Transactions on Microwave Theory and Techniques 62(10), 2456-2461 (2014).

P7. S. Kazlauskas, A. Kežionis, T. Šalkus, A.F. Orliukas, Effect of sintering temperature on electrical properties of gadolinia-doped ceria ceramics, Journal of Materials Science 50, 3246-3251 (2015).

P8. A. Kežionis, S. Kazlauskas, D. Petrulionis, A.F. Orliukas, Relationship between charge carrier relaxation and peculiarities of electric response in some solid oxygen ion conductors, Solid State Ionics, *accepted 12 July 2015.*

Author's contribution

In articles [P1-P2], [P4-P5] and [P7] published in the topic of dissertation, the author of the thesis had the main responsibility for preparing the papers. More details are given below.

In [P1] the author of the thesis had the leading role in developing the entire paper, since it was based on his master thesis.

In paper [P2] the author of the thesis performed the measurements of electrical properties of single crystals, contributed to the development of algorithm for estimating the DRT function, and also had the main responsibility for the analysis and interpretation of the experimental results.

During the development of measurement equipment presented in [P3] the author of the thesis was responsible for specific elements of the measurement system, as well as testing of the equipment.

In [P4] this author conducted all the measurements of electrical properties, contributed to the improvement of the algorithm for estimating the DRT function, interpretation of the results and writing of the article.

In [P5] this author carried out most of experimental investigations, had leading role in interpretation of the results, contributed to writing of the article.

During the development of measurement model presented in [P6] the author of the thesis made contribution to the improvement of model of the measuring circuit, as well as to writing of the paper.

In [P7] the author of the thesis carried out all the measurements of electrical properties and had leading role in interpretation of the results and writing the paper.

The author of the thesis carried out all the measurements of experimental data presented in [P8]. The author has also significantly contributed the development of presented method for analysis of results and writing the paper.

Other publications

P9. A.F. Orliukas, O. Bohnke, A. Kežionis, S. Kazlauskas, V. Venckutė, D. Petrulionis, T. Žukauskas, T. Šalkus, A. Dindune, Z. Kanepe, J. Ronis, V. Kunigėlis, Broadband impedance spectroscopy of some Li+ and conducting solid electrolytes, Advanced Electromagnetics 1(1), 70–75 (2012).

P10. E. Kazakevičius, G. Tsekouras, K. A. Michalow-Mauke, S. Kazlauskas, T. Graule, Electronic Conductivity Enhancement of (La,Sr)TiO3 with Nb-Doping on B-Site, Fuel Cells 14(6), 954-960 (2014).

Contributions to conferences

1. S. Kazlauskas, A. Kežionis, A.F. Orliukas, Aukštatemperatūrių deguonies laidžiųjų keramikų gamyba ir jų elektrinės savybės. 39-oji Lietuvos nacionalinė fizikos konferencija: programa ir pranešimų tezės, Vilnius, Lietuva, p. 45 (2011).

2. T. Šalkus, D. Petrulionis, T. Žukauskas, S. Kazlauskas, V. Venckutė, V. Kunigėlis, A. Kežionis, V. Kazlauskienė, J. Miškinis, A.F. Orliukas, Kuro elementų keramikinių elektrodų gamyba ir tyrimas, 39-oji Lietuvos nacionalinė fizikos konferencija: programa ir pranešimų tezės, Vilnius, Lithuania, p. 62 (2011).

3. S. Kazlauskas, A. Kežionis, T. Šalkus, A.F. Orliukas, Electrical properties of YSZ and CaSZ single crystals, 10th International Symposium on Systems with Fast Ionic Transport: book of abstracts, Chernogolovka, Russia, p. 19 (2012).

4. A.F. Orliukas, O. Bohnke, A. Kežionis, S. Kazlauskas, V. Venckutė, D. Petrulionis, T. Žukauskas, T. Šalkus, A. Dindune, Z. Kanepe, J. Ronis, V. Kunigėlis, Broadband impedance spectroscopy of some Li+ and V conducting solid electrolytes, Advanced Electromagnetics Symposium, Paris, France, p. 42 (2012).

5. A.F. Orliukas, A. Kežionis, S. Kazlauskas, V. Kazlauskienė, Miškinis J., Šilėnas A., Petrulionis, D., T. Žukauskas, T. Šalkus, XPS and broadband impedance spectroscopy of some functional materials for SOFC, Fundamental problems of solid state ionics: 11th international meeting, Chernogolovka, Russia, p. 59 (2012).

6. S. Kazlauskas, A. Kežionis, T. Šalkus, A.F. Orliukas, Charge carrier relaxation in solid $V_O^{\bullet\bullet}$ conductors, SSI-19: 19th international conference on solid state ionics, book of abstracts, Kyoto, Japan, p. 99 (2013).

7. S. Kazlauskas, A. Žemaitytė, A. Kežionis, A.F. Orliukas, Effect of sintering temperature and time on ionic conductivity of gadolinia-doped ceria ceramics, Advanced materials and technologies: book of abstracts of the 15-th International Conference-School, Palanga, Lithuania, p. 131 (2013).

8. A. Kežionis, S. Kazlauskas, High temperature ultra-broadband impedance spectrometer. Abstract Book: 6th International Workshop on Impedance Spectroscopy, Chemnitz, Germany, 32-33 (2013).

9. J. Sakaliūnienė, E. Rajeckaitė, T. Šalkus, S. Kazlauskas, A. Kežionis, B. Abakevičienė, S. Tamulevičius, Investigation of structural and electrical properties of YSZ nanopowders and ceramics synthesized by coprecipitation method, SSI - 19: 19th international conference on solid state ionics, book of abstracts, Kyoto, Japan, p. 107 (2013).

10. A. Žemaitytė, S. Kazlauskas, Sintering of gadolinia-doped ceria ceramics and their electrical properties, Open readings = Laisvieji skaitymai: 56th scientific conference for young students of physics and natural sciences: programme and abstracts, Vilnius, Lithuania, p. 147 (2013).

11. S. Kazlauskas, A. Žemaitytė, A. Kežionis, A.F. Orliukas, Gadoliniu legiruoto cerio oksido keramikų sintezės temperatūros įtaka jų joniniam laidumui, 40-oji Lietuvos nacionalinė fizikos konferencija: programa ir pranešimų tezės, Vilnius, Lithuania, p. 71 (2013).

12. A. Kežionis, S. Kazlauskas, J. Krivochiža, T. Žukauskas, A.F. Orliukas, Aukštatemperatūris superplačiajuostis pilnutinės varžos spektrometras, 40-oji

Lietuvos nacionalinė fizikos konferencija: programa ir pranešimų tezės, Vilnius, Lithuania, p. 18 (2013).

13. D. Petrulionis, A. Kežionis, P. Butvilas, T. Šalkus, S. Kazlauskas, T. Žukauskas, E. Kazakevičius, L. Šatas, A.F. Orliukas, Skirtuminis stiprintuvas kietųjų joninių laidininkų matavimui, 40-oji Lietuvos nacionalinė fizikos konferencija: programa ir pranešimų tezės, Vilnius, Lithuania, p. 175 (2013).

14. A. Žemaitytė, S. Kazlauskas, A. Kežionis, Gadoliniu ir samariu legiruotų cerio oksido keramikų gamyba iš nanomiltelių ir elektrinių savybių tyrimas. Studentų moksliniai tyrimai 2012/2013: konferencijos pranešimų santraukos, p. 564-566 (2013).

15. S. Kazlauskas, A. Žemaitytė, A. Kežionis, A.F. Orliukas, Sintering and electrical properties of gadolinium- and samarium-doped ceria, ISSFIT-11: 11th international symposium on systems with fast ionic transport: abstract book, June 25-29, Poland. p. 74 (2014).

16. S. Kazlauskas, A. Kežionis, A.F. Orliukas, Effect of sintering temperature and time on ionic conductivity of samarium-doped ceria ceramics, Advanced materials and technologies: book of abstracts of the 16-th international conference-school, Palanga, Lithuania, 27-31 August, p. 103 (2014).

17. A. Kežionis, S. Kazlauskas, D. Petrulionis, A.F. Orliukas, Pecularities of charge carrier relaxation in some solid oxygen ion conductors, ISSFIT-11: 11th international symposium on systems with fast ionic transport: abstract book, June 25-29, Poland. p. 34 (2014).

1. Literature review

The chapter is divided into four sections, reviewing literature relating to various aspects of fluorite-structured oxygen ion conductors. The first section is devoted to crystal structure, electrical properties, conduction mechanism and other factors. The next two sections review effects of chemical composition and processing on structure and electrical properties of certain zirconia- and ceria-based oxygen ion conductors. The last one, section 1.4, provides an overview of methods and procedures that are being used to extract relevant information from impedance spectra, starting from parameters such as electrical conductivity up to the DRT function.

1.1. Oxygen ion conduction: general considerations

One of the most interesting part of solid electrolytes is oxides that exhibit oxygen ion conductivity with none or negligible electronic contribution to total electrical conductivity.

Fluorite-structured oxygen ion conducting materials have a crystal structure of cubic fluorite AO_2 (A – large tetravalent cation), in which A is surrounded by eight oxygen ions located at the corners of the unit cell, an example of which (ZrO_2) may be found in Fig. 1.1. Defects in the structure are generally generated by substituting A sites with lower valence cations. It introduces the oxygen vacancies to maintain overall charge neutrality. Borrowing terminology from semiconductor technology, this substitution is called as "doping".

Since the formed oxygen vacancies are mobile and can be used to transport oxygen through the material, the oxygen ion conductors sometimes are referred to as oxygen vacancy conductors or simply $V_O^{\bullet\bullet}$ conductors ($V_O^{\bullet\bullet}$ represents oxygen vacancy in Kröger-Vink notation). One should say that in the absence of an electric field, the ions exhibit a random motion from one lattice site to another. By the presence of the applied electric field, the movement of charge carrier is still random, but with a certain drift in the direction parallel to the electric field.
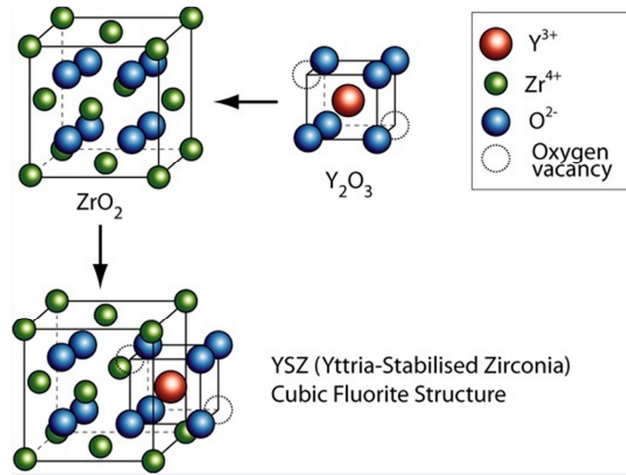
Fig. 1.1. Crystal structure of YSZ [2].

Concentration of charge carrier in the solid oxygen ion conductors is directly related to the concentration of defects. Another requirement for high oxygen ion conductivity is small energy barrier ΔE, called "conductivity activation energy" or simply "activation energy", for migration from an occupied site to unoccupied one. The ionic conductivity of oxygen ion conductor may be described as:

$$\sigma = \mu N q, \tag{1}$$

where μ is charge carrier electrical mobility, N – effective charge carrier concentration, and q – charge for single charge species. The ionic conductivity depends exponentially on the ΔE according to the Arrhenius law:

$$\sigma T = \sigma_0 \exp\left(-\Delta E / k_{\mathrm{B}} T\right), \tag{2}$$

where σ_0 is pre-exponential factor, k_{B} – Boltzmann constant, and T – absolute temperature. In order to obtain high ionic conductivity at low temperatures, the value of activation energy should be as small as possible, preferably less than 1 eV.

Therefore, besides the fluorite, there are only a few particular structures exhibiting considerable oxygen ion conductivity: perovskites and perovskite-related oxides, as well as compounds with so-called LAMOX (lanthanum molybdenum oxide) and BIMEVOX (bismuth metal vanadium oxide) structures. However, the extent of this work will be limited to fluorite-structured oxides,

which comprise solid solutions of oxides of divalent or trivalent cations (i.e. Y_2O_3, Yb_2O_3, CaO) in oxides of tetravalent metals (such as ZrO_2, ThO_2, or CeO_2).

As it was mentioned in the introduction, oxygen ion conductors are generally utilized in the form of polycrystalline ceramics, which are made via sintering of powders with carefully controlled chemical composition and particle size distribution. By sintering the powder compacts are transformed into coherent solids due to mass transport through diffusion. It leads to grain growth, what eliminates the pores and provides well defined grain boundary medium [3]. Due to polycrystallinity of ceramics, its ionic conductivity comprises contributions of bulk and grain boundary medium. While the bulk conductivity seems to be a direct function of the level of aliovalent dopants and the associated oxygen vacancy concentration [4], the literature data on conductivity of grain boundary medium reveal a broad scattering that cannot be easily explained [4, 5]. In general, the oxygen ion conducting ceramics always exhibit smaller specific conductivity than the single crystals due to presence of grain boundary medium. However, the specific conductivity of grain boundary medium is usually difficult to evaluate due to uncertainty in volume fraction of grain boundary medium in the sample. For this reason the specific conductivity of grain boundary medium (σ_{gb}) is often referred to as measured absolute conductivity of grain boundary medium divided by sample dimensions.

The information above covers the main concepts of oxygen ion conduction in solid oxides. It only should be added that there are also more requirements for oxygen ion conductors used in SOFCs, other than stability in various environments, thermal stability and high ionic conductivity, which arise due to their high operating temperatures. These are resistance to thermal shock, compatibility of expansion coefficient with that of an adjacent material, etc. Moreover, reducing of operating temperature of SOFCs below 850 °C gives optimum trade-off between performance and lifetime of the device.

1.2. Effect of chemical composition and processing on structure and electrical properties

The magnitude of ionic conductivity is of great importance when talking about the applications of solid oxygen ion conductors. There are enormous efforts in literature for the improvement of ionic conductivity, and one of the main influencing parameters was found to be chemical composition.

1.2.1. Yttria-, scandia- and calcia-stabilized zirconia

Pure zirconia undergoes two phase transitions between room temperature and its melting point: monoclinic to tetragonal at ~1170 °C and tetragonal to cubic at ~2370 °C (Fig. 1.2). An addition of aliovalent dopants results in stabilization of the cubic phase even up to room temperature, as well as in creation of oxygen vacancies. One of the most common dopants is yttrium: such a compound (general formula $Zr_{1-x}Y_xO_{2-\delta}$) is called "yttria-stabilized zirconia" and noted YSZ. Crystal structure of YSZ and its general phase diagram are presented in Figs. 1.1 and 1.2, respectively. As indicated in Fig. 1.2, 8 mol% yttria is the lowest concentration to stabilize the cubic phase to room temperature. According to the Kröger-Vink notation, the substitution of Y by Zr can be expressed as:

$$Y_2O_3(ZrO_2) \rightarrow 2Y'_{Zr} + 3O_0^X + V_O^{\bullet\bullet}, \tag{3}$$
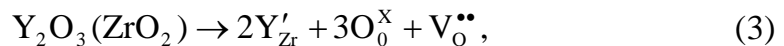
where Y'_{Zr} indicates yttrium ion at zirconium lattice site, with singular negative charge, O_O^X – neutral oxygen ion, and $V_O^{\bullet\bullet}$ – oxygen vacancy with effective charge +2.

It may seem that increase in the dopant level and, consequently, introduction of more vacancies should result in higher conductivity. However, this principle applies only at low concentrations of dopants for fluorite-structured oxygen ion conductors, when the increase in conductivity is due to the increase of the amount of oxygen vacancies. According to the literature data, the ionic conductivity of these materials varies as a function of dopant concentration and shows a maximum at specific concentration (Fig. 1.3). A gradual decrease in conductivity
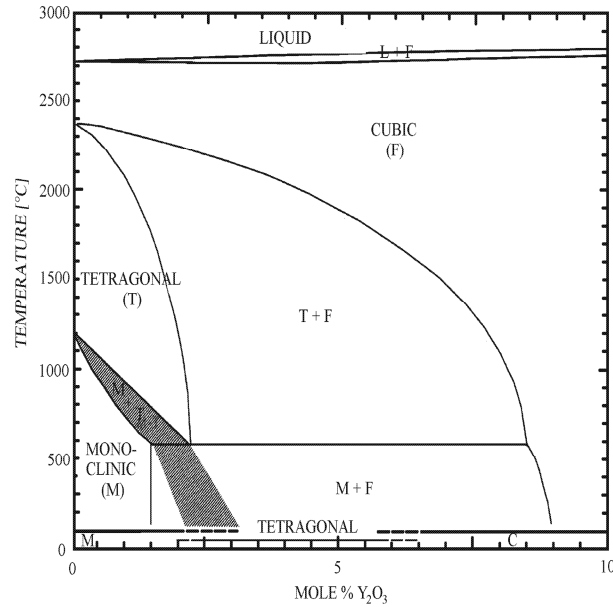
Fig. 1.2. Phase diagram of the system ZrO_2-Y_2O_3 [6].

of YSZ with doping concentration increase is explained by interactions of Y'_{Zr} and $V_O^{\bullet\bullet}$, that results in a higher energy barrier on the path of vacancy jump [7, 8]. An optimum doping level in YSZ system was found to be around 8 mol%, which corresponds to equilibrium between the increase of charge carriers and interactions between the defects.

It should be noted that most of practical applications of oxygen ion conductors require high conductivity of the order of 1 S/m. As denoted by Eq. (2), the magnitude of conductivity increases exponentially with increasing temperature. For example, YSZ exhibits a room temperature conductivity of 10^{-9} S/m [11] and high operating temperature (800-900 °C) is required for YSZ to provide oxygen ion conductivity of 1 S/m. Specifically, the ionic conductivity of 8 mol% YSZ (YSZ8) at 1000 °C is about 10 S/m [12, 13]. Therefore materials, which exhibit sufficient ionic conductivity at lower temperatures, are broadly investigated worldwide.

Other promising zirconia-based electrolytes are zirconia with the additions of Sc_2O_3, Sm_2O_3, CeO_2, CaO, etc. For each dopant, the doping concentration range for stabilizing the cubic phase varies and is temperature dependent. The
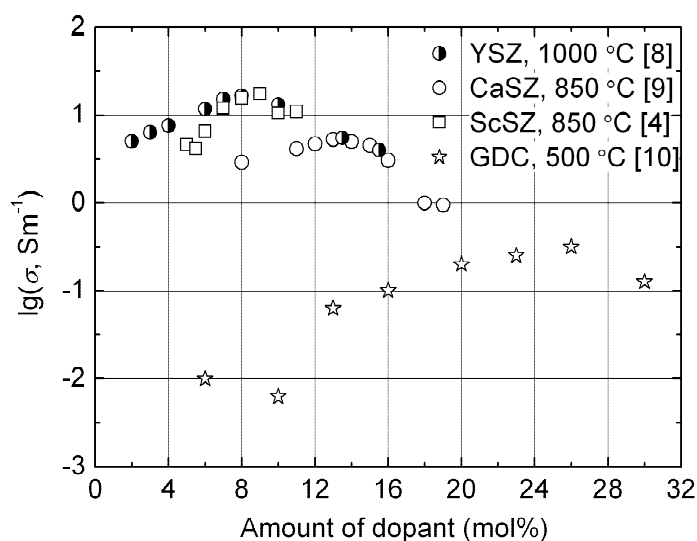
Fig. 1.3. Conductivity variation as a function of dopant content in zirconia- and ceria-based polycrystalline ceramics.

temperature dependent conductivity of most zirconia-based solid electrolytes has been particularly well studied in the literature. It was found that the conductivity of these materials is not only a function of dopant concentration, but also is dependent on ionic radius of the dopants. A number of studies have shown that ionic conductivity of stabilized zirconia depends on the size of dopant cations and tends to be the highest for those with ionic radii close to that of the host Zr^{4+} (0.84 Å) [8, 14]. Indeed, scandia-stabilized zirconia (ScSZ) (Sc^{3+} radii 0.87 Å) shows the highest conductivity among Ca^{2+}, Y^{3+}, Sm^{3+}, etc. [4]. It was suggested that lower mismatch of ionic radii results in lower internal stress in the lattice, which cause lower barrier for the movement of oxygen ions and, consequently, lower activation energy.

ScSZ is a promising material with optimum doping of 8-10 mol% (Fig. 1.3). For example, 9 mol% doped ScSZ ceramics (ScSZ9) exhibits 35 S/m ionic conductivity at 1000 °C [4], which is slightly higher than that of YSZ8 at the same temperature. However, certain ScSZ compositions (9-13 mol% Sc_2O_3) suffers a phase transition from rhombohedral to high temperature cubic phase at around 800-900 K (depending on dopant amount), which is unique for scandia-stabilized

23

zirconia [15]. Thermocycling of such material eventually leads to material degradation. There are reports in the literature that the stabilization of the cubic phase ScSZ in lower temperatures can be achieved by co-doping with small amounts (0.5-1.5 mol%) of other oxides (Gd_2O_3, Y_2O_3, Bi_2O_3 or CeO_2) [16]. Still, the effect of various ternary dopants on this process has not been studied in detail. It should be also noted that the observed phase depends not only on the composition, but also on the preparation method, thermal prehistory and microstructure of ceramics [17]. Combinations of more than one type of dopant are also quite often used to obtain higher conductivities or other specific properties.

Another ordinary zirconia-based solid electrolyte is calcia-stabilized zirconia (CaSZ), which is also extensively studied because of its high conductivity and stability. Charge carrier compensation mechanism in CaSZ is slightly different than that in YSZ. E.g., in YSZ the substitution of Zr^{4+} by Y^{3+} causes formation of oxygen vacancies, the amount of which is equal to half the amount of Y^{3+} ions. Whereas in CaSZ the amount of vacancies is equal to number of Ca^{2+} ions and is twice higher than that in YSZ. Despite the latter fact, CaSZ system shows similar behaviour to that of other stabilized-zirconia systems. According to the literature data, ionic conductivity of CaSZ exhibits maximum at around 12-13 mol% CaO concent (Fig. 1.3) [9]. Further increase in dopant concentration leads to decreased ionic conductivity, in the same way as in other solid oxygen ion conductors. Though, conductivity of CaSZ was found to be significantly lower than that of YSZ in broad temperature range. E.g., the most conductive composition of CaSZ (CaSZ12) exhibits ionic conductivity of $7.2 \cdot 10^{-4}$ S/m at 400 °C, whereas YSZ8 shows $1.8 \cdot 10^{-2}$ S/m at the same temperature [18].

Conductivity activation energy ΔE is also important parameter of oxygen ion conductors, since it characterizes sensitivity of conductivity to temperature change. However, the value of activation energy depends on many factors, such as dopant type, its concentration level, grain size of ceramics [18] and even selection of the temperature range [8]. According to the literature data, activation energies

for stabilized zirconia varies approximately from 0.9 eV for YSZ3 [19] to 1.4 eV for ScSZ9 [20]. Due to its complex nature, a detailed survey of activation energy will not be dealt in this literature review.

In general, the zirconia-based electrolytes are the most common electrolytes for SOFCs, since they comply with the key requirements for electrolytes of SOFCs: high ionic conductivity, high mechanical and chemical stability, etc. [21]. It should be also noted that zirconia ceramics exhibit minimum electronic contribution to total conductivity. Another favourable factor is that zirconia, as a base of these electrolytes, is considered to be abundant and relatively low cost material. Although the stabilization of zirconia with yttria does not yield the highest conductivities, yttrium is the most frequently used dopant because of availability and cost. Calcia as dopant is much less popular, probably due to its lower conductivity, whereas, scandia as dopant is considered to be too expensive to be suitable for industrial applications.

1.2.2. Gadolinia-doped ceria

Other common class of fluorite-structured oxygen ion conductors is based on ceria, which is also doped with Gd_2O_3, Sm_2O_3, Y_2O_3, etc. Ceria-based electrolytes are of considerable interest due to its high ionic conductivity, which in some cases is even higher than that in stabilized zirconia [22].

Regarding stabilized zirconia, optimum dopants for Ce^{4+} (0.97 Å) are Y^{3+} (1.019 Å) and Gd^{3+} (1.053 Å) due to proximity of its atomic radii. However, there is still discrepancy in understanding the relationship between the dopant properties and the ionic conductivity [23]: gadolinia-doped ceria (GDC) has higher ionic conductivity than yttria-doped ceria [24], although the best match for ionic radius of Ce^{4+} (0.97 Å) is yttrium. Since pure ceria already has high temperature phase, and the addition of dopants is carried out solely for the creation of oxygen vacancies, such an operation is called "doping" instead of "stabilization" as for zirconia-based systems. GDC has shown ionic conductivity comparable to that of

ScSZ at 600-800 °C [25]. Activation energies of GDC varies approximately from 0.5 to 1.0 eV for GDC containing 10 mol% Gd_2O_3 (GDC10) and 20 mol% Gd_2O_3 (GDC20), respectively [26].

An optimum gadolinia level for the highest conductivity of GDC shows some discrepancy. Different reports present different optimum concentrations: 10 mol% [10, 27], 15 mol% [28-31] and 20 mol% [32-35]. Contradictory of these results are explained by temperature dependence of optimal dopant concentration, which shifts towards higher value with temperature increase. However, all the mentioned GDC studies have observed presence of certain optimum composition beyond which the conductivity decreases in the same way as for stabilized zirconia.

Doped ceria is frequently referred to as an alternative for stabilized zirconia in various applications. However, it is known that ceria-based compounds have an important disadvantage related to reduction of Ce^{4+} to Ce^{3+} at high temperatures and low oxygen partial pressures [36]. Therefore ceria under reducing environment becomes so-called reduced ceria $CeO_{2-\delta}$, where $\delta = \{Ce^{3+}\}/2$. Such a modification leads to appearance of electronic conductivity, which in most applications is undesirable. Although this problem may be partially solved by decreasing operating temperature of devices to below 950 K or other means [37-41], their implementation brings additional issues. Therefore, application of ceria-based electrolytes is often hindered [42, 43].

In general, both zirconia- and ceria-based oxygen ion conductors are promising for various applications. Considering the effect of chemical composition on the electrical properties of reviewed solid electrolytes, it may be concluded that the main points are both the proximity of dopant and host ionic radii, and appropriate concentration of dopant.

1.3. Effect of processing on electrical properties

Chemical composition is not the only parameter affecting electrical properties of fluorite-structured oxygen ion conductors. Processing conditions, which include

fabrication and sintering of ceramic samples, as well as a thermal prehistory, may also greatly influence its electrical, mechanical properties [44] and even optimal concentration of dopants for the highest conductivity.

Lots of studies dedicated to the investigation of the sintering conditions influence on electrical properties of polycrystalline oxygen ion conductors can be found in the literature. Results show that the sintering temperature and other factors greatly affect relative density of ceramics and its microstructural features, such as dopant segregation, impurities, and formation of ordered micro domains, which in turn greatly influence electrical conductivity of polycrystalline materials.

Before beginning a more detailed review, it should be noted that commercially available powders of zirconia- or ceria-based oxygen ion conductors require high sintering temperatures of about 1500 °C [23, 34, 45-47]. Lower sintering temperatures usually lead to not fully sintered ceramics with low relative density and consequently poor conductivity. E.g., a relative density of YSZ ceramics changes from 50 to more than 90 %, when the sintering temperature increases from 1200 to 1450 °C [48]. There is also a study indicating that relative density of 98 % was achieved for zirconia- and ceria-based ceramics at sintering temperatures higher than 1400 °C [49, 50]. As can be seen, the sintering temperature plays an important role in sintering process, since it is said that for main applications, such as SOFC, a relative density of electrolyte > 94 % is required.

On the other side, it is known that high sintering temperatures result in grain growth [51]. E.g., grain size of YSZ3 ceramics sintered at 1400 °C was found to be less than 1 μm, whereas that at 1500 °C exhibited 2.3 μm [52]. Increase in grain size is usually undesirable, as it leads to decrease of a hardness of ceramics [53]. Moreover, as the sintering temperature increases up to 1600 °C and above, a further growth of grains and formation of hollow holes were detected in stabilized zirconia ceramics [51].

There are many studies considering effects of sintering temperature and grain size on electrical conductivity in zirconia- and ceria-based solid electrolytes. Most

of these agreed that the bulk conductivity is not affected by grain size and sintering temperature, while the conductivity of grain boundary medium was found to be dependent on both of these factors. However, a wide variety of results are presented in literature. As examples may be mentioned GDC10 and GDC20 ceramics. E.g., Jadhav et al. [54] reported that increase of the GDC10 ceramics sintering temperature up to 1500 °C leads to increase of total conductivity and decrease of its activation energy, which was attributed to the increase of bulk conductivity. Studies by Öksüzömer et al. [26] and Lenka et al. [55] have also showed increase in the bulk conductivity with increase in sintering temperature for GDC10 and GDC20 ceramics, which was explained by grain growth at high temperatures. Whereas work by Arabaci et al. [56] revealed an increasing trend in conductivity of grain boundary medium for GDC10 with the increasing sintering temperature. Moreover, Reddy et al. [50] determined considerably different activation energies of conductivity of grain boundary medium, namely, 0.94 and 1.2 eV for GDC10 ceramics sintered at 1100 and 1400 °C, respectively. Similar inconsistencies may also be found on sintering temperature of ceramics made of other oxygen ion conductors. Therefore it is difficult to define optimum sintering temperatures, which would definitely lead to maximum total conductivity.

The effect of grain size on the electrical conductivity of solid electrolytes was also observed. A number of studies revealed slightly decreased or constant conductivity of YSZ [57-59] and GDC [60] ceramics, as the grain size decreased from 20 to 0.2 μm. When the mean grain size was 100 nm or less, opposite and stronger grain size effect was found to occur. Increasing conductivity with decreasing grain size has been reported for thin films of solid electrolytes [61, 62]. E.g., ionic conductivity in nanocrystalline YSZ16 thin films with average grain size of 20 nm was found to be increased by 2-3 orders of magnitude as compared to that of coarse-grained ceramics [63]. Similar conductivity improvement was also observed in GDC thin films when mean grain size decreased from 40 to 10 nm [64]. However, the ionic conductivity in bulk YSZ ceramics with nano-sized grains was found to be poor or even not existing [59, 65-70]. So, the

increase in conductivity of nanocrystalline solid electrolytes was observed in thin films only.

Since high sintering temperature results in high grain size, higher energy costs, increased chemical interactions, and difficulties in co-sintering, many efforts have been made for its reduction. Proposed solutions comprise addition of various additives [71], increase in sintering time, and by taking advantages of particular sintering methods (e.g. pulsed electric current sintering, pressureless sintering, hot pressing, microwave sintering) [70], all of which requires additional instruments. It should be noted that there are also more variables regarding optimum processing conditions of oxygen ion conducting ceramics, such as sintering duration, surface area of powder, etc. There is a lot of contradictory information in the literature, what indicates complexity of the subject or even presence of unknown or uncontrolled parameters in processing of ceramics. Therefore, despite lots of studies dedicated to the investigation of processing's influence on ionic conductivity, various factors still should be understood in order to enhance ionic conductivity.

1.4. Methods for analysis of experimental impedance spectroscopy data and estimation of the distribution of relaxation times

The electrical properties of solid electrolytes are usually investigated by IS. IS is commonly used to study influence of external factors, such as temperature or partial pressure of any gas, on electrical properties of the system. It provides electrical properties (i.e. admittance, impedance, electric modulus and permittivity) as a function of frequency.

A typical frequency dependence of the real part of complex conductivity is presented in Fig. 1.4, which indicates three relaxation dispersions. Here it may be recalled that polycrystalline ceramics consist of different resistive and capacitive components, which causes different relaxation times of charge carrier. Considering the literature data [72, 73], dispersion at low frequency range is

attributed to ion relaxation in the electrode-electrolyte interface. In case of polycrystalline ceramics, dispersion at the intermediate frequency is caused by charge carrier relaxation in grain boundary medium, whereas that one at high frequency region is assigned to charge carrier relaxation in the bulk of solid electrolyte.
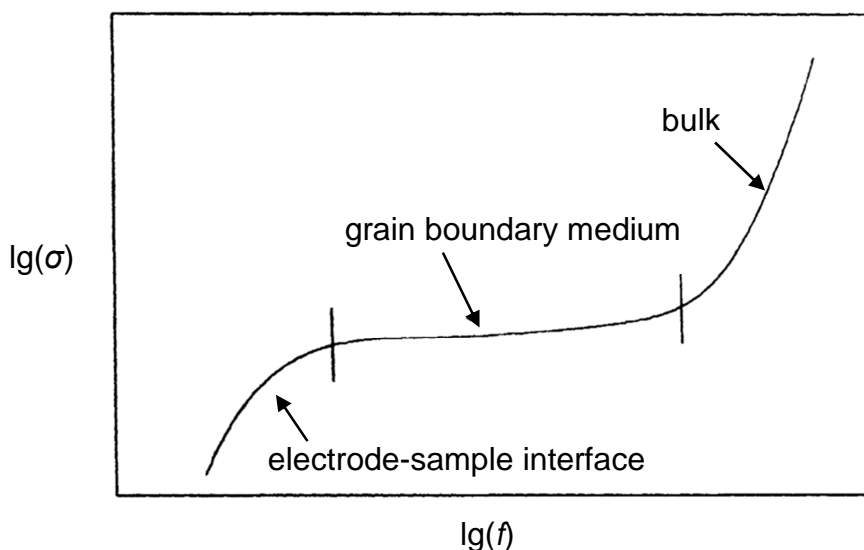
Fig. 1.4. Schematic illustration of conductivity vs. frequency for oxygen ion conducting ceramics.

Electrical parameters of ceramics may be determined by analysis of complex impedance or other representations of electric properties. The most common analysis is made using equivalent circuits, which consist of common electrical components such as resistors (R), capacitors (C), as well as distributed elements such as constant phase element (CPE). Fitting of selected equivalent circuit model to experimental data is easily carried out by specific non-linear least squares fitting software. Although many equivalent circuit models have been reported in literature, a very basic equivalent circuit for polycrystalline ceramics may be consisted of three parallel R and C circuits in series (Fig. 1.5(a)). Parallel RC elements are certain relaxation circuits with time constant $\tau = RC$. In Fig. 1.5(a) represented R_b and C_b refer to resistive and capacitive regions of the bulk, R_{gb} and

C_{gb} – to resistive and capacitive regions of the grain boundary medium and R_e and C_e correspond to processes at electrode-electrolyte interface. In this case each RC element obeys an ideal Debye behaviour and the complex impedance of the circuit can be written as:

$$\tilde{Z}(\omega) = Z' - iZ'' = \frac{1}{1/R_b + i\omega C_b} + \frac{1}{1/R_{gb} + i\omega C_{gb}} + \frac{1}{1/R_e + i\omega C_e}, \qquad (4)$$

where ω is the angular frequency, and i – imaginary unit. The impedance of such a circuit on a complex plane plot (Z'' vs. Z') representation, which is also frequently called "Nyquist plot", appears as a series of somewhat overlapping semicircles (Fig. 1.5(b)). Diameters of these semicircles correspond to resistances related to the bulk, grain boundary medium and electrode-electrolyte interface. Since the processes in these regions have different relaxation frequencies f_r, which correspond to the top of each semicircle and refer to maximum value of the imaginary component, this plot allows the resistances to be separated. The relaxation time of each process can be determined from the relation $\omega\tau = 1$, where $\omega = 2\pi f_r$ and τ is the relaxation time of the process (or time constant of the relaxation circuit). However, frequency is only a parameter of complex plane plot, the direction of increase of which is indicated by arrow in Fig. 1.5(b): low frequency data are on the right side of the plot and higher frequencies are on the left. Since the frequency is not directly evident, if it is required, it needs to be determined by other means.

It should be also noted that most relaxation processes in real materials exhibit non-Debye behaviour, which is caused by certain DRT of charge carrier. Therefore experimental results deviate from ideal capacitor or resistor behaviour, and in complex impedance plane plots appear as depressed semicircles with centre below the real axis. In general it may be concluded that a degree of the distortion of semicircle observed on the complex plane plot is related to measure of DRT of charge carrier and the higher is the distortion, the more widely distributed are relaxation times. Main theories used to describe this occurrence are reviewed in [74]. In some cases the deviations from ideal behaviour are ignored, whereas in

other cases these features are included in the equivalent circuit above by replacing the capacitors by CPEs. The impedance of CPE is written as $1/Q(j\omega)^n$, where Q and n are frequency independent parameters. In case of $n = 0$, CPE represents an ideal capacitor with capacity $C = Q$, while in case of $n = 1$, CPE describes pure resistor with a resistance value of $R = 1/Q$.

(a)
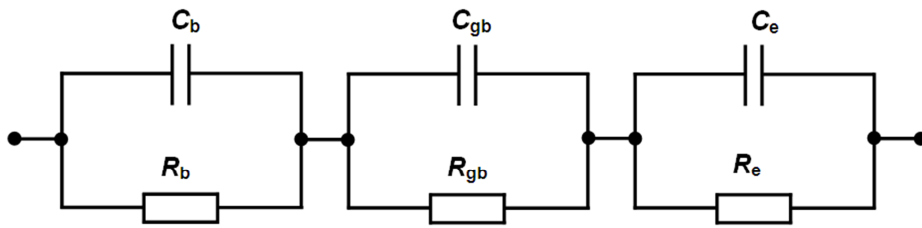
(b)
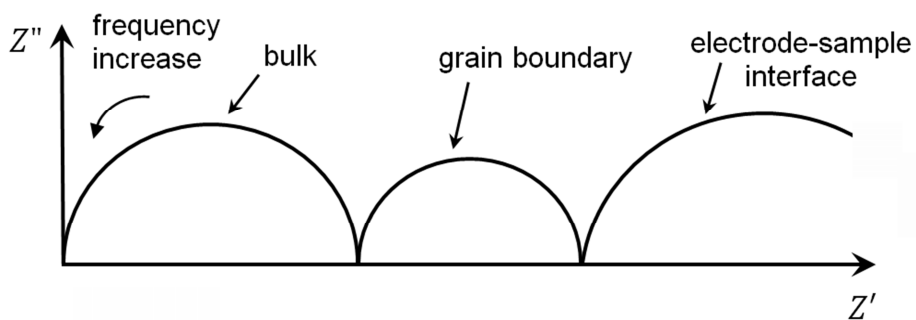
Fig. 1.5. Equivalent circuit for polycrystalline oxygen ion conductor (a) and complex plane impedance plot for this circuit (b).

Equivalent circuit fitting is very convenient and widely used tool for modelling of charge transfer processes. It also allows to determine specific parameters of oxygen ion conductors such as conductivity, high frequency limit permittivity, etc. However, since circuit elements needs to be assigned to physical phenomena situated in a system under consideration, an application of the method requires certain a priori knowledge. Equivalent circuit models are also ambiguous, because different arrangements of the circuit elements can yield exactly the same impedance curves [75]. Moreover, the latter technique is adequate for processes

clearly separated on a logarithmic frequency scale only, whereas overlapping dispersions may be difficult to resolve.

Also there is another approach for analysis of impedance spectra of solid electrolytes, which involves description of AC response by empirical frequency domain functions. One of the most widely used expressions is called "Jonscher power law" or "universal dielectric response". This function divides frequency dependence of real part of electrical conductivity to frequency independent DC conductivity (σ_{DC}) and frequency dependent part:

$$\sigma'(\omega) = \sigma_{DC} + A\omega^n. \tag{5}$$

Here A is a constant for particular temperature and n is a power exponent, which characterizes deviation from the Debye behaviour and can assume values between 0 and 1. For oxygen ion conductors experimental n values are often reported to be between 0.5 and 0.8 [76]. Many studies have demonstrated, that a wide variety of materials, including oxygen ion conductors, as well as many other solid electrolytes with hopping charge carrier, exhibit quite similar frequency dependence of AC conductivity, which may be described by Eq. (5). Also there is a number of other models, such as those of Davidson and Cole [77], Kohlrausch-Williams-Watts [78], Havriliak-Negami [79], etc., used to describe relaxation behaviour of dielectric and conductive systems. A fit of these functions to experimental data provides certain parameters, related to the character of relaxation processes. However, an interpretation of the obtained data by means of empirical frequency domain functions requires a priori knowledge of number of processes in the system. As the available information does not appropriately reflect the actual processes in the material, this technique, as well as equivalent circuit modelling, gives erroneous results.

However, in recent years, an alternate method has been increasingly used, which allows a determination of the DRT function directly from the frequency domain data and bypasses the need for a priori knowledge of the physical processes. In contrast to these two above described methods, this one is able to separate processes with comparable relaxation times. The most common

33

applications of this technique are dielectric systems. In this approach a complex permittivity spectrum $\tilde{\varepsilon}(\omega) = \varepsilon' - i\varepsilon''$ can be described by an ensemble of Debye processes with continuous DRT function (similarly as in [80]):

$$\tilde{\varepsilon}(\omega) = \varepsilon_\infty + \int_{-\infty}^{\infty} \frac{g(\tau)}{1 + i\omega\tau} d\lg\tau, \qquad (6)$$

where $g(\tau)$ – continuous DRT function $(g(\tau) \geq 0)$, and ε_∞ – high frequency limit permittivity.

In case of conductive systems this technique is based on an assumption that complex impedance spectrum $\tilde{z}(\omega)$ may be represented as superposition of the elements with individual relaxation times. In other words, the system is assumed to consist of an infinity number of *RC* circuits, the impedance of which may be expressed by the following integral in a similar way as in [81]:

$$\tilde{z}(\omega) = z_\infty + z_{DC} \int_{0}^{\infty} \frac{f(\tau)}{1 + i\omega\tau} d\tau, \qquad (7)$$

where $f(\tau)$ – DRT function $(f(\tau) \geq 0)$, and z_∞ – high frequency limit impedance. In such a notation, $f(\tau) \cdot (1 + i\omega\tau)^{-1} d\tau$ represents the contribution of processes with relaxation times between τ and $\tau + d\tau$.

Solutions of Eqs. (6) and (7) are of high importance, since they give information about dynamics of charge carriers. However, these equations have form of a Fredholm integral equation of the first kind and it is known that direct extraction of $g(\tau)$ from $\tilde{\varepsilon}(\omega)$, as well as $f(\tau)$ from $\tilde{z}(\omega)$ is mathematically ill-posed problem, which means that solution may be not unique, or it may be extremely sensitive to errors in initial data. It should be noted that, as the dielectric or conductive system is characterized by real and imaginary parts of permittivity, impedance or other experimentally obtained property, the application of Eqs. (6) and (7) requires good quality of data, which would obey Kramers-Kronig relations. Moreover, since the experimental data points are discrete and the continuous distributions are also represented by discrete points, one must expect that there will always be some error in the estimated DRT function.

But even so, a number of special techniques have been proposed for approximate solution of ill-posed problems. Main of these are Marquardt-Levenberg search algorithm [82], Monte-Carlo method [83, 84], combination of Fourier analysis, extrapolation and filtering [81], evolutionary programming techniques [85], and different regularization techniques, such as Tikhonov regularization method [86]. The latter method is one of the most convenient and most frequently used in practices and therefore was chosen in this study. The term "regularization" in its name means that it involves certain residual function, which measures the smoothness of the solution and is controlled by choice of certain regularization parameter.

Numerous studies have been carried out to estimate the DRT function directly from experimental data. However, the majority of reports were dealing with the behaviour of DRT function of dielectric systems. E.g., group of works by J.R. Macdonald [73, 77, 87, 88] has presented a number of techniques for analysing dielectric response in frequency domain by means of numerical methods, which have been applied to synthetic and experimentally obtained data. Some other successful examples by E. Tuncer et al. [83, 89], V.A. Stephanovich et al. [90], F. Aslani et al. [91], H.E. Atyia [92], A. Mikonis et al. [93], J. Macutkevic et al. [80] should be also mentioned.

Much more limited number of studies were dealing with conductive systems. Probably the most comprehensive group of works on DRT function of conductive systems [81, 94-98] was published by E. Ivers-Tiffée and colleagues. They have developed a method, which allows calculation of $f(\tau)$ directly from imaginary part of the experimental impedance data [81]. The proposed algorithm is based on inverse Fourier transformation with subsequent extrapolation and digital filtering in the transformed space. Thereafter this group have reported the results of extraction of DRT function for a number of electrochemical systems, such as cathode-electrolyte-anode interfaces in SOFCs [81, 94, 95, 97-99]. The method applied in the studies allowed to resolve up to three distinct relaxation processes within one frequency decade [81]. The obtained data were used for identification

of physical processes in the respective elements, as well as for the improvement of frequency resolution of the impedance data [96].

Another significant contribution to this field was made by group of Y. Tsur, which has introduced genetic algorithm (GA) and genetic programing (GP) approaches [85, 100, 101]. The GA fits the DRT function to a predetermined model, such as Gaussian distribution function, whereas when more than one process is considered, a superposition of selected models may be applied. The GP algorithm is quite similar to the GA, with the main difference that it creates new models of DRT function by combining certain mathematical functions. Optimization of these models is in both cases performed by specific strategy, which is based on algorithms similar to those observed in nature and therefore is called "evolutionary programming". An analysis of experimental data for niobium-doped $BaTiO_3$ by GA and GP algorithms revealed that the DRT function in these samples may be good enough represented by functions based on Gaussian function. More recent study by S. Hershkovitz, S. Baltianski, and Y. Tsur [101] has reported four different peaks in the DRT function, made of combinations of Gaussian, Lorentzian, and hyperbolic secant, obtained by GP algorithm for symmetric cell made of lanthanum strontium cobalt ferrite (LSCF) and GDC. Another work by S. Hershkovitz et al. [100] is the only paper of others, than the author of this dissertation, found that deals specifically with the DRT function of fluorite-structured oxygen ion conductor (GDC10). Most of other existing studies are dedicated to the DRT function related to the electrode-electrolyte interface or electrolytes with another structure. In case of GDC10, the GP algorithm has also detected four different peaks in the impedance spectra obtained by 2-electrode method. However, a detailed assignment of peaks to their physical origin could not be done due to certain features of measurement method and limited frequency range of measurement equipment used in the study (100 mHz-1 MHz).

Other particular contributions to development and implementation of methods for estimating the DRT function of conductive systems should be also mentioned. E.g., Francesco Ciucci et al. [102] have presented method based on Bayesian and

hierarchical Bayesian approaches, which is very similar to Tikhonov regularization one. B.A. Boukamp has also developed Fourier transform-based algorithm [103], similar to that of E. Ivers-Tiffée et al. In the same work by B.A. Boukamp is presented a collation of DRT functions for LSCF, which were obtained by two different methods: the GA algorithm and method, developed by B.A. Boukamp on its own. Though, practically all previous experimental studies of electrical properties of solid oxygen ion conductors were carried out in limited frequency range or temperature interval. The main reason for this may have been that relaxation frequencies at elevated temperatures exceed limits of conventional measurement techniques. Since microwave measurements are not widely used by researchers of solid electrolytes, this factor restricts opportunities to observe changes of obtained dispersions' region in broad temperature range.

The applications of equivalent circuit fitting and empirical frequency domain functions, as well as the above described methods for estimation of the DRT function, enable to estimate relevant information on the investigated material from impedance spectra. E.g., they allow to measure dielectric and charge transport properties of the solid electrolytes. Estimated parameters of the materials can be also used for prediction of the behaviour of systems under various conditions.

2. Experimental

This chapter reviews processing of the studied samples, as well as methods and techniques applied to their investigation. Since the IS is the main tool for characterising electrical properties of solid electrolytes, and during the study a new measurement technique was developed, the main focus is focused on this method and subsequent analysis of the obtained results. Other techniques, such as scanning electron microscopy, differential thermal analysis and X-ray diffraction, are also outlined in this chapter.

2.1. Material processing

A wide range of materials was used in order to summarize the electrical properties and other characteristics of oxygen ion conductors. Most of samples studied were in the form of polycrystalline ceramics, which have found extensive applications due to its fast production that requires no sophisticated equipment. Two zirconia-based single crystals were also included in the study, since the influence grain boundary medium is eliminated in this type of samples. A complete list of the materials studied is presented in Table 1.1.

Table 1.1. Studied oxygen ion conductors.

Compound	Chemical formula	Form
YSZ3	$Zr_{0.97}Y_{0.03}O_{1.97}$	ceramic
YSZ8	$Zr_{0.92}Y_{0.08}O_{1.96}$	ceramic
YSZ10	$Zr_{0.9}Y_{0.1}O_{1.95}$	single crystal
ScSZ10	$Zr_{0.9}Sc_{0.1}O_{1.95}$	ceramic
CaSZ15	$Zr_{0.85}Ca_{0.15}O_{1.85}$	single crystal
GDC10	$Ce_{0.9}Gd_{0.1}O_{1.95}$	ceramic
GDC20	$Ce_{0.8}Gd_{0.2}O_{1.9}$	ceramic

The YSZ and CaSZ single crystals, grown by the skull melting method [104, 105], were obtained from Swiss Federal Institute of Technology (Switzerland). Solid electrolyte ceramics were sintered from commercial powders, produced by company "Fuel Cell Materials". Pure powders without any additives were first preheated at 600 °C for 2h in an air, and then uniaxially cold pressed in a steel die of 8 mm diameter. Sintering of the powder compacts was performed in air atmosphere at various temperatures from 1100 to 1500 °C for 1 or 2 h with a heating rate of 5 °C min^{-1}. Density of the obtained products was determined by geometric and Archimedes methods. The reached density values of the sintered ceramics were not lower than 94 %.

2.2. Broadband impedance spectroscopy

IS is a powerful tool used to characterize ionic conductors, processes in which take place simultaneously but with different time constants. The method may be used in the study of conductive single crystals, ceramics, glasses, as well as other materials. Impedance measurements were carried out at Solid State Ionics laboratory, Vilnius University.

2.2.1. General considerations

The electrical impedance is a complex ratio of voltage to current in an AC circuit. It extends the concept of resistance to AC circuits, and possesses both magnitude and phase, unlike resistance, which includes magnitude only. The impedance spectrum is usually represented in complex form $\tilde{Z}(\omega) = Z'(\omega) - iZ''(\omega)$. The real part of impedance is the resistance $Z' = \mathrm{Re}(\tilde{Z}) = |\tilde{Z}|\cos\theta$, and the imaginary part is the reactance $Z'' = \mathrm{Im}(\tilde{Z}) = |\tilde{Z}|\sin\theta$, where $\theta = \arctan(Z''/Z')$ is the phase difference between voltage and current. Since $\tilde{Z}$ denotes absolute impedance, which can be related to the specimen dimensions, more important property for estimation of material properties is the specific impedance $\tilde{z}$. The specific impedance is defined as the product of its absolute impedance $\tilde{Z}$ and ratio of the electrode area S and sample length l:

$$\tilde{z} = \tilde{Z}S/l. \tag{8}$$

There are several other derived quantities related to impedance, which often play important roles in IS. These are specific admittance $\tilde{\sigma}(\omega) = z^{-1} = \sigma' + i\sigma''$, specific electric modulus $\tilde{m}(\omega) = i\omega\varepsilon_0 z = m' + im''$, and permittivity $\tilde{\varepsilon}(\omega)$. The listed specific properties represent physical characteristics of the material, and since this study will deal with specific properties only, the word "specific" will usually be omitted.

Generally speaking, the measurements of electrical impedance are usually made with specimens having two identical electrodes applied to the faces of a sample. In a typical experiment, a small electrical signal is applied to perturb the system, and the resulting linear response signal of current or voltage is observed as a function of the perturbation frequency. It is usually assumed, that the properties of the electrode-electrolyte system are time invariant, and the response is monitored.

IS has multiple possible experimental setups developed, the most important of which for oxygen ion conductors are 2- and 4-electrode methods, which will be described in more detail in the next sections. In this work the investigations of electrical properties were performed by combining both these methods.
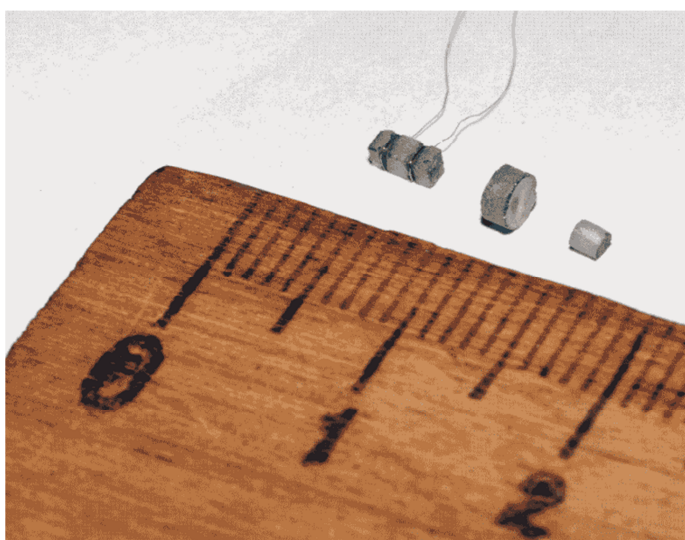
Fig. 2.1. YSZ single crystal samples prepared for IS measurements.

Two types of samples were prepared for distinct IS techniques. Measurements by 2-electrode method were performed using cylindrical samples of 1.5 mm in length and up to 3 mm in diameter (Fig. 2.1, two samples on the right). Whereas rectangular samples of about 8×1.5×1.5 mm were needed for 4-electrode method (Fig. 2.1, sample on the left). The electrodes of the samples were prepared using Pt paste made by "Gwent Electronic Materials LTD", fired at 1073 K, except for

voltage electrodes in case of the 4-electrode method, where platinum wires turned around the sample were used.

2.2.2. Measurement technique at low frequencies (100 mHz-2 MHz)

Impedance measurements at low frequency range were carried out by recently developed impedance spectrometer (described in [106]), operating in the frequency range of 100 mHz to 2 MHz. The equipment is capable of performing 2- and 4-electrode measurements in sample temperatures ranging from 300 to about 900 K. Hardware of this spectrometer is also capable to perform measurements in both frequency and time domains.

The impedance by the 2-electrode method is obtained by measuring the current through sample and the resulting voltage drop. The latter measurement technique is quite common, however, at low frequency range it quite often gives complex results that are difficult to interpret. The problem is that for the measurement of both physical quantities are used the same two electrodes. In such a way, it is not possible to measure the impedance of the sample itself, since the electrode-sample interface affects the total response. In case of highly conductive materials at low frequencies, the effects at the electrode-sample interface may obscure any useful information. E.g., this shortcoming restricts opportunities to directly measure the electrical properties of grain boundary medium of any polycrystalline oxygen ion conducting ceramics due to strong electrode-electrolyte interface polarization effect. Therefore overcoming this problem is very important.

The electrode-sample interface effects quickly become negligible when moving away from the electrode, which suggests that optimal voltage measurement points are in the bulk of the sample. This is the main point of the 4-electrode impedance measurement method, where the voltage measurement electrodes are placed on the sides of the sample, away from the current electrodes (as illustrated in Fig. 2.1). This measurement setup has a considerable experimental advantage over 2-electrode one, however, it requires advanced

hardware. E.g., since no current must flow in the voltage electrodes, it is necessary to use a differential amplifier with an extremely high input impedance and low capacitance. It should be noted that there are several commercial impedance spectrometers, operating in frequencies ranging from µHz up to a few MHz, that are available from Solartron Analytical, Novocontrol, Agilent Technologies, Gamry Instruments, Autolab, etc. Still, almost all of these spectrometers operate using 2-electrode method, and Novocontrol only offers a 4-electrode impedance measurement system. However, the capacitance of the differential voltage input is high, reaching 10 pF, whereas that of equipment used in this study is less than 2 pF.
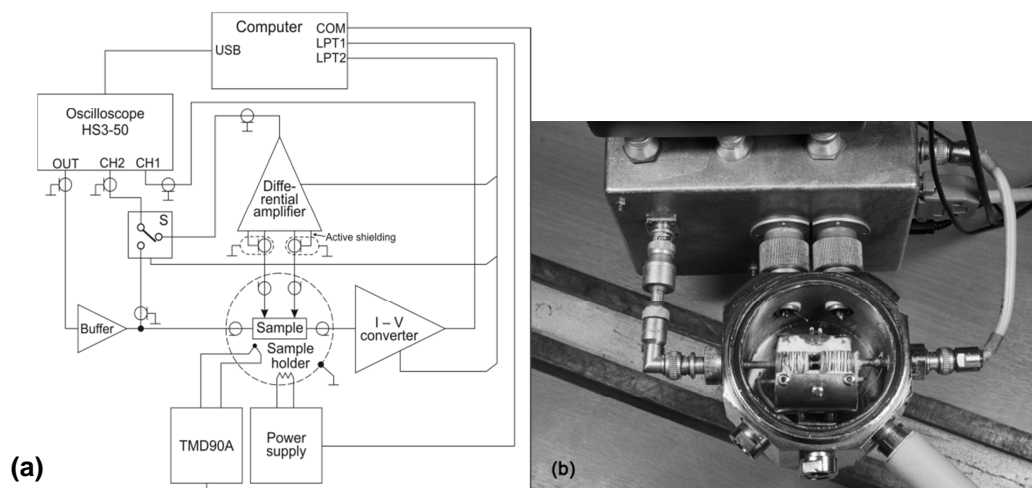
Fig. 2.2. Schematic overview of the impedance spectrometer operating in 2- and 4-electrode methods (a) and its photograph (b).

The latter impedance spectrometer consists of several distinct components, which are shown in Fig. 2.2. The electrical signals are measured by a two channel computer oscilloscope "Handyscope HS3" (TiePie), which has an adjustable resolution (12, 14, or 16 bits) and a built-in function generator. A generated sinusoidal signal is applied to the sample through a buffer. Investigations were usually performed by applying sinusoidal signal with amplitude of 6 mV. The current through the sample is measured by a current to voltage (I–V) converter, which feeds the signal to the first channel (CH1) of the oscilloscope. In case of 4-

electrode operation, a differential amplifier is connected to measure the voltage drop on the sample, the output of which is fed through the switch S to the second channel (CH2) of the oscilloscope. Otherwise, 2-electrode voltage measurements are taken by connecting the buffer's output to the oscilloscope's CH2 input.

The sample is placed in a custom sample holder. The holder assembly is connected to a digital thermometer "TMD90A" (Amprobe) and a custom computer-controlled power supply for the heater, which are used for temperature control of the sample. All of the control logic of the spectrometer, signal processing, as well as data storage and analysis are implemented in Matlab software. Measurements by both 2- and 4-electrode methods provided experimental data with 40 points per frequency decade.

2.2.3. Measurement technique at high frequencies (300 kHz-~10 GHz)

IS investigations at high frequency range (from 300 kHz to ~10 GHz) were based on the measurement of scattering parameters (*S*-parameters) matrix for a 2-port network made of a coaxial waveguide and a sample, inserted in the gap of a central conductor. Since the electrode-electrolyte interface effects are manifesting at low frequencies only, solely 2-electrode method was applied in high frequency region.

Before beginning a more detailed review, it should be noted that in total there were three different impedance spectrometers used for investigation of oxygen ion conductors in this study. The measurements carried out during the first years of PhD studies were performed by using the low frequency spectrometer detailed in subsection 2.2.2. and previously developed equipment for impedance measurement in frequency range from 300 kHz to 3 GHz [107]. Analysis and interpretation of these results are presented in subsections 3.1.1 and 3.1.2. The remaining results (except these obtained by 4-electrode method), presented in sections 3.1.3. and 3.2., were measured by new recently developed ultra-broadband impedance spectrometer operating at frequencies from 100 mHz to about 10 GHz. It combines already described low frequency equipment and the

high frequency one, which will be specified below. More details about the method of measurements in high frequency range are presented in [1].

Since the microwave measurements are not widely used by researchers of solid electrolytes, it is difficult to find any commercially available equipment which would be suitable for oxygen ion conductors at high frequency and elevated temperatures. Therefore, a new methodology for impedance measurement at broad frequency and temperature ranges was developed at Solid State Ionics laboratory, Vilnius University. It should be noted that there already were methods applicable at temperatures close to 1000 °C, such as so-called "open-ended coaxial probe" [108-111], or resonator methods [112, 113]. However, the newly developed technique employs a new model of the measuring circuit (MMC), which is much more accurate than the one presented in [107], as well as a measurement method, specifically developed for a specific sample holding system. The main advantage of this technique as compared to others is dramatically reduced influence of the transmission line's thermal expansion, which is particularly important in high temperature applications.

The second important property of the proposed method is that the MMC takes into account the parasitic reflections of the sample holding system. Therefore there is no necessity to have a sample holder with the characteristics approaching an ideal transmission line. This is especially important in the GHz frequency range. Furthermore, this model takes into account the distribution of the electromagnetic field in the measuring capacitor (MC) without solving a complicated electrodynamics problem, which generally involves complex calculations (e.g., [114, 115]). The method is suitable for determination of specific electrical (complex permittivity, electrical modulus, impedance, conductivity) and corresponding absolute properties of small samples. The only feature of this method, which, in some particular cases, could be considered as a shortcoming, is that it requires knowledge of a full two port scattering matrix.

The proposed MMC assumes that the device under test is a coaxial waveguide with a sample to be measured inserted in the gap of the central conductor

44

(Fig. 2.3). The testing device is connected to the ports of the network analyzer in planes A-A and B-B, and one must assume that a perfect measurement of the full two port *S*-parameters in these planes is possible. The ends of coaxial waveguide are fixed, thus telescopic construction of the external conductor maintains overall length of the line constant during heating. Telescopic construction of the internal conductor, employing a spring, allows the short-circuiting of the line and the insertion of varying length samples. A photograph of the developed respective measurement setup is presented in Fig. 2.4.
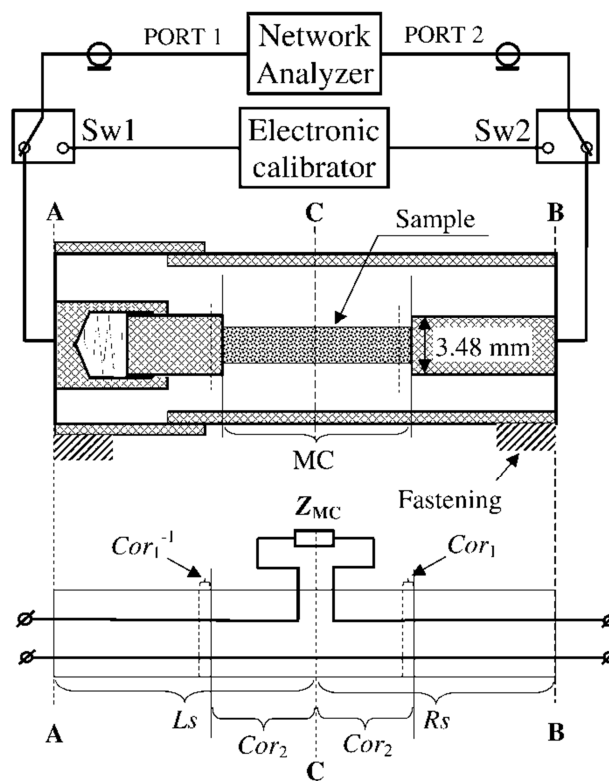
Fig. 2.3. Structure and equivalent circuit of the coaxial sample holder.

Formalism of scattering transfer parameters (*T*-parameters) is preferable for the analysis of cascading networks. The relationship between matrices **S** and **T**, and their parameters may be defined as follows [116]:

$$\mathbf{T} = \frac{1}{S_{21}} \begin{vmatrix} -S_{11}S_{22} + S_{12}S_{21} & S_{11} \\ -S_{22} & 1 \end{vmatrix}. \qquad (9)$$

45
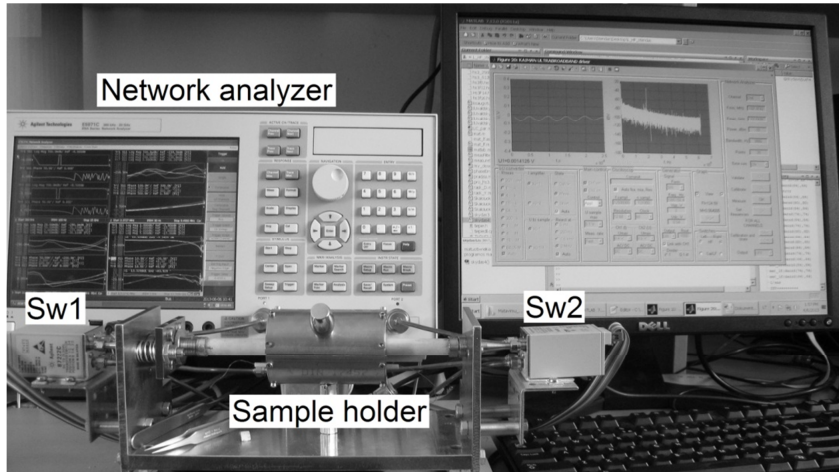
Fig. 2.4. Photograph of the measurement setup. Sw1 and Sw2 denote microwave switches, which, when required, connect the network analyzer to the electronic calibrator.

The equivalent circuit of this sample holder consists of several two-port networks. When the sample holder is short circuited, one can write the transfer parameters $\mathbf{T}_{SC}$ for the whole transmission line:

$$\mathbf{T}_{SC} = \mathbf{LsRs}. \tag{10}$$

Here $\mathbf{Ls}$ and $\mathbf{Rs}$ are the T-parameters of the left (L_S) and right (R_S) sections of the non-ideal 50 Ω coaxial transmission lines, respectively. It is considered, that both sections are short-circuited in the reference plane C-C (Fig. 2.3), which passes through the centre of the sample to be measured. If the sample is inserted, both of the mentioned sections become shorter. Also, the electrical length of the transmission line section with the sample is not equal to its geometrical length and depends on the geometry, as well as on the electrical properties of the sample. A change in the electrical length of the transmission line due to sample insertion is represented by two small ideal transmission lines Cor_2. As the temperature rises, the length of the section R_S increases due to thermal expansion (short ideal line Cor_1), while simultaneously shortening the left section of the structure within the telescopic assembly by the same amount (line Cor_1^{-1}). This compensates the total elongation of the central conductor. Let $\mathbf{Cor}_1$ and $\mathbf{Cor}_2$ be the T-parameter

46

matrices of the corresponding sections. If the T-matrix of the MC is $\mathbf{X}_{MC}$, one can write:

$$\mathbf{T}_X = \mathbf{Ls}\,\mathbf{Cor}_1^{-1}\mathbf{Cor}_2\mathbf{X}_{MC}\mathbf{Cor}_2\mathbf{Cor}_1\mathbf{Rs} \ . \tag{11}$$

Here $\mathbf{T}_X$ is the transfer matrix of the overall transmission line and

$$\mathbf{X}_{MC} = \begin{vmatrix} 1 - \dfrac{Z_{MC}}{2} & \dfrac{Z_{MC}}{2} \\ -\dfrac{Z_{MC}}{2} & 1 + \dfrac{Z_{MC}}{2} \end{vmatrix} . \tag{12}$$

Z_{MC} is considered to be a lumped parameter, which in Eq. (12) stands for the impedance of the MC, normalized to the characteristic impedance of the transmission line.

The results of the testing, using a coaxial sample holder made from a refractory ceramic coated with platinum, demonstrate that the method is suitable for carrying out measurements in the megahertz and gigahertz frequency range up to about 1200 K and higher temperatures. Investigations of solid oxygen ion conductors by this equipment were usually carried out by using the power of AC signal of 0 dBm and obtaining up to 64 points per frequency decade. All measurements were carried out in air, the temperature was controlled by computer connected to K-type thermocouple and DC power supply in the same way as in case of low frequency impedance spectrometer.

2.3. Method for the determination of the distribution of relaxation times by Tikhonov regularization method

The algorithm for estimation of DRT function was developed in cooperation by doc. dr. Algimantas Kežionis and the author of this thesis. Tikhonov regularization method, as well as other methods for estimating the DRT function directly from experimental data, requires good quality of input data, which obey Kramers-Kronig transform. Therefore, the obtained impedance results were at first checked by integral Kramers-Kronig relations as described in [117]:

$$z'_{KK}(\omega) = \left(\frac{2}{\pi}\right)\int_0^\infty \frac{x \cdot z''_m(x) - \omega \cdot z''_m(\omega)}{x^2 - \omega^2}\,dx, \qquad (13)$$

$$z''_{KK}(\omega) = -\left(\frac{2\omega}{\pi}\right)\int_0^\infty \frac{z'_m(x) - z'_m(\omega)}{x^2 - \omega^2}\,dx, \qquad (14)$$

where ω and x are angular frequencies. Straightforward integration, without any extrapolation or other procedures, was employed due to presence of experimental data in broad frequency range.
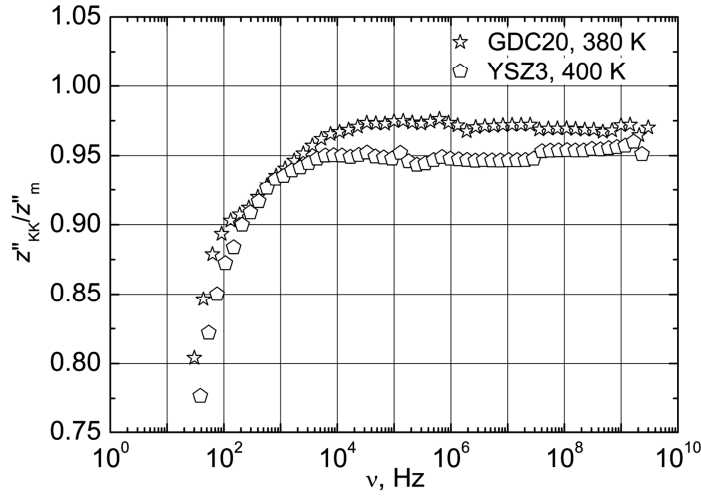
Fig. 2.5. Ratio of obtained by Kramers-Kronig transformation and measured imaginary parts of impedance.

An illustration of comparison of reconstructed z''_{kk} using Eq. (14) and measured z''_m data is presented in Fig. 2.5. The examples refer to relatively low temperatures, where real and imaginary parts of electrical properties differ in few orders of magnitude and, consequently, the accuracy of measurements is inevitably low. However, the measurement conditions are improved with increase of temperature and electrical conductivity. Therefore, the presented illustration confirms sufficient quality of the performed measurements even at severe conditions, except for low frequencies, where effect of limited frequency range is

observed. It should be also noted, that the lowest frequency experimental data in general were disregarded in this study, because they are mostly related to the properties of electrode-electrolyte interface.

The obtained spectra were also further analysed for finding DRT function, supposing that impedance spectrum can be represented as a sum of elements with individual relaxation times, as already indicated by Eq. (7). With a little bit of algebra, the real and imaginary parts of Eq. (7) can be expressed as:

$$z'(\omega) = z_\infty + \int_{-\infty}^{\infty} f(\tau) \frac{1}{1+\omega^2\tau^2} d\lg(\tau), \tag{15a}$$

$$z''(\omega) = \int_{-\infty}^{\infty} f(\tau) \frac{\omega\tau}{1+\omega^2\tau^2} d\lg(\tau). \tag{15b}$$

Matlab application, which employs regularization tool package [118] and familiar formalism as other the same purpose numerical algorithms [80, 86], has been developed to solve these equations. In this application Eqs. (15a) and (15b) are sampled in the logarithmic frequency and time scales with equidistant steps:

$$h_\omega = \Delta\lg\omega, \quad h_\tau = \Delta\lg\tau. \tag{16}$$

So one can write:

$$\begin{cases} \dfrac{1}{z'(\omega_1) - z_\infty} \displaystyle\sum_{k=1}^{N} f_k (1+\omega_1^2\tau_k^2)^{-2} h_\tau = 1; \\ \vdots \\ \dfrac{1}{z'(\omega_N) - z_\infty} \displaystyle\sum_{k=1}^{N} f_k (1+\omega_N^2\tau_k^2)^{-2} h_\tau = 1; \\ \dfrac{1}{z''(\omega_1)} \displaystyle\sum_{k=1}^{N} f_k \omega_1 \tau_k (1+\omega_1^2\tau_k^2)^{-2} h_\tau = 1; \\ \vdots \\ \dfrac{1}{z''(\omega_N)} \displaystyle\sum_{k=1}^{N} f_k \omega_N \tau_k (1+\omega_N^2\tau_k^2)^{-2} h_\tau = 1. \end{cases} \tag{17}$$

Where $\tau_1 - \tau_N$, $\omega_1 - \omega_N$ – sampled relaxation time and frequency, respectively. If DC specific resistivity z_{DC} is known, this system of 2N equations can be supplemented with one more equation:

$$\frac{1}{z'_{dc} - z_\infty} \sum_{k=1}^{N} f_k h_\tau = 1. \tag{18}$$

The solutions of Eqs. (17) and (18) must satisfy inequality $f_k > 0$.

Regularization tool package, used for solution of ill-posed problem, implements several regularization methods. The tests on solving Eqs. (17) and (18) revealed that in this case Tikhonov regularization method and function of regularization tool package *tikhonov* gives the best matching of experimental and calculated results. However, this regularization method requires to set regularization parameter λ manually.

Table 2.1. The baseline data of numerical experiment.

No. of curve	M	σ_G	Added noise, %	RMS error, %	Regularization parameter λ	Comments
1	-7.602	0.33	-	-	-	Initial DRT
2	-7.602	0.33	0.01	0.35	0.003	Backwards calculated DRT
3	-7.602	0.33	1	2.67	0.072	Backwards calculated DRT
4	-7.602	0.33	1.6	2.22	0.144	Backwards calculated DRT
5	-7.602	0.33	3.16	3.84	0.21	Backwards calculated DRT

A numerical experiment was performed to verify the effectiveness of this method. It was supposed to be Gaussian distributed relaxation times in the logarithmic time scale:

$$f(\tau) = \frac{1}{\sigma_G \sqrt{2\pi}} \exp\left(-\frac{(\lg\tau - M)^2}{2\sigma_G^2} \right), \tag{19}$$

where M and σ_G are mean and standard deviation of $\lg\tau$, respectively. Impedance versus frequency was calculated (it was supposed that $z_\infty = 0$) using Eqs. (15a) and (15b) during this experiment. Measurement errors were simulated by adding Gaussian white noise to real and imaginary parts of impedance. Finally the DRT function was calculated backwards by using Matlab application and

choosing regularization parameter λ. The choice of λ was based on minimal RMS (Root Mean Square) error of impedance, simulated using DRT function obtained from noisily data. The baseline data and results of the numerical experiment are presented in Table 2.1 and Fig. 2.6.
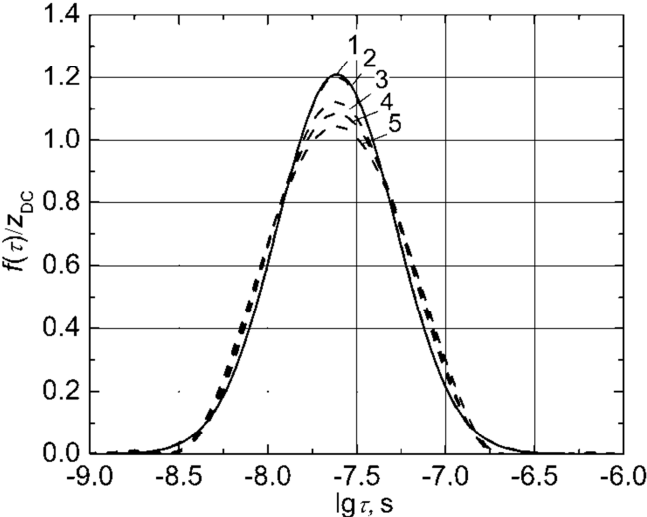
Fig. 2.6. Initial and calculated backwards DRT functions with different noise added, % (1 – initial, 2 – 0.01 %, 3 – 1 %, 4 – 1.6 %, 5 – 3.16 %).
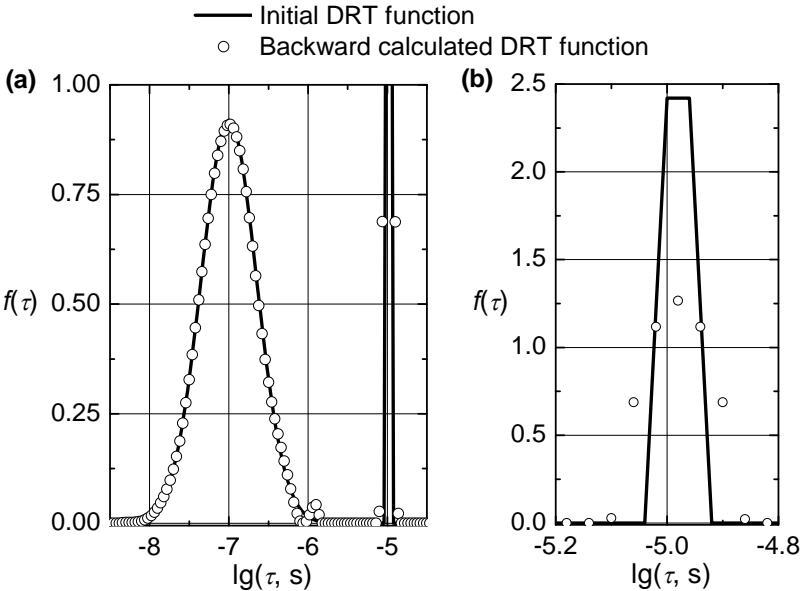
Fig. 2.7. Initial and backward calculated DRT functions.

When 0.01 % noise was added, minimum RMS error and very good correspondence of initial and simulated DRT functions was found for $\lambda \cong 0.003$ (Fig. 2.6 curves 1, 2). In more noisy cases the minimum of RMS error was found at higher values of RMS error and λ. Corresponding DRT functions are presented in Fig. 2.6 (curves 3, 4, 5), which confirms sufficient agreement of initial and calculated results.

However, a slightly improved algorithm than the one described above was used for estimation of DRT functions in sections 3.1.3. and 3.2. The resolution capabilities of the modified algorithm are demonstrated in resolving synthetic DRT function consisting of Gausian ($\sigma_G = 0.35$) and narrow rectangular (close to Debye, containing 2 relaxation time points only) distributions. The DRT function contained 25 points per time decade, what corresponds to real experimental conditions. The impedance data from this synthetic DRT function have been calculated, from which the DRT function was backward calculated. The initial and backward calculated DRT functions at different scales are presented in Figs. 2.7(a) and 2.7(b), which demonstrate sufficiently high resolution of the method.

2.4. Scanning electron microscopy

Scanning electron microscopy (SEM) is an useful technique for studying surfaces of ceramics. The technique is particularly suitable in characterizing the microstructure of ceramics. In this study the microstructure of certain sintered samples was characterized using a scanning electron microscope JEOL JSM-6510LV. The characterization was carried out in University of Maine (France) and supervised by engineer Tibaut Languenne.

The surfaces of the studied specimens were at first polished using successive grades of emery paper. Then samples were thoroughly degreased, cleaned ultrasonically by using alcohol as solvent, and washed by water. After the cleaning, samples were dried completely using oven. The examination of samples was performed without any conductive coating applied.

2.5. Differential thermal analysis

Differential thermal analysis (DTA) was used to check for the character of phase transition of ScSZ ceramics. The investigation was carried out with a "SDT Q600" (TA Instruments) equipment at University of Maine.

In principle the DTA technique comprises measurements of a difference in temperature between the sample and an insert reference as a function of temperature, as the two specimens are subjected to identical heat treatments. In this study aluminium oxide (Al_2O_3) was used as a reference material and the sample was ScSZ ceramics. The crucibles with the specimens were placed in the machine, where built-in thermocouples measured their respective temperatures. The samples were heated and cooled at a 20 K/min under airflow 100 mL/min. The DTA data were collected at 292-1173 K.

2.6. X-ray diffraction

The crystal structure of ScSZ ceramics was determined at different temperatures by X-ray diffraction (XRD) analysis. A PANalytical X'pert MPD PRO diffractometer (CuKα radiation) at University of Maine was used in the study. XRD measurements were taken at temperatures up to 840 K in the 2Θ range of 5-60° with step size of 0.03°.

3. Results and discussion

The first subsection of this chapter presents and discusses the electrical properties and charge carrier relaxation phenomena as functions of temperature and dopant concentration in oxygen ion conductors listed in Table 1.1. These data are published in two articles ([119] and [120]) in journal "Solid State Ionics". Subsection 3.1.2. presents a study of effect of sintering temperature on electrical properties of GDC ceramics, which can also be found in journal "Journal of Materials Science" [121]. Investigation of ScSZ ceramics in the vicinity of phase transition, which is published in journal "Electrochimica Acta" [122], is reported

in subsection 3.1.3. A more general analysis of relaxation behaviour in zirconia- and ceria-based oxygen ion conductors is given in section 3.2. These results are also published in journal "Solid State Ionics" [123].

3.1. Electrical properties and charge carrier relaxation phenomena

3.1.1. Effect of temperature and dopant concentration

The investigations were carried out by impedance spectroscopy in broad frequency range (from 100 mHz to 3 GHz). Obtained results allowed to observe the dispersion of electrical properties, attributed to charge carrier relaxation, in wide temperature range (from ~500 to ~1000 K). The study also includes mathematical analysis of experimental data in terms of the DRT function.

Typical spectra of the real part of impedance for oxygen ion conducting ceramics contained up to three dispersion regions, which were attributed to oxygen ion relaxation in the electrode-sample interface (at low frequencies), grain boundary medium (at intermediate frequencies) and bulk (at high frequencies) (Fig. 3.1). Since the study deals with the electrical properties of the materials itself, the contribution of electrode-sample interface was eliminated by taking advantage of 4-electrode measurement method. The only difference between impedance spectra for oxygen ion conducting ceramics and single crystals is that the latter do not contain dispersion caused by charge carrier relaxation in grain boundary medium.

One of the most important parameters of oxygen ion conductors are total (often also referred to as DC) electrical conductivity and these of bulk and grain boundary medium regions. Total specific resistance of ceramics is approximately equal to a sum of resistances of bulk and grain boundary medium: $\rho_t = \rho_b + \rho_{gb}$, whereas bulk conductivity for single crystals is equivalent to DC conductivity.

An example of complex plane plot is presented in Fig. 3.2, where semicircular arcs, some of which contain tails at the low frequency end, are shown. According to the literature data [72, 124, 125], nearly complete left hand side semicircles are

54
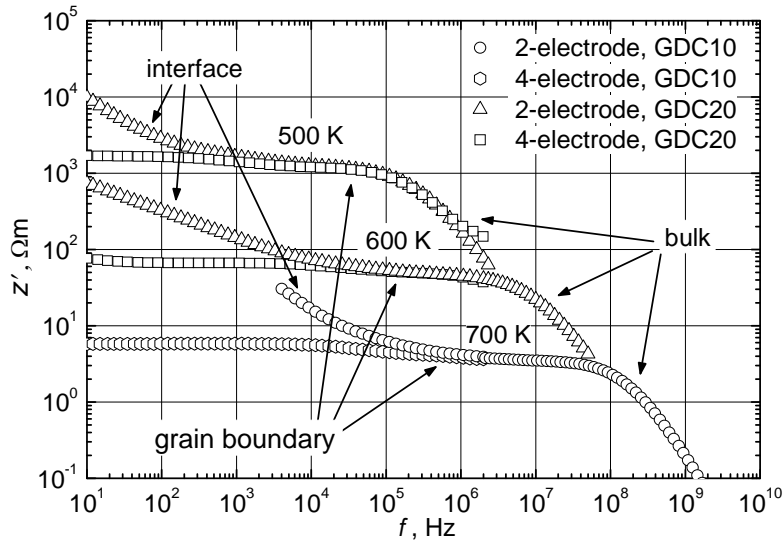
Fig. 3.1. Real part of impedance spectra for GDC10 and GDC20 ceramics sintered at 1500 and 1400 °C, respectively.

assigned to the bulk response, while low frequency tails are attributed to grain boundary medium of ceramics and electrode-electrolyte interfaces. By using 4-electrode impedance measurement method, the electrode-electrolyte interface, which relatively blocks the ionic current, was eliminated from the system and the third semicircle did not appear in the impedance spectra. As indicated in Fig. 3.2, bulk conductivities σ_b were calculated from bulk resistance values, estimated by extrapolating the rightmost ends of left hand side semicircles to the real axis. The conductivity of grain boundary medium σ_{gb} was generally considered as a reciprocal of measured specific resistance of grain boundary medium z_{gb}, which is also annotated in Fig. 3.2. Measurements of DC conductivity of ceramics and single crystals in most cases were performed by 4-electrode method. However, both 2-electrode and 4-electrode methods showed nearly identical values for DC conductivity.

Temperature dependences of bulk conductivity of studied single crystals and ceramics are presented in Fig. 3.3. Temperature ranges of measurements vary
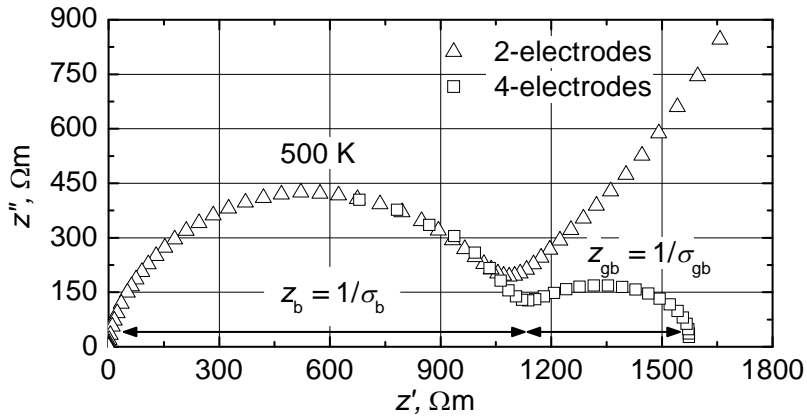
Fig. 3.2. Complex impedance plane plot for GDC20 ceramics sintered at 1400 °C.

depending on physical properties of prepared samples and equipment capabilities. The experimental data in Fig. 3.3 reveal slight change in slope towards lower activation energies at high temperatures for all the studied samples. This effect has been observed in many studies of solid oxide electrolytes [105, 126, 127] and thus different explanation models are presented in literature [126, 128]. A variation in activation energies and consistency with literature data are summarized in Table 3.1.
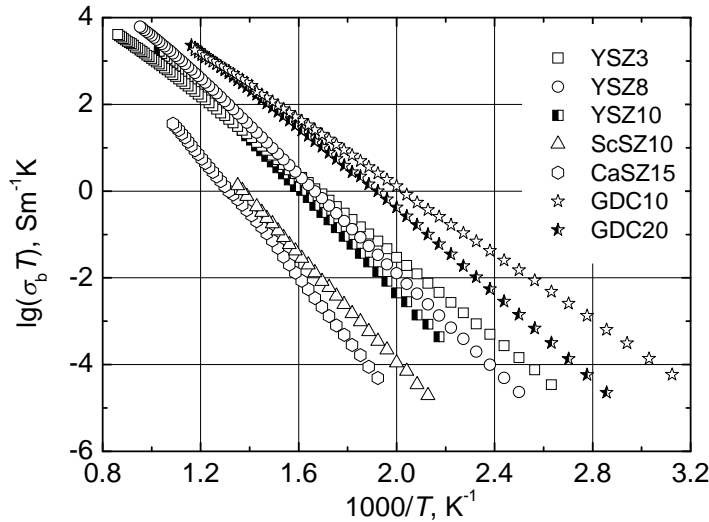
Fig. 3.3. Bulk conductivity as a function of reciprocal temperature for studied oxygen ion conductors.

Table 3.1. Average activation energies of conductivity ΔE_σ (at different temperature ranges), activation energies of relaxation time ΔE_τ and crystalline structures of the investigated materials.

This study					Literature values			
Material	Crystalline structure	Temp. range, K	ΔE_σ, eV	ΔE_τ, eV	Material	Temp. range, K	ΔE_σ, eV	Ref.
YSZ3	Monoclinic-Tetragonal [6]	380-430	0.92	0.91	YSZ3	473-773	0.95	[129]
		1110-1160	0.82			573-723	0.91	[19]
YSZ8	Cubic [6]	400-450	1.07	1.11	YSZ8	473-773	1.14	[129]
		950-1000	0.94			300-1100	1.05	[130]
YSZ10	Cubic [6]	460-510	1.23	1.18	YSZ10	300-523	0.94	[131]
		870-920	1.05			300-1100	1.22	[130]
ScSZ10	Rhombohedral-Cubic [15]	470-520	1.24	1.26	ScSZ9	573-723	1.43	[20]
		690-740	1.26		ScSZ11	723-1073	1.34	[132]
CaSZ15	Cubic [133]	520-570	1.45	1.40	CaSZ15	450-1200	1.32	[104]
		870-920	1.33			973-1998	1.26	[134]
GDC10	Cubic [135]	310-360	0.78	0.76	GDC10	298-673	0.81	[136]
		770-820	0.71			673-1173	0.72	[136]
GDC20	Cubic [135]	350-400	1.01	0.93	GDC20	473-910	0.91	[26]
		810-850	0.83			910-1073	0.51	[26]

Since the electrical properties of single crystals are not influenced by microstructure as in the case of polycrystalline ceramics, it makes sense to begin more detail analysis with the simplest case. Frequency dependences of real and imaginary parts of impedance for both single crystals are shown in Figs. 3.4-3.7. The y axes of these figures represent normalized specific impedance z/z_{DC}. The DC resistivity decreases with increasing temperature and leads to decrease in the average charge carrier relaxation time. So, the impedance dispersion region and the position of the imaginary impedance peak (z_p'') shift to higher frequencies with increase of the temperature (Figs. 3.4-3.7). Figures 3.5 and 3.7 also show a slight but regular increase of normalized impedance peak value z_p''/z_{DC} with increasing temperature. Thus semicircles of normalized impedance $z''/z_{DC} = f(z'/z_{DC})$ are slightly more depressed at lower temperatures compared to the ones at higher

57

temperatures. That indicates narrowing of the distribution of the DRT function with increasing temperature.
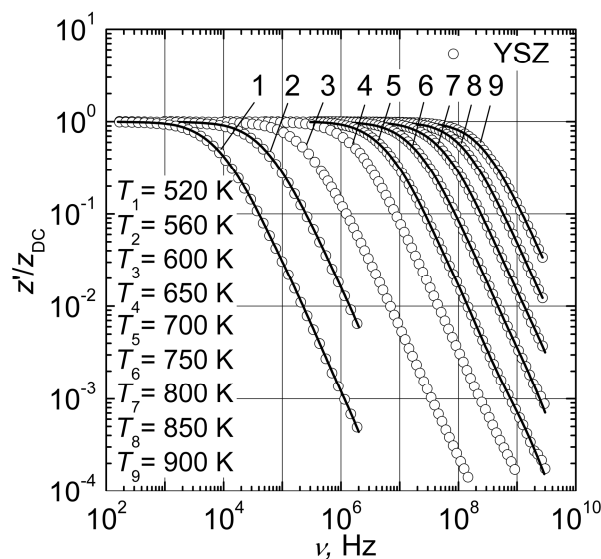
Fig. 3.4. Frequency dependencies of real part of normalized impedance. Solid lines are normalized impedance frequency dependencies calculated backwards from obtained DRT functions.
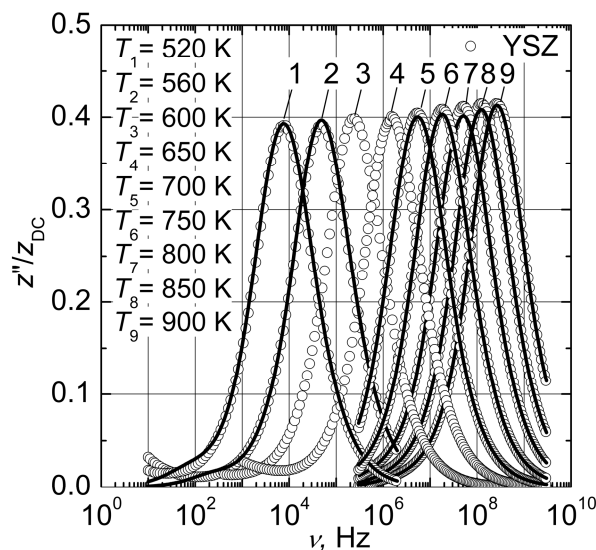
Fig. 3.5. Frequency dependencies of imaginary part of normalized impedance. Solid lines are normalized impedance frequency dependencies calculated backwards from obtained DRT functions.
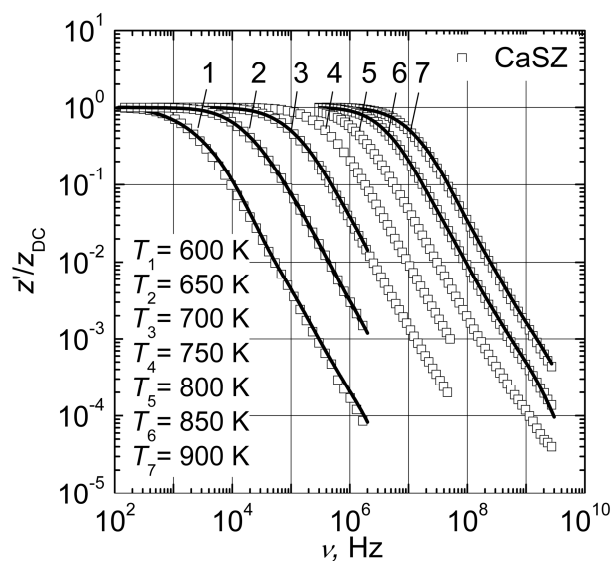
Fig. 3.6. Frequency dependencies of real part of normalized impedance. Solid lines are normalized impedance frequency dependencies calculated backwards from obtained DRT functions.
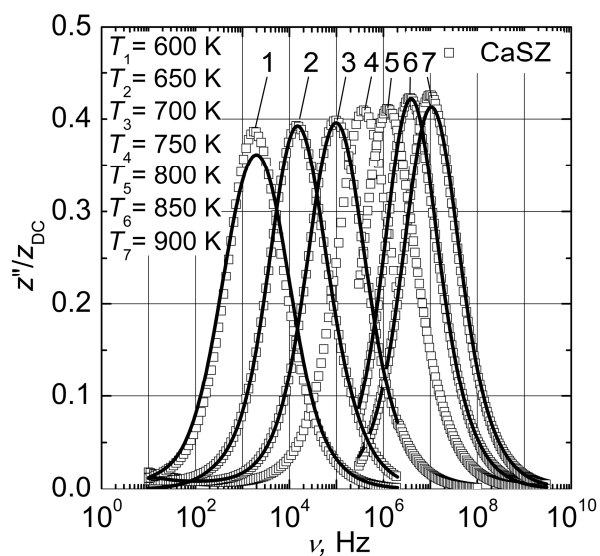
Fig. 3.7. Frequency dependencies of imaginary part of normalized impedance. Solid lines are normalized impedance frequency dependencies calculated backwards from obtained DRT functions.

The impedance spectra were further analysed in order to find the DRT function. Prior the analysis, the obtained impedance data were checked by integral Kramers-Kronig relations, which indicated sufficient quality of data. The estimated DRT functions for YSZ and CaSZ confirms narrowing of the distribution of the DRT function with increasing temperature (Figs. 3.8 and 3.9). It should be noted that the calculated DRT function is very sensitive to measurement errors. Measurement of $\tilde{z}(f)$ was carried out in two or three stages with by two sets of measurement equipment using different samples. The sample shaping, temperature measurement and other inaccuracies, accompanied by transition from one method to another, have leaded to variation of measured specific impedance data by several percent. These factors have caused critical increase of RMS error, and therefore in Figs. 3.8 and 3.9 only those DRT functions are presented, which were calculated from $\tilde{z}(f)$ data measured by single method (measured by [106] either [107]). For this reason the DRT functions in the regions around 650 K for YSZ and 750 K for CaSZ are not shown. At first sight the obtained DRT function is close to Gaussian with some low intensity peaking far from mean $\lg\tau$. For comparison, Gaussian curve and DRT function of CaSZ single crystal at 600 K are presented in Fig. 3.10. The accuracy of estimation of DRT functions represented in Figs. 3.8 and 3.9 is not good enough to define the temperature behaviour of DRT function directly from the peak width. However, a slight narrowing of DRT function with increasing temperature can be linked to increase of the DRT function's peak value at high temperatures.

RMS error of backwards calculated impedance and peak values of normalized DRT function at different temperatures for both single crystals are presented in Table 3.2. Backwards calculated frequency dependences of the normalized impedance are shown as solid lines in Figs. 3.4-3.7. Temperature dependences of z'' peak frequency (ν_p) and relaxation time at DRT function peak (τ_p) for both single crystals are presented in Fig. 3.11. Solid lines in this figure are least square linear fits of corresponding dependences. These data show nearly the Arrhenius

temperature behaviour with the activation energies close to that of σ_{DC}. The activation energies of these parameters are presented in Table 3.3.
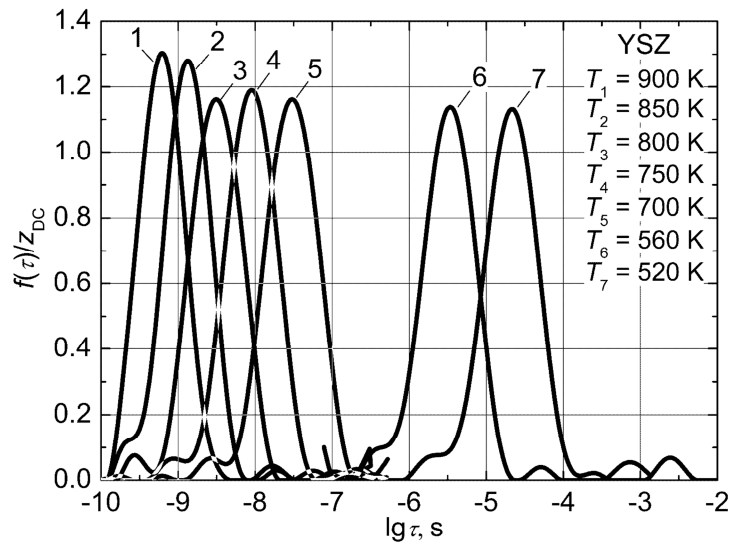
Fig. 3.8. Normalized DRT functions at different temperatures.
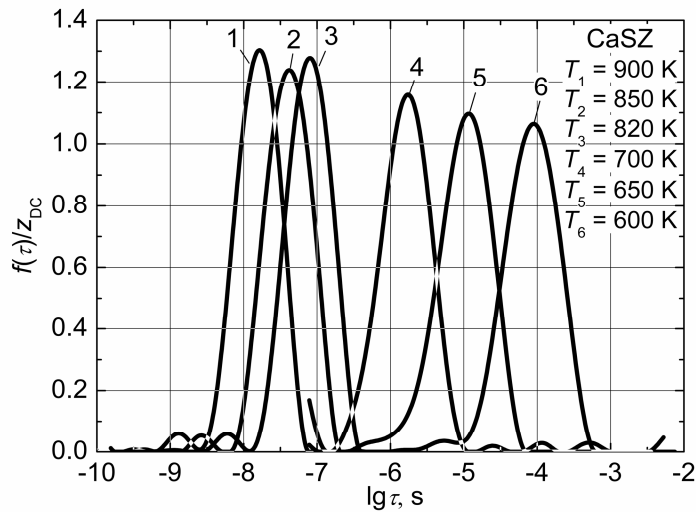
Fig. 3.9. Normalized DRT functions at different temperatures.
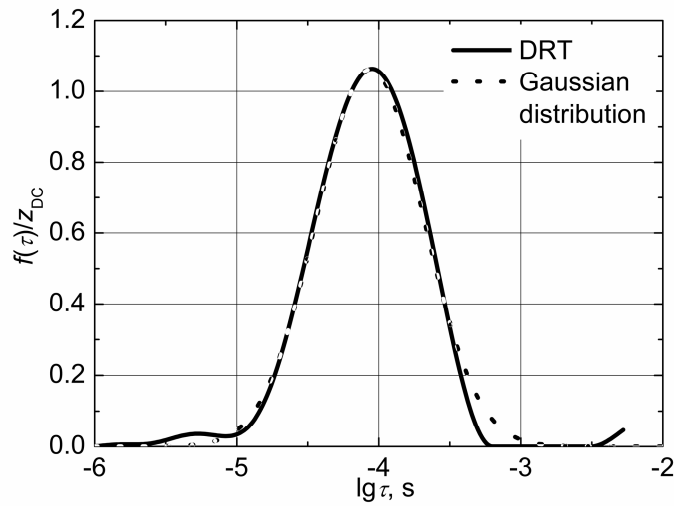
Fig. 3.10. DRT function for CaSZ at 600 K and Gaussian distribution.

Table 3.2. RMS error and DRT function's peak values.

YSZ				CaSZ			
Temperature, K	RMS error, %	$\lg\tau_p$, s	Peak value of DRT	Temperature, K	RMS error, %	$\lg\tau$ at DRT peak, s	Peak value of DRT
520	1.73	-4.66	1.13	600	3.3	-4.04	1.06
560	0.67	-5.47	1.14	650	0.79	-4.93	1.10
700	0.91	-7.52	1.16	700	0.49	-5.76	1.16
750	0.92	-8.04	1.19	820	5.5	-7.10	1.28
800	0.83	-8.51	1.16	850	2.14	-7.38	1.24
850	0.58	-8.88	1.28	900	1.22	-7.78	1.30
900	0.60	-9.21	1.31	910	0.84	-7.86	1.36

Depressed character of semicircles was also observed for polycrystalline oxygen ion conducting ceramics. As an example, complex plane plots of normalized impedance data for GDC10 ceramics at several temperatures are shown in Fig. 3.12.
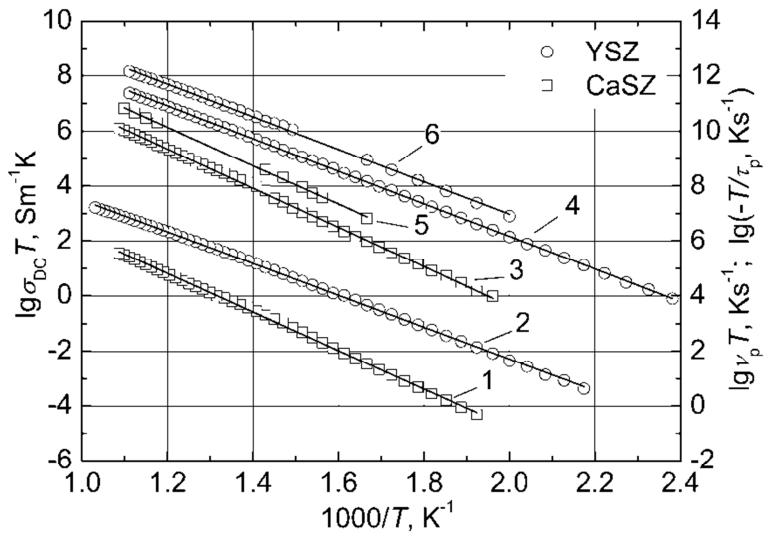
Fig. 3.11. Temperature dependences of DC conductivity (1, 2), imaginary impedance peak frequency (3, 4) and relaxation time at DRT function peak (5, 6). Solid lines are linear fit of corresponding dependences.

Table 3.3. Activation energies of $\sigma_{DC}(\Delta E_\sigma)$, v_p (ΔE_v) and τ_p (ΔE_τ).

	ΔE_σ, eV	ΔE_v, eV	ΔE_τ, eV
YSZ	1.19	1.19	1.18
CaSZ	1.40	1.43	1.40
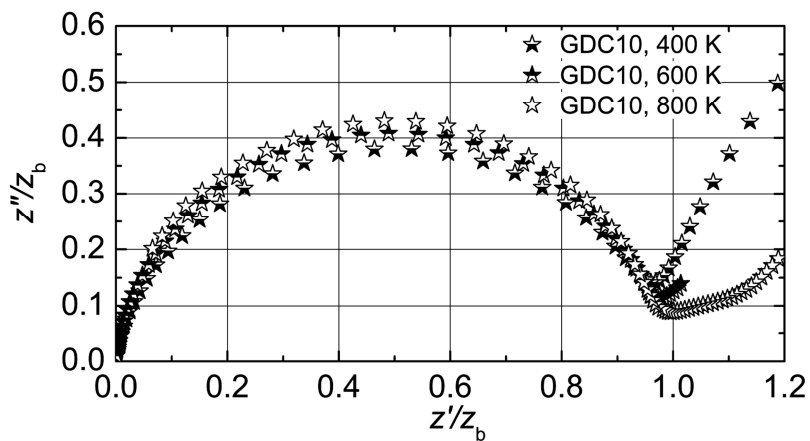
Fig. 3.12. Complex plane plots of GDC10 impedance data measured at different temperatures.
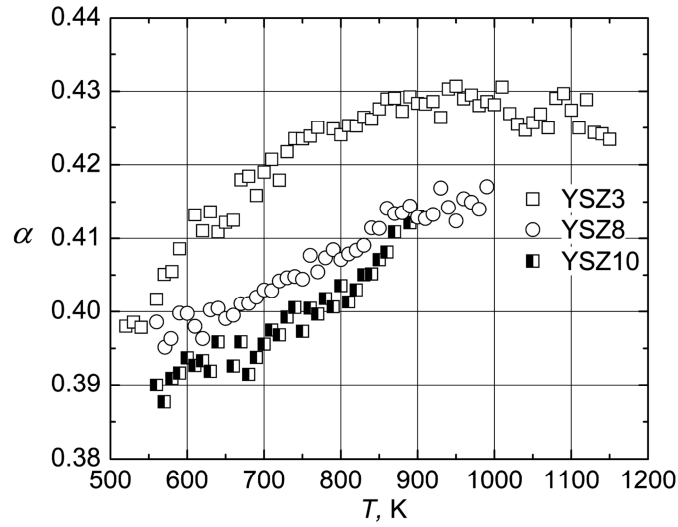
Fig. 3.13. The dependencies of $\alpha(T)$ for YSZ materials.

A degree of arcs distortion can be estimated by peak value of normalized imaginary part of impedance: $\alpha = z''_{max}/z_b$. The latter parameter can be used as a measure of the extent of this distribution: lower value indicates more widely distributed relaxation times and vice versa. Temperature dependences of α for various oxygen ion conductors are shown in Figs. 3.13 and 3.14. Results display a gradual increase of parameter α with increasing temperature for almost all the investigated compounds. Anomalous temperature dependences of YSZ3 and ScSZ10 might be caused by phase transitions occurring around 800 K temperature [6, 15]. As indicated in Fig. 3.13, the YSZ materials experience wider distribution of charge carrier relaxation times with increasing dopant concentration. This regularity also applies to findings for GDC ceramics specified in Fig. 3.14.

Narrowing of the DRT with increasing temperature and decreasing dopant concentration is consistent with solutions of DRT function, which were numerically calculated by previously described algorithm. Several of DRT functions are given in Fig. 3.15. It should be noted that the results for ceramic samples present only a part of DRT function related to charge carrier relaxation in the bulk.
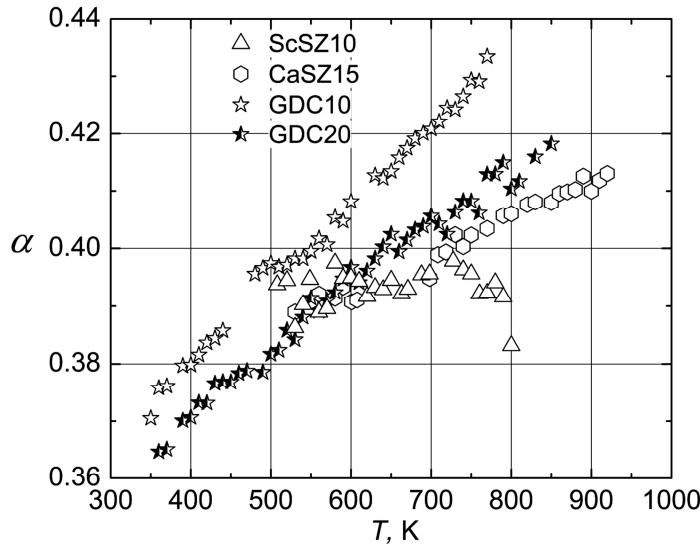
Fig. 3.14. The dependencies of $\alpha(T)$ for ScSZ10, CaSZ15, GDC10 and GDC20.

The values of maxima of these DRT functions show a tendency to increase with the temperature increase or dopant concentration decrease. The most probable relaxation times show temperature behaviour close to the Arrhenius law with activation energies comparable to that of electrical conductivities (Fig. 3.16, Tables 3.2 and 3.3).

Illustrated behaviour of the DRT function with regard to variation in dopant concentration can be caused by a change of interaction between mobile charge carrier and other lattice irregularities (dopants, associated and dissociated vacancies). These irregularities may result in microregions with distinct local dopant concentration, conductivity and charge carrier relaxation time. It may be explained by an increase of the local interaction radius, analogous to the temperature induced increase of Debye length in liquid electrolytes or solid semiconductors. E.g., the Debye length of semiconductors is given:

$$L_{\mathrm{D}} = \sqrt{\frac{\varepsilon k_{\mathrm{B}} T}{q^2 N_{\mathrm{d}}}}\,, \qquad (20)$$

65
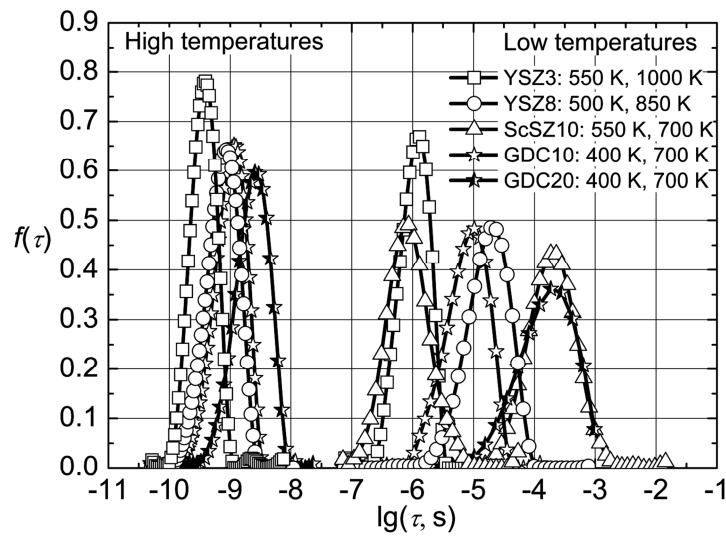
Fig. 3.15. Function $f(\tau)$ for YSZ, ScSZ and GDC at different temperatures.
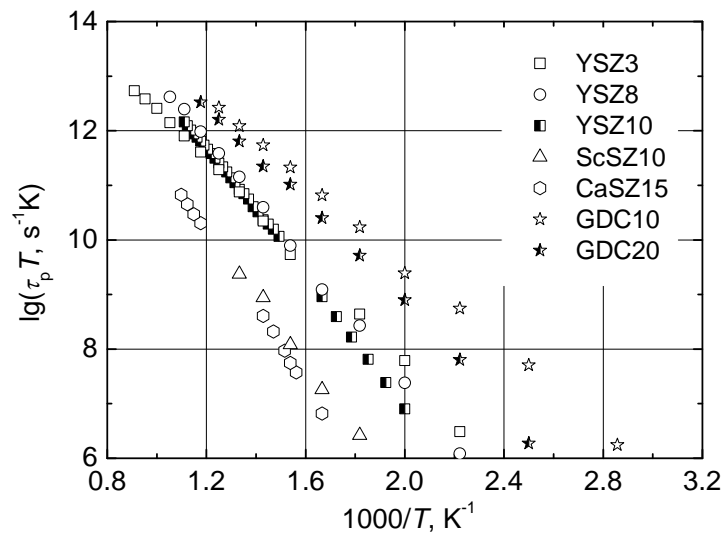
Fig. 3.16. The most probable relaxation time as a function of reciprocal temperature for studied materials.

where ε is absolute permittivity, and N_d is the concentration of dopants (either donors or acceptors). Debye length increases proportionally to the square root of the temperature and therefore increasing temperature leads to an expansion of the microregions. Charge carrier in samples with a lower lattice irregularity

concentration are further away from these irregularities, and therefore are less affected by them, making the DRT in such samples narrower and α value higher.

Summary

The electrical properties of various oxygen ion conductors were investigated in broad frequency range and temperature interval. The dispersion of electrical parameters were observed and attributed to the charge carrier relaxation in the electrical field. Small but well pronounced increases of peaks of imaginary parts of normalized impedance were found in all cases when the temperature increases and dopant concentration decreases. These findings indicate narrowing of DRTs and are consistent with results of numerical analysis of experimental data, which showed DRT function's shape in the logarithmic time scale close to the Gaussian. Temperature dependences of frequency of z'' frequency peak and most probable relaxation time (DRT function's peak) showed nearly the Arrhenius temperature behaviour with the activation energies close to that of conductivity.

3.1.2. Effect of sintering temperature

In this subsection is presented an investigation of electrical properties of GDC10 and GDC20 ceramics sintered at various temperatures from 1100 to 1500 °C for 2 h. Electrical measurements were carried out in the frequencies ranging from 100 mHz to 3 GHz and temperatures up to 850 K by combining 2- and 4-electrode methods, what allowed to identify in detail the effect of sintering temperature to the electrical properties of bulk and grain boundary medium of ceramics. Impedance spectra were also analysed by numerically calculating the DRT function.

Temperature dependences of bulk conductivity of GDC10 and GDC20 (Fig. 3.17) were found to be barely dependent on sintering temperature and the presented σ_b values apply to all the investigated ceramics. The mean bulk conductivity activation energies were found to be 0.77 and 0.90 eV for GDC10
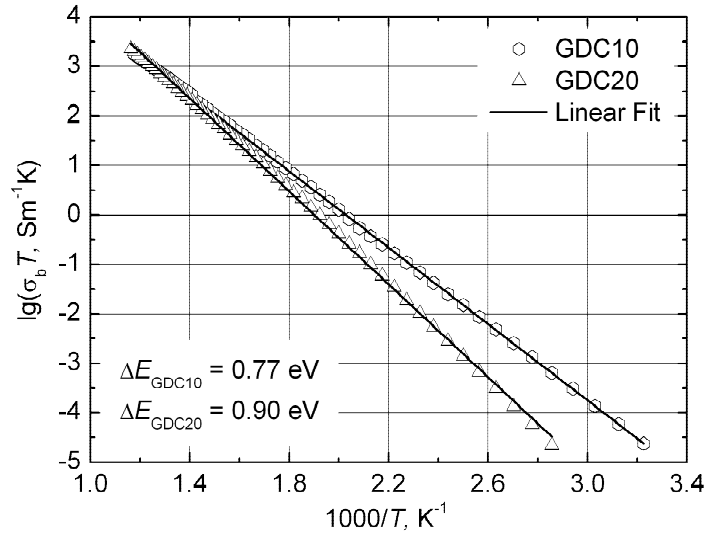
Fig. 3.17. Bulk conductivity for GDC10 and GDC20 ceramics vs. 1/*T*.

Table 3.4. Total and grain boundary conductivity values, relaxation frequencies, relative grain boundary medium volumes at 500 K temperature for investigated ceramics, and corresponding activation energies.

Material	Sintering temp., °C	σ_t, S/m (at 500 K)	σ_{gb}, S/m (at 500 K)	ΔE_{σ_gb}, eV	$f_{gb}^{(1)} \left(f_{gb}^{(2)} \right)$, kHz (at 500 K)	$\Delta E_{f\_gb}^{(1)}$ $\left(\Delta E_{f\_gb}^{(2)} \right)$, eV	$\gamma \times 10^3$ (at 500 K)
GDC10	1100	0.0013	0.0033	0.87	14.39	0.84	3.1
	1200	0.0013	0.0024	0.83	9.96	0.86	2.9
	1300	0.0016	0.0036	0.84	10.08	0.88	2.0
	1400	**0.0011**	**0.0018**	**0.81**	**3.53 (0.13)**	**0.86 (0.74)**	**-**
	1500	**0.0013**	**0.0025**	**0.81**	**8.09 (0.49)**	**0.87(0.77)**	**-**
GDC20	1100	0.0006	0.0016	0.97	13.30	0.97	5.9
	1200	0.0005	0.0011	0.94	2.88	0.94	1.9
	1300	0.0006	0.0019	0.95	3.65	0.95	1.4
	1400	0.0006	0.0021	0.95	1.73	0.95	0.6
	1500	0.0006	0.0011	0.96	0.69	0.96	1.0

and GDC20, respectively, and they are in the range of literature values of 0.72-0.90 eV for GDC10 [136-138] and 0.51-1.03 eV for GDC20 [26, 139]. Since the measurements were carried out in broad temperature range, in which the conductivity changes by 8 orders of magnitude, an uncertainty of mean activation energy was found to be roughly not more than 1 % of initial value.

The total conductivity σ_t was determined from low frequency plateau values of experimental data obtained by the 4-electrode method. A list of total conductivity values at 500 K temperature for all the investigated ceramics is given in Table 3.4. The resulting differences in σ_t values reveal certain effect of sintering temperature to properties of grain boundary medium.

As it was mentioned earlier, quantitative assessment of grain boundary medium properties is challenging due to uncertainty of its occupied volume. At first approach, specific conductivity of grain boundary medium σ_{gb} was considered as a reciprocal of measured specific resistance of grain boundary medium z_{gb}. Obtained σ_{gb} values and their activation energies ΔE_{σ_gb} for GDC10 and GDC20, some of which are presented in Fig. 3.18 and Table 3.4, did not show any obvious regularity with sintering temperature. For more detailed analysis, an estimation of proportion ratio between dimension of grain and thickness of grain boundary medium was carried out. According to the brick-layer model [60], grains were assumed to be cube-shaped with an edge length of d_g, and grain boundary medium exist as flat layers between grains with thickness of δ_{gb}. Using these assumptions, a relation of grain boundary medium's specific (σ_{gb}^{sp}) and measured (σ_{gb}^{m}) conductivities can be defined as:

$$\sigma_{gb}^{sp} = \sigma_{gb}^{m} \cdot \frac{\delta_{gb}}{d_g}. \tag{21}$$
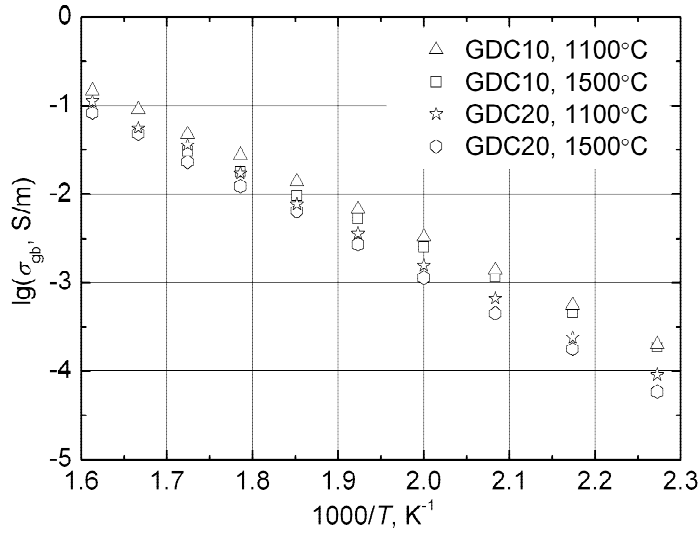
Fig. 3.18. Conductivity of grain boundary medium vs. $1/T$ for GDC10 and GDC20 ceramics sintered at various temperatures.

Furthermore, specific conductivity of grain boundary medium may be considered as a product of angular relaxation frequency ($2\pi f_{gb}$), where f_{gb} indicates frequency of respective peak in z'', and absolute permittivity of grain boundary medium ($\varepsilon_0 \varepsilon_{gb}$):

$$\sigma_{gb}^{sp} = 2\pi f_{gb} \cdot \varepsilon_0 \varepsilon_{gb}, \tag{22}$$

where ε_0 is permittivity of free space, and ε_{gb} – relative permittivity of grain boundary medium. Since it is difficult to define variation of ε_{gb} with sintering temperature, and there were no obvious causes for significant its variations, for simplicity this value was supposed to be steady: $\varepsilon_{gb} = 10$. Then ratio δ_{gb}/d_g may be estimated from Eqs. (21) and (22):

$$\frac{\delta_{gb}}{d_g} = \frac{2\pi f_{gb} \cdot \varepsilon_0 \varepsilon_{gb}}{\sigma_{gb}^m}. \tag{23}$$

The ratio δ_{gb}/d_g allows estimation of relative volume of grain boundary medium γ (volume occupied by grain boundary medium divided by total volume of sample). In general, the relative volume of grain boundary medium is

70

considered as: $\gamma = 3\delta_{gb}\big/(d_g + 3\delta_{gb})$, however, when $3\delta_{gb} << d_g$, the expression becomes:

$$\gamma \approx \frac{3\delta_{gb}}{d_g}. \tag{24}$$

Results showed consistent γ decrease with sintering temperature (Table 3.4). However, the latter methodology was found to be unsuitable for analysis of GDC10 specimens sintered at 1400 and 1500 °C. Two distinct relaxation frequencies were found for these samples in the low-frequency range, which are related to the charge carrier relaxation in grain boundary medium. In the imaginary part of impedance of 4-electrode measurement data this peculiarity manifested itself as splitted low frequency peak, as illustrated in Fig. 3.19, where one regular and two exclusive patterns for GDC10 are presented. In contrast, no similar effect was observed for GDC20, even for the specimens sintered at 1500 °C (Fig. 3.19). The respective semicircles for GDC10 sintered at high temperatures, depicted in complex plane plot, also appear to be distorted (inset, Fig. 3.19). Although the splitting of relaxation frequencies is most clearly evident in the imaginary part of impedance (Fig. 3.19), the identification of peak frequencies directly from this part of data is rather complicated.

Therefore more extensive analysis of this occurrence was carried out by numerically calculating the DRT function directly from impedance spectra obtained by 4-electrode method. The latter analysis estimates system's time domain behaviour, which in this case was found to be more evident than the frequency domain. The obtained DRT functions contained a single peak at frequencies attributed to processes in grain boundary medium for all the investigated ceramics except for GDC10 ceramics sintered at 1400 and 1500 °C. The findings are shown in Table 3.4, where specimens possessing two relaxation centres are indicated by bold, and in Fig. 3.20, where a comparison of a few regular and these two exclusive patterns of DRT function is presented. Vertical arrows in Figs. 3.19 and 3.20 mark the peaks of the probability density of charge carrier relaxation times, locations of which refers to the most probable

71
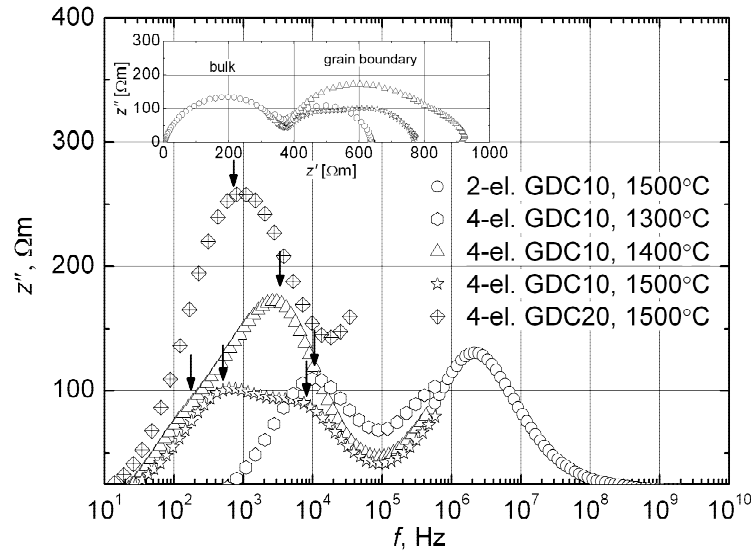
Fig. 3.19. Imaginary part of impedance spectra for ceramics sintered at 1300, 1400 and 1500 °C at 500 K. Vertical arrows mark locations of estimated relaxation frequencies. Inset: Respective complex plane plots at 500 K for GDC10 ceramics.

characteristic relaxation times. Top scale in Fig. 3.20 relates the obtained DRT functions to relaxation frequency, which is inversely proportional to relaxation time: $f = 1/2\pi\tau$. The higher (or the only one) most probable relaxation frequency was defined as the main relaxation frequency $f_{gb}^{(1)}$ of grain boundary medium and the remaining (if any) – as secondary relaxation frequency $f_{gb}^{(2)}$ of grain boundary medium. Since the 4-electrode data covered a limited frequency range, only parts of DRT functions are presented, which are mainly related to the charge carrier relaxation in grain boundary medium. The frequencies $f_{gb}^{(1)}$ and $f_{gb}^{(2)}$ were found to be very close and the impedance spectra in certain cases contained only moderate number of frequency points. Therefore, the identification of them was rather difficult. So only an approximate estimation of temperature dependences of these frequencies was extracted from the obtained impedance spectra.

72
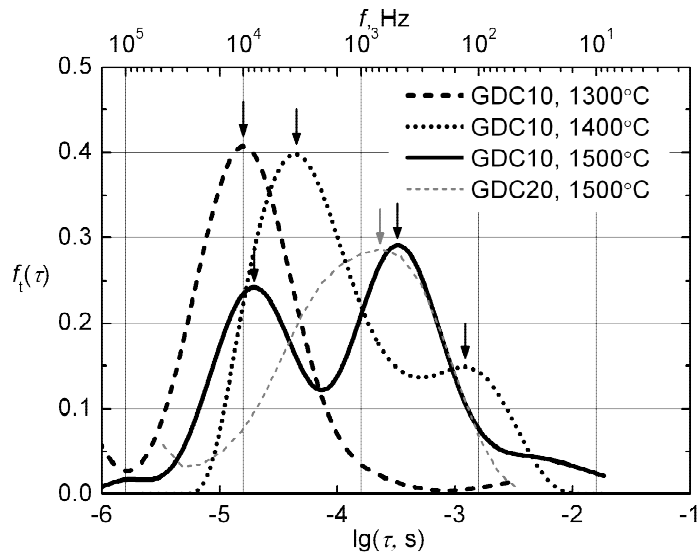
Fig. 3.20. DRT functions at 500 K for GDC10 sintered at different temperatures. Vertical arrows mark most probable relaxation times of charge carriers.
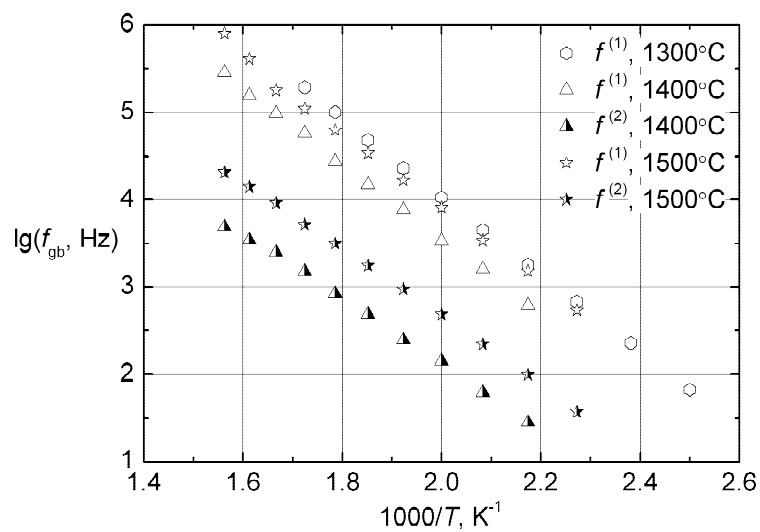
Fig. 3.21. Relaxation frequencies of grain boundary medium vs. $1/T$ for GDC10 ceramics sintered at 1300, 1400 and 1500 °C.

As presented in Fig. 3.21, the determined values of the main relaxation frequencies for GDC10 show very similar temperature behaviour to that of conductivity of grain boundary medium. All the Arrhenius plots of relaxation frequencies for GDC10 and GDC20 give activation energies in close agreement with the values obtained for conductivity of grain boundary medium (Table 3.4). Secondary relaxation frequencies of particular specimens were found to have slightly lower values of activation energy $\left(\Delta E^{(2)}_{f\_gb}\right)$ and considerably smaller absolute values, which may indicate presence of another medium type in the grain boundary medium of the ceramics. Since the latter effect is observed in ceramics sintered at relatively high temperatures, it can be assumed that at such temperatures the grain boundary medium may form two phases, which reveals itself as two different relaxation centres. However, confirmation of this conclusion by structural characterization is complicated due to low quantity of grain boundary medium, which was found to be less than 0.6 % of the sample (Table 3.4).

Summary

GDC10 and GDC20 ceramics with different electrical properties of the grain boundary medium were produced by altering the sintering temperature from 1100 to 1500 °C. The obtained conductivity values of grain boundary medium did not show any regularity with sintering temperature. The relaxation frequencies of charge carrier in the grain boundary medium for most of the specimens were found to exhibit the Arrhenius behaviour with activation energies close to these of conductivity of grain boundary medium. More detailed analysis of the proportion ratio between grain dimension and thickness of grain boundary medium, based on the brick-layer model, showed a consistent decrease of relative volume of grain boundary medium with sintering temperature for all the investigated ceramics. The ceramic samples sintered at 1400 and 1500 °C also showed a particular character of frequency dispersion of electrical properties caused by oxygen ion relaxation in grain boundary medium. Numerical analysis of the experimental data for these ceramics revealed two relaxation frequencies attributed to the charge

carrier relaxation in grain boundary medium, which suggests that the grain boundary medium consists of two phases with different electrical properties.

3.1.3. Vicinity of phase transition

This subsection presents a detailed study of electrical properties of ScSZ10 ceramic samples in wide temperature range, which covers a phase transition region. Temperature behaviour of specific conductivity and permittivity in bulk, and both specific and total conductivities in grain boundary medium is discussed. Peculiarities of DRT function for mobile ions are also investigated in detail using Tikhonov regularization technique.

Polycrystalline ScSZ10 samples were sintered at 1500 °C temperature in air atmosphere for 1h. Microstructure of samples was characterized using SEM. As it is shown in Fig. 3.22, grain size of obtained specimens was in the range of few microns. Crystal structure of ceramics was determined at different temperatures by XRD. Initial analysis of the samples at room temperature showed that the principal phase of the pattern is rhombohedral (β-phase) (Fig. 3.23); low intensity peaks of cubic phase were also observed (Fig. 3.23, inset), which is typical for this kind of material [140, 141].
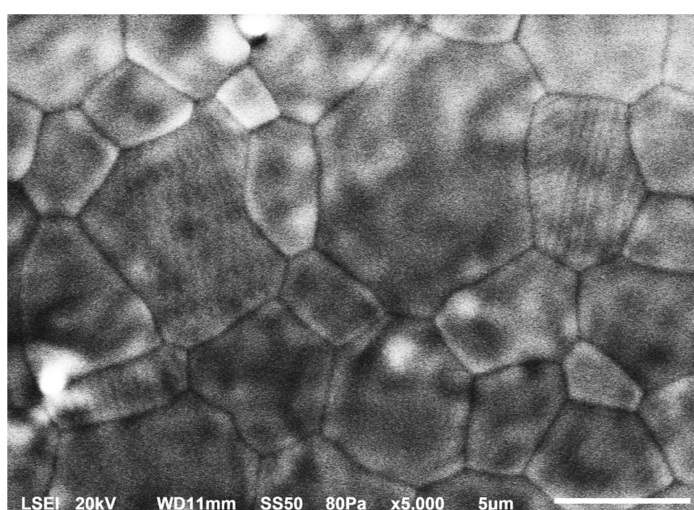
Fig. 3.22. SEM image of sintered 10ScSZ ceramics.
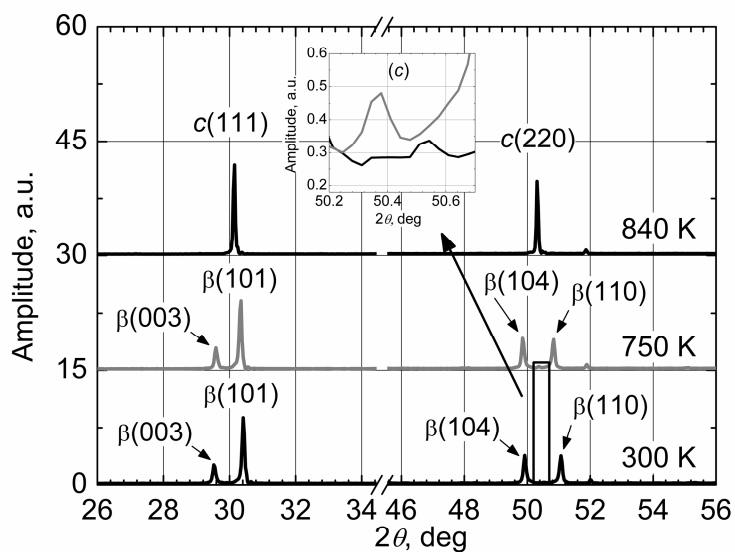
Fig. 3.23. X-ray diffraction patterns of ScSZ10 ceramics sintered at 1500 °C. Inset: low intensity cubic phase peaks.
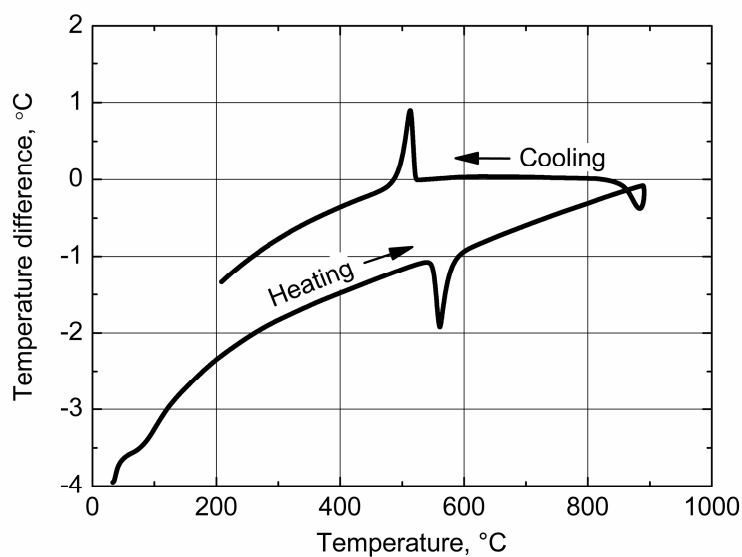
Fig. 3.24. DTA curve for ScSZ10 ceramics.

DTA of obtained ceramic sample showed an endothermic peak at 834 K and exothermic one – at 786 K temperatures upon heating and cooling cycles, respectively (Fig. 3.24), i.e. considerable thermal hysteresis was observed. The

transition temperatures itself slightly depend on heating/cooling rate, and at 20 K/min thermal hysteresis loop was found to be of value around 48 K. XRD study at 840 K temperature (Fig. 3.23) detected single *c*-phase of the sample. However, it should be noted that distinct studies indicate different phase transition temperatures, what are explained by effect of grain size of sintered ceramic specimens to character of ScSZ phase transitions [140, 141].
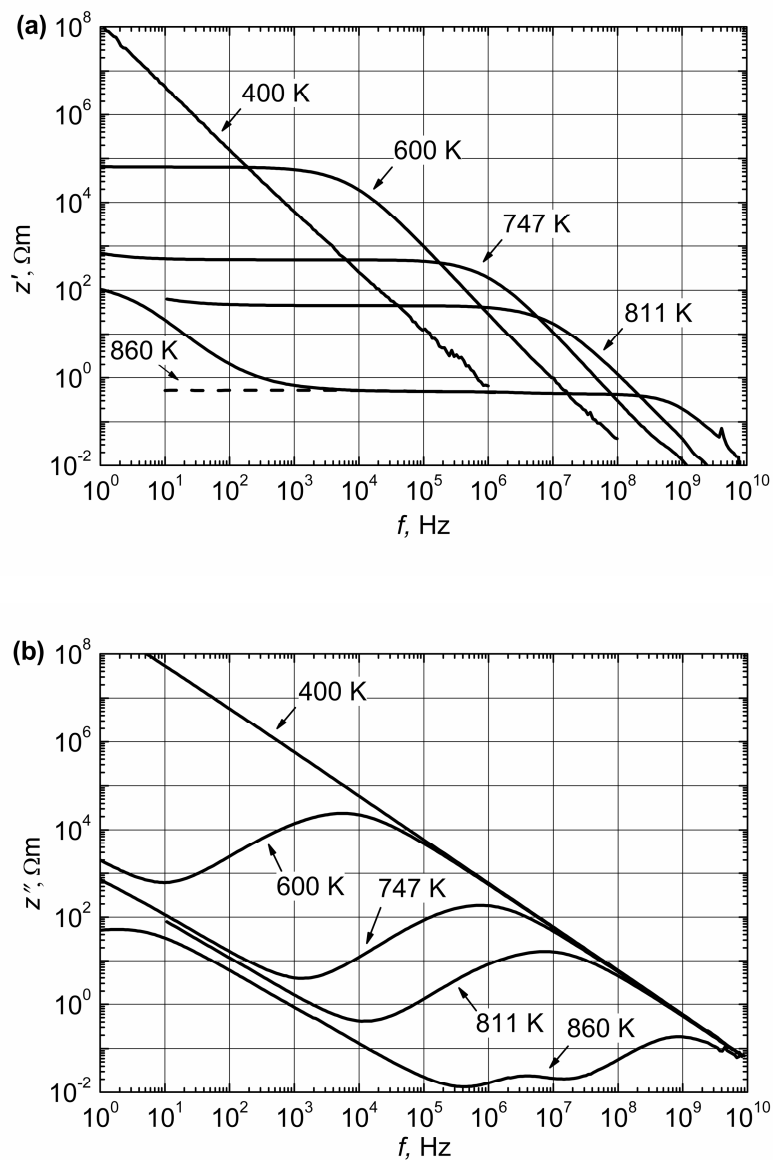
Fig. 3.25. Spectra of real (a) and imaginary (b) parts of ScSZ10 impedance at various temperatures.

Electrical parameters of ceramics were extracted from measured ultra-broadband spectra (Fig. 3.25). Temperature dependences of DC conductivities of bulk σ_b and grain boundary medium σ_{gb}^m of studied ceramics are shown in Fig. 3.26 (curve 1). In this case conductivity of grain boundary medium is referred to as measured conductivity of grain boundary medium σ_{gb}^m in order to distinguish it from its specific conductivity of grain boundary medium σ_{gb}^{sp}. Temperature dependences of σ_b and σ_{gb}^m at temperatures far from phase transition were found to obey the Arrhenius law with activation energies of $\Delta E_{b\beta} = 1.30$ eV (in β-phase) and $\Delta E_{bc} = 0.93$ eV, $\Delta E_{tgbc} = 1.49$ eV (in c-phase), respectively (Table 3.5).

Table 3.5. Activation energies of conductivity and mean relaxation frequency.

	β-phase		c-phase	
	ΔE^b, eV	ΔE^{gb}, eV	ΔE^b, eV	ΔE^{gb}, eV
σ	1.30	1.44	0.93	1.49
f	1.27	1.26	0.96	1.46

A jump in grain conductivity value σ_b of several orders of magnitude was observed nearby phase transition (800-820 K upon heating and 790-810 K upon cooling, respectively). The observed anomalies correspond to the DTA peaks (Fig. 3.24). These changes also cause a sharp increase in permittivity, as shown in Fig. 3.27. The figure shows temperature dependences of high frequency limit permittivity and real part of permittivity measured at frequencies of 1 and 4.8 GHz. Presented ε_∞ values were obtained from complex plane plots of modulus by extrapolating high frequency end of semicircular arcs to real axis and calculating reciprocal value. Abrupt alteration of $\varepsilon_\infty(T)$ in the phase transition region indicates change of elastic polarization, which suggests a structural phase transition. The major part of change in $\varepsilon(T)$ at 1 and 4.8 GHz frequencies around phase transition is caused by impact of mobile ions.
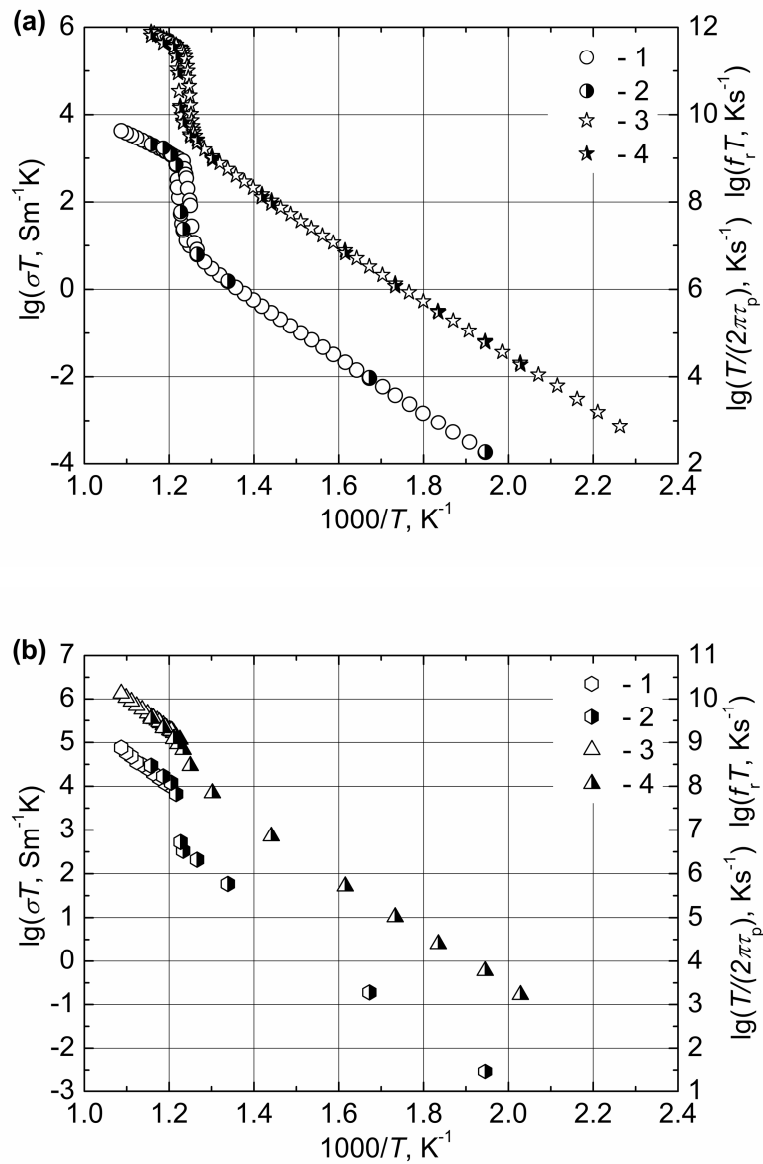
Fig. 3.26. Arrhenius plots of conductivity and charge carriers relaxation frequency for bulk (a) and grain boundary medium (b): 1 – specific bulk and measured grain boundary medium conductivities determined from corresponding semicircles in complex plane plots; 2 – specific bulk and measured grain boundary medium conductivities determined from DRT function; 3 – bulk and grain boundary medium imaginary impedance peak frequencies; 4 – bulk and grain boundary medium most probable relaxation frequencies determined from DRT function peaks.
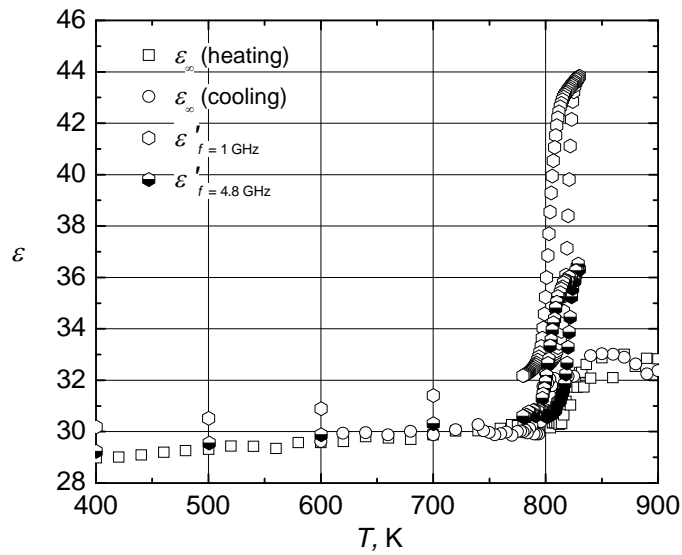
Fig. 3.27. Temperature dependences of high frequency limit permittivity and real part of permittivity at 1 and 4.8 GHz.

Figure 3.28 presents complex plane plot of ScSZ normalized (divided by z_b) impedance at temperatures far from (a) and around (b) the phase transition region. Both figures show z'' and z' data at frequencies covering bulk and grain boundary medium dispersion. In β-phase only one semicircle is observed, which seems to belong to charge carrier relaxation in the bulk of ceramics.

In c-phase a second semicircle at the low frequency side of the plots emerged, which can be related to processes in grain boundary medium. Due to DRT of charge carrier, all the observed semicircles are depressed. At temperatures far from phase transition, deformation of the high frequency arc decreases with increasing temperature, which indicates narrowing of the DRT function. Analogous phenomenon in YSZ, GDC and other oxygen ion conductors was described in subsection 3.1.1. According to the current results, while approaching phase transition temperature, the deformation of high frequency semicircle starts to increase, then follows the decrease along with arise of second arc. Such pulsating shape behaviour of the mentioned semicircle is illustrated by parameter

80
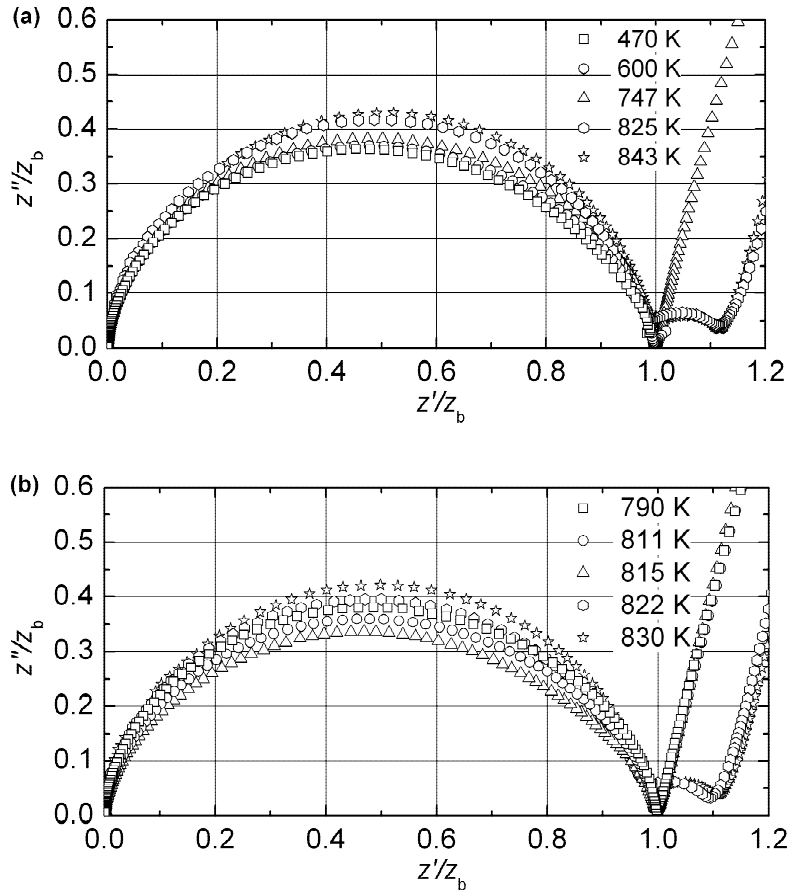
Fig. 3.28. Complex impedance plane plots at temperatures far from phase transition region (a) and in phase transition region (b).

α (introduced in section 3.1.1.) in Fig. 3.29. As it was mentioned, this parameter directly indicates the extent of the DRT: lower value corresponds more widely distributed relaxation times and vice versa. An increase of parameter α with increasing temperature (far from phase transition temperature) is clearly seen. However, there is a deviation from such behaviour of parameter α at phase transition temperature region. The presented temperature dependence of α has a clear minimum (Fig. 3.29), located in the vicinity of phase transition, which indicates broadening of the DRT. This occurrence can be caused by increase of local conductivity fluctuations at the phase transition temperature region.

It also can be expected, that charge carrier relaxation times in the bulk and grain boundary medium of ceramics are very close in their values in the rhombohedral β-phase. Since in this case resistivity of grain boundary medium is
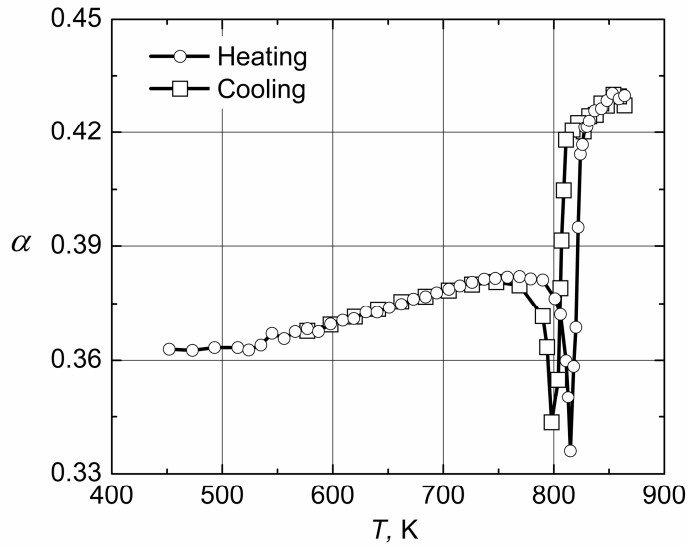
Fig. 3.29. Temperature dependence of α parameter.

very low, both relaxation processes can't be separated. In phase transition region, average relaxation time in grain interior becomes much smaller, while the one of grain boundary medium changes much less. When the difference between both average relaxation times become significant (in c-phase), this comes out as two dispersion regions, and semicircle in impedance complex plane plot splits into two (Fig. 3.28). The latter remarks are illustrated by Fig. 3.30, where the DRT functions of ScSZ10 ceramics at different temperatures are shown.

As can be seen, the value of the main peak of the DRT function shows a regular increase with increasing temperature at temperatures far from phase transition (it is indicated by a slight decrease of DRT function width) and a clear minimum at phase transition temperature, respectively. The second peak of DRT function is observed even in β-phase, whereas it is difficult to notice any manifestation of second relaxation process in impedance data (Figs. 3.25 and 3.28). This result is slightly unexpected and at first there was a doubt about its certainty. The DRT functions were obtained solving Eqs. (15a) and (15b) by Tikhonov method, which in some cases provides solutions with small spurious peaks. Extent of these peaks is usually up to several percent of the main peak, while position depends on experimental data correctness and setting of

regularization parameter λ, as indicated in sections 2.3. and 3.1.1. However, in this case the magnitude of secondary peak was higher than 10 % of the main peak value and there was only weak response to regularization parameter change. Moreover, the temperature dependence of most probable relaxation frequency in grain boundary medium (Fig. 3.26 (b), curve 4) nearly obeys the Arrhenius law with activation energy: $\Delta E_{gb\beta}$=1.26 eV, which gradually passes to ΔE_{gbc}= 1.46 eV (Table 3.5) after the transition to c-phase. The latter part of this curve is in agreement with data obtained directly from peak position of z'' in frequency dependences, what shows reliability of the presented results. Consequently, total DRT function of ScSZ10 ceramics can be considered as a sum of two components:

$$f_t(\tau) = f_b(\tau) + f_{gb}(\tau),\tag{25}$$

where $f_b(\tau)$ and $f_{gb}(\tau)$ define distribution of relaxation times in the bulk and grain boundary medium, respectively. In this context it is useful to rewrite Eq. (7) in normalized form:

$$\frac{\tilde{z}(0)}{z_{DC}} = \int_{-\infty}^{\infty} \left(f_b(\tau) + f_{gb}(\tau)\right) d\lg(\tau) = \int_{-\infty}^{\infty} f_b(\tau) d\lg(\tau) + \int_{-\infty}^{\infty} f_{gb}(\tau) d\lg(\tau) = 1,\tag{26}$$

where $z_{DC} = z_b + z_{gb}$.
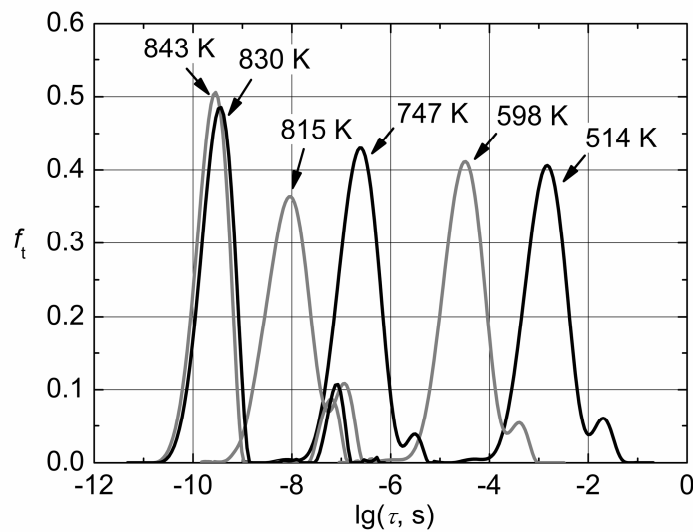
Fig. 3.30. DRT functions at different temperatures.

83

Thus these functions contain information about contributions of the bulk and grain boundary medium's resistances to the overall resistivity z_{DC}. In *c*-phase both resistances can be determined directly from semicircles in complex plain plots (Fig. 3.28), representing different charge carrier relaxation processes. However, only one semicircle is observed in low temperature phase and the only way to find these components is to separate these two parts of DRT function and take advantage of Eq. (26).
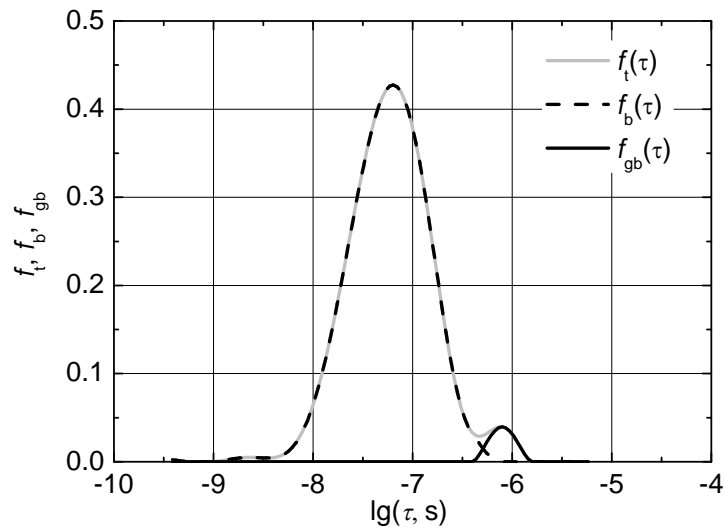
Fig. 3.31. Extraction of bulk and grain boundary medium DRT functions at 790 K for ScSZ10 ceramics.

It was assumed that function $f_{gb}(\tau)$ is symmetric with respect to its peak and the right side of this function is unaffected by $f_b(\tau)$ (Fig. 3.31). According to this assumption, shape of function $f_{gb}(\tau)$ was extracted at different temperatures and contribution of grain boundary medium to total resistivity was determined by integrating this function. Temperature dependence of reciprocal parameter to the contribution of z_{gb}^m (i.e. measured conductivity of grain boundary medium $\sigma_{gb}^m = 1/z_{gb}^m$) is presented in Fig. 3.26 (b) (curve 2). However, accuracy of this method depends on many factors, including character of the impedance spectra,

values of measurement error and selection of the value of the regularization parameter λ.

It is slightly surprising that measured conductivity of grain boundary medium σ_{gb}^{m} and mean charge carrier relaxation frequency f_{gb} in grain boundary medium's also show sudden changes (of about a half and of one order of magnitude, respectively) in phase transition temperature region. However, according to Eq. (22), a jump in specific conductivity of the grain boundary medium should occur, because there is almost no probability for significant change of permittivity during phase transition. Thus jump in σ_{gb}^{m} is higher than that in σ_{gb}^{sp}, what probably means increase $\leftrightarrow$ decrease of effective volume of grain boundary medium during $\beta \leftrightarrow c$ phase transition, respectively. In low temperature phase, grain boundary medium may be partially fallen out of charge carrier transport path due to anisotropic conduction in the bulk. Another plausible cause of this effect could be a change in thickness of grain boundary medium induced by the phase transition in the bulk of ceramics. The jump in specific conductivity of grain boundary medium may be caused by change in strain of grain boundary medium. Local crystal structure in the interface bulk-grain boundary medium environment also could transform during phase transition and probably affect σ_{gb}^{sp}.

In general, Eq. (22) also can be applied for bulk of ceramics. Thus the values of activation energies of conductivity and relaxation frequency should be very close in all cases. However, as can be seen from Table 3.5, grain boundary medium in β-phase distinguished themselves by more significant difference between values of mentioned activation energies. The more rapid increase of σ_{gb}^{m}, comparing to that of σ_{gb}^{sp}, could be a consequence of temperature dependent extent of effective volume of grain boundary medium. For example, detailed analysis of XRD data shows an increase of low intensity peaks of cubic phase in β-ScSZ10 with increasing temperature (Fig. 3.23, inset). If c-phase is located in the interface bulk-grain boundary medium, it may alter the thickness of grain boundary medium. It should be noted that the latter difference in activation energy values

could also be affected by accuracy of determination of measured conductivity and mean relaxation frequency of grain boundary medium.

Summary

Dense ScSZ10 ceramic samples were sintered with grain size of about 10 μm. A rhombohedral phase was detected in this compound at room temperature, which undergoes transformation to the cubic phase at around 800-820 K. Abrupt changes in specific grain conductivity and permittivity were found as a consequence of this phase transition.

The dispersion of electrical parameters was also observed in broad frequency and temperature ranges and attributed to the charge carrier relaxation in the electrical field. The DRT function in the bulk, which was determined by numerical analysis of experimental data, was found to be narrower with increasing temperature at temperatures far from the phase transition point in both rhombohedral and cubic phases. An increase of width of the DRT function was observed in the phase transition temperature region, which could arise as a consequence of increase of local conductivity fluctuations. The measured conductivity and average charge carrier relaxation frequency of grain boundary medium were found from DRT function data. Obtained data indicated jump of specific and measured conductivities of grain boundary medium in the phase transition region, which suggests that crystal structure of the crystallites affect electrical properties of grain boundary medium.

3.2. Relationship between charge carrier relaxation and peculiarities of electric response

This section continues study of electrical properties and DRT function behaviour of solid oxygen ion conductors, listed in Table 1.1. The data presented here was obtained by previously mentioned ultra-broadband impedance spectrometer capable of measurements at frequencies up to 10 GHz. An analysis
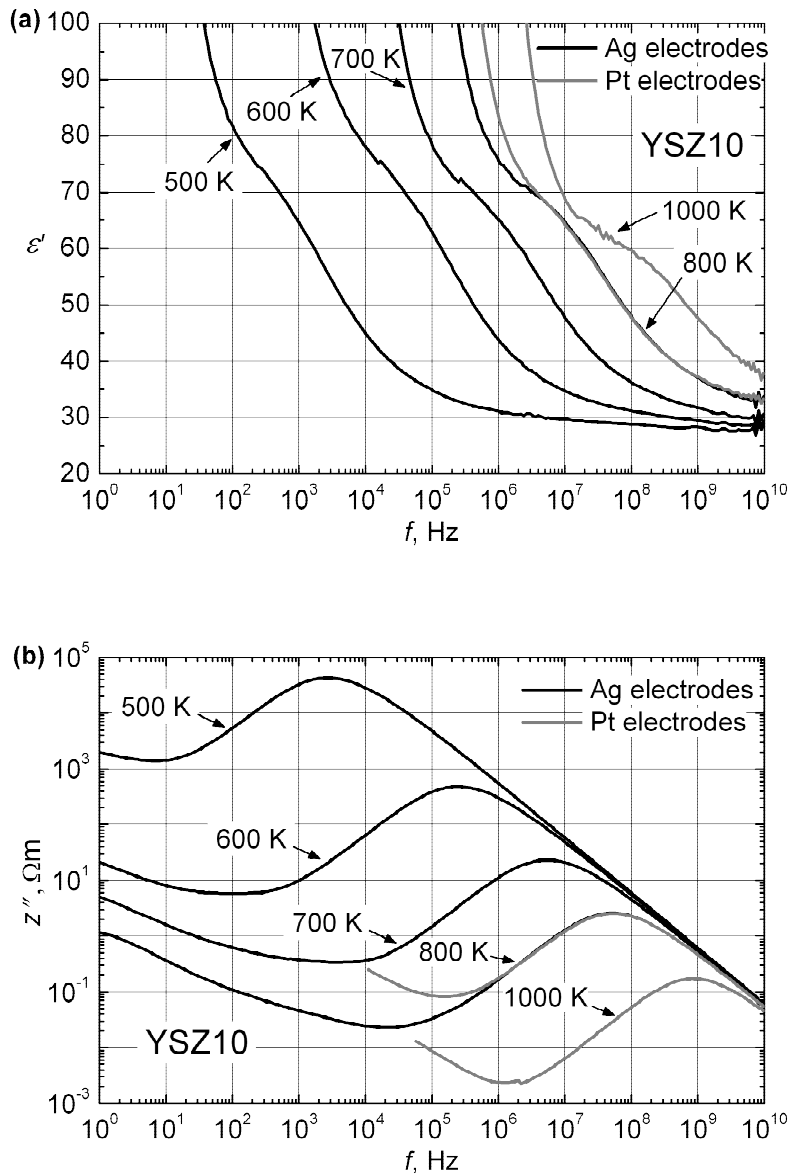
Fig. 3.32. The frequency dependences of the real part of permittivity (a) and the imaginary part of impedance (b) of the YSZ10 single crystal at various temperatures.

of experimental data allowed to observe peculiarities of the behaviour of permittivity and ratio of characteristic frequencies (frequencies of imaginary part's peaks) of electrical modulus (f_m) and impedance (f_z). As it will be shown, these two parameters are related to the DRT function of conductive system and they can be employed for determination of behaviour of the DRT function.

The frequency dependences of the real part of permittivity and imaginary part of impedance for YSZ10 and CaSZ15 single crystals at various temperatures are presented in Figs. 3.32 and 3.33, respectively. As it is seen in these illustrations, characteristic frequency f_z increases with increasing temperature. High values of z'' and ε' at low frequencies (Figs. 3.32 and 3.33) are mainly due to interfacial effects at the electrode-electrolyte interface. In the microwave frequency range, permittivity asymptotically approaches its high frequency limit, but in the intermediate frequency range, at frequencies $f < f_z$, a plateau of ε' appears. Similar effects in oxygen ion conductors, as well as in conductive glasses and polymers, were also observed in other studies [76, 130, 142-144]. There is an inherent problem with finding the plateau value of ε_s, which arises due to the interference of frequency regions of the plateau and the neighbouring interfacial dispersion. The interference was only slightly reduced by using Ag electrodes, which shifted the interfacial dispersion region to lower frequencies (Figs. 3.32 and 3.33).

Since the replacement of electrode material did not show sufficient effect, another methodology for estimating the plateau value of real part of permittivity was developed, which is based on the analysis of the DRT function. The DRT function in this study was estimated by improved algorithm, which allows determining of the DRT function with a significantly lower minimization error than that demonstrated in subsection 3.1.1. According to methodology for estimation of ε_s, at first the DRT function $f(\tau)$ (Fig. 3.34) is found. Despite the restricted frequency range of the data used for the DRT function calculation, a small impact of the interface in region of long relaxation times is observed in most cases. Reliability of the results can be verified by backward calculation of impedance from initial function $f(\tau)$, utilizing Eqs. (15a) and (15b). In particular, the permittivity was calculated from impedance data using formula:

$$\tilde{\varepsilon} = \frac{1}{i\omega\varepsilon_0\tilde{z}}. \tag{27}$$
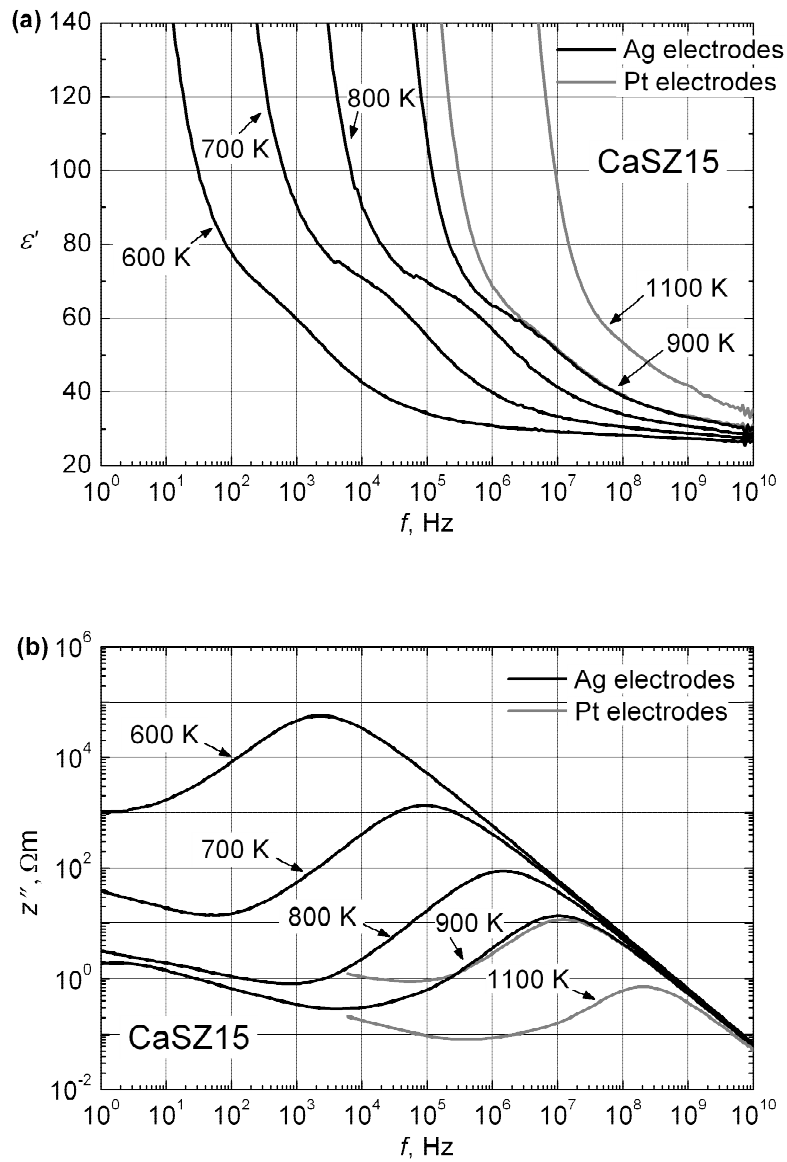
Fig. 3.33. The frequency dependences of the real part of permittivity (a) and the imaginary part of impedance (b) of the CaSZ15 single crystal at various temperatures.

The obtained results, an example of which is represented by solid line in Fig. 3.35, sufficiently coincide with initial experimental data in the frequency range, used for finding $f(\tau)$. However, the effect of electrode-electrolyte interface is clearly noticeable in the initial and backward calculated spectra of ε' and z''. Therefore, the restricted DRT functions $f_R(\tau)$ were obtained by zeroing values of

$f(\tau)$ in the region of long relaxation times (Fig. 3.34, region (b)). The spectra of ε' and z'', which were backward calculated from these restricted DRT functions $f_R(\tau)$, did not show any impact of the electrode-electrolyte interface (Fig. 3.35, dashed lines). This allowed one to easily determine the plateau value ε_s of the real part of permittivity.
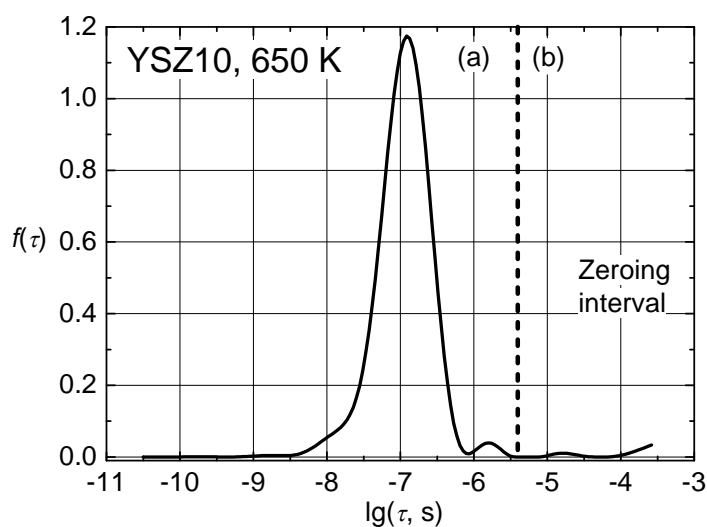
Fig. 3.34. The DRT function of YSZ10 single crystal at 650 K. The restricted DRT function was obtained by zeroing function in the region (b).

Since the experimental and backward calculated results showed very good agreement in the relevant frequency range, the examined frequency responses of YSZ10 and CaSZ15 single crystals can be well described by Eqs. (15a) and (15b). Thus the observed behaviour of real part of permittivity (Fig. 3.35(a), solid line) may be considered as a typical frequency response of distributed conductive system with DRT function, shaped close to that shown in Fig. 3.34.

The calculated standard deviation σ_R of $f_R(\tau)$ for YSZ10 and CaSZ15 single crystals is presented in Fig. 3.36. A decrease of σ_R with increasing temperature is consistent with the findings presented in subsections 3.1.1. and 3.1.3., which indicated narrowing of the DRT function in zirconia and ceria-based oxygen ion
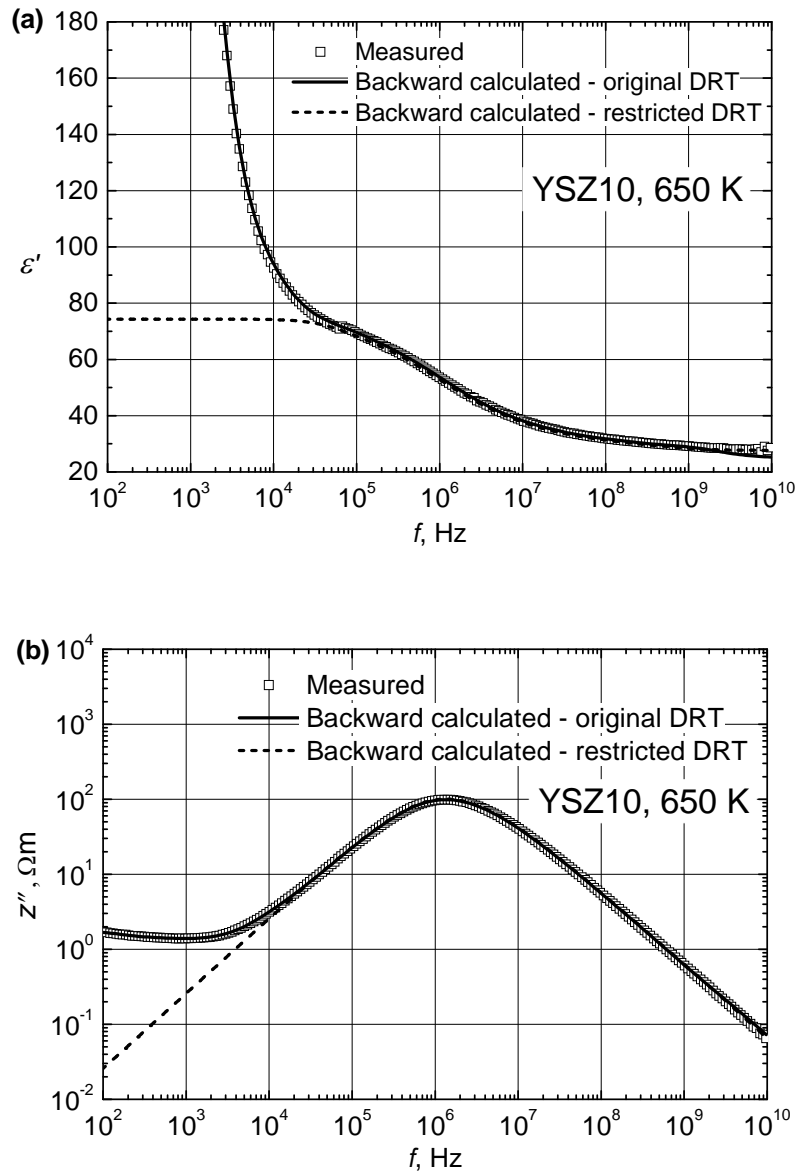
Fig. 3.35. Frequency dependences of the real part of permittivity (a) and the imaginary part of impedance (b) of YSZ10 single crystal at 650 K, as measured and backward calculated from original and restricted DRT functions.

conductors with increasing temperature. The dependences of $\varepsilon_s(T)$ for both single crystals are also shown in Fig. 3.36. The value of ε_s depends on temperature with a similar character as σ_R, exhibiting a decrease with increasing temperature. According to Eqs. (15a), (15b) and (27):

$$\tilde{\varepsilon} = \cfrac{1}{i\omega\varepsilon_0 z_b \displaystyle\int\limits_{-\infty}^{\infty} f(\tau)\cfrac{1-i\omega\tau}{1+\omega^2\tau^2}\,d\lg(\tau)} \cdot \qquad (28)$$
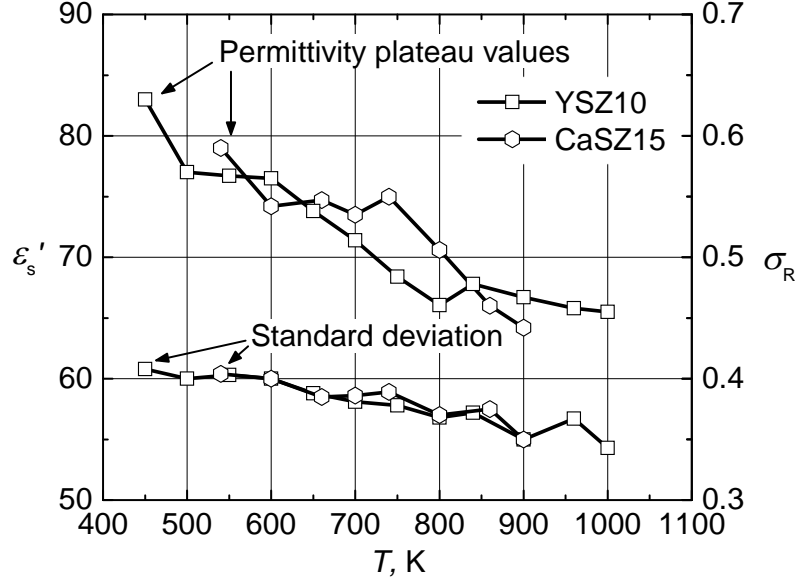
Fig. 3.36. The temperature dependences of plateau value of real part of permittivity, and standard deviation of the DRT function for YSZ10 and CaSZ15 single crystals.

For a given relaxation mechanism, one can write low and high frequency limits of permittivity:

$$\varepsilon_s = \lim_{\omega \to 0}[\mathrm{Re}(\tilde{\varepsilon})], \qquad (29a)$$

$$\varepsilon_\infty = \lim_{\omega \to \infty}[\mathrm{Re}(\tilde{\varepsilon})]. \qquad (29b)$$

Having in mind that:

$$\int\limits_{-\infty}^{\infty} f(\tau)\,d\lg(\tau) = 1 \qquad (30)$$

and in accordance with the Eqs. (28), (29a) and (29b), it may be shown, that:

$$\varepsilon_s = \frac{1}{\varepsilon_0 z_b}\int\limits_{-\infty}^{\infty}\tau f(\tau)\,d\lg(\tau) = \frac{<\tau>}{\varepsilon_0 z_b}, \qquad (31a)$$

$$\varepsilon_\infty = \cfrac{1}{\varepsilon_0 z_b \displaystyle\int_{-\infty}^{\infty} \cfrac{1}{\tau} f(\tau)\, d\lg(\tau)} = \cfrac{1}{\varepsilon_0 z_b \left< \cfrac{1}{\tau} \right>}. \qquad (31b)$$

Here $<\tau>$ and $<\cfrac{1}{\tau}>$ are mean and mean reciprocal relaxation times of mobile charge carrier, respectively. Thus:

$$\frac{\varepsilon_s}{\varepsilon_\infty} = <\tau><\frac{1}{\tau}>. \qquad (32)$$

High frequency limit permittivity is determined by elastic polarization and barely depends on the system of mobile ions. Thereby Eq. (32) indicates that ε_s is higher for a system with more distributed τ. Thus the temperature dependence of plateau value of real part of permittivity may be considered as an indicator of temperature behaviour of the DRT function of conductive system.

However, the latter procedure for estimating temperature behaviour of the DRT function for ceramic materials is complicated due to strong interference of ε_s with permittivity component, caused by the intercrystalline dispersion. For a direct characterization of the DRT function in case of ceramic materials, it is more appropriate to use directly measurable parameter – ratio $r = f_m/f_z$, where f_m corresponds to peak value of the imaginary part of electric modulus.

For the electric modulus m one can write:

$$m(\omega) = i\varepsilon_0 \omega \tilde{z}(\omega) = \int_{-\infty}^{\infty} \frac{f(\tau)\varepsilon_0 z_b}{\tau} \frac{\omega^2 \tau^2 + i\omega\tau}{1 + \omega^2 \tau^2} d\lg(\tau) = \int_{-\infty}^{\infty} g(\tau) \frac{\omega^2 \tau^2 + i\omega\tau}{1 + \omega^2 \tau^2} d\lg(\tau). \quad (33)$$

Here:

$$g(\tau) = \frac{f(\tau)}{\tau} \varepsilon_0 z_b. \qquad (34)$$

Let one assume that the probability density functions $f(\tau)$ and $g(\tau)$ have maxima at argument values τ_z and τ_m, respectively. In the frequency domain these parameters determine locations of the peaks of imaginary parts of impedance and electrical modulus at frequencies $f_z \approx 1/2\pi\tau_z$ and $f_m \approx 1/2\pi\tau_m$, respectively. It may be shown from Eq. (34), that $\tau_m < \tau_z$ and at the same time $f_m > f_z$. In case of

bell-shaped $f(\lg(\tau))$ (as shown in Fig. 3.34), when $f(\tau)$ broadens then τ_m decreases and ratio $\tau_z/\tau_m \approx f_m/f_z$ increases. Assume, for example, that the DRT function is normally distributed on a logarithmic scale:

$$f(\tau) = \frac{1}{\sigma_n \sqrt{2\pi}} \exp\left(-\frac{\lg\tau - \lg\tau_z}{2\sigma_n}\right)^2.$$ (35)

It may be shown, that in this case the standard deviation σ_n is proportional to logarithm of ratio r:

$$\sigma_n^2 \propto \lg\frac{\tau_z}{\tau_m} \approx \lg\frac{f_m}{f_z}.$$ (36)

The temperature dependences of $r(T)$ for YSZ10 and CaSZ15 single crystals, as well as for various zirconia and ceria ceramics, are shown in Fig. 3.37. In all cases the parameter r decreases with increasing temperature, which indicates narrowing of the DRT function. Figure 3.37 also shows correlation between the ratio r and the dopant concentration. The ratio r for YSZ and GDC compounds increases (i.e. the DRT function widens) with increasing dopant concentration. Similar findings, obtained by completely different methods, are presented in subsections 3.1.1. and 3.1.3. There is a huge $r(T)$ peak in the temperature region 800-820 K for ScSZ10 ceramics (Fig. 3.37(a)). It was also already shown, that in this temperature range a structural $\beta \leftrightarrow c$ ScSZ10 phase transition takes place, which is accompanied by a significant broadening of the DRT function. According to Eq. (36), this behaviour must be followed by an increase of the ratio r.

Consequently, the temperature behaviour of the DRT function in studied oxygen ion conductors may be estimated not only from the extent of the distortion of complex impedance arcs or computing the DRT function directly, as carried out in section 3.1. The same can be accomplished by estimating the plateau of real part of permittivity at intermediate frequencies or the ratio r, which corresponds to the characteristic frequencies of peak values of the imaginary parts of electric modulus and impedance. Estimation of plateau value requires advanced data
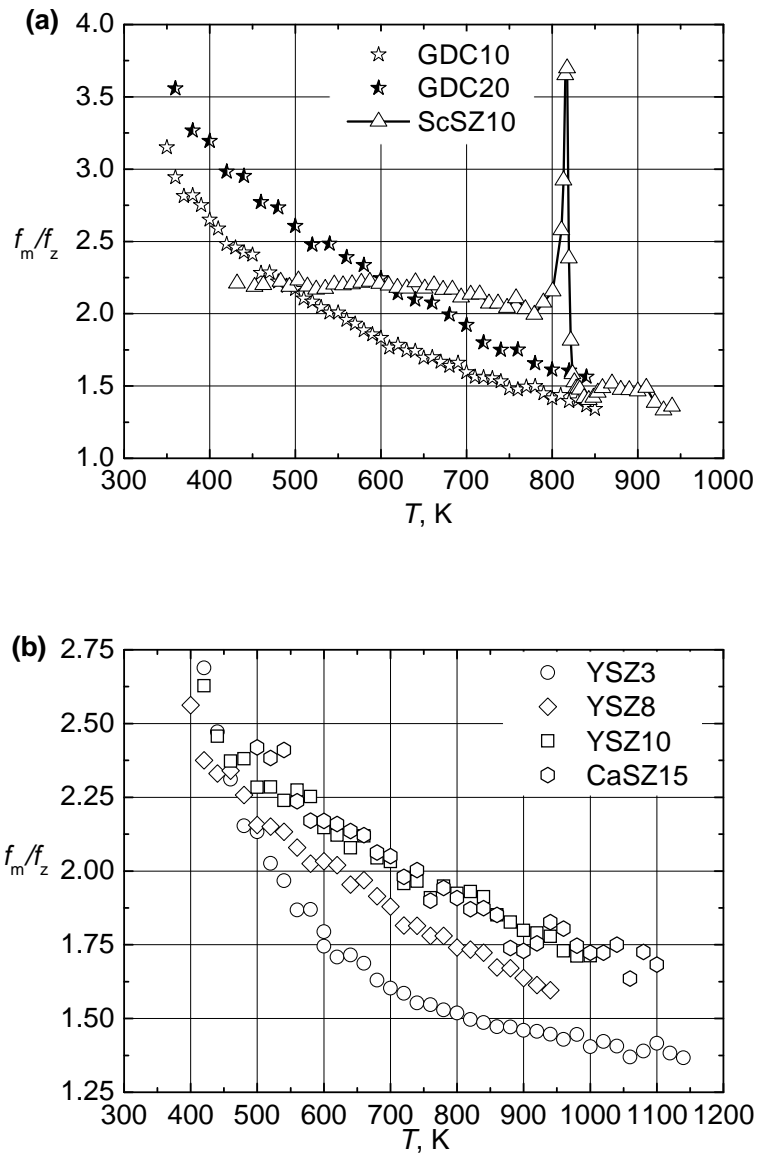
Fig. 3.37. The temperature dependences of $r = f_m/f_z$ ratio of the investigated oxygen ion conductors.

processing due effect of interfacial dispersion and is more suitable for single crystals, while the plateau of permittivity in ceramics is strongly affected by neighbouring dispersion related to grain boundary medium. Measurement of parameter r is applicable both to single crystal and ceramic samples. Moreover, the parameters f_m and f_z are directly measurable and data in considerably

narrower frequency range is sufficient in order to find peculiarities of the DRT function compared to case of dealing with the distortion of complex impedance arcs.

Summary

The electrical properties of various oxygen ion conductors were investigated in broad frequency and temperature ranges. In the frequency region $f < f_z$ the plateau of real part of permittivity, interfering with the interfacial dispersion, was observed for YSZ10 and CaSZ15 single crystals. This plateau is characteristic frequency response feature of conducting system with distributed relaxation times. Narrowing of the DRT functions with increasing temperature were observed for both single crystals. This was reflected in the plateau of real part of permittivity and in the directly measurable ratio $r = f_m / f_z$, the decrease of which was observed with temperature increase.

Conclusions

Fluorite-structure oxygen ion conducting ceramics (YSZ, CaSZ, ScSZ, GDC) were sintered at various temperatures from 1100 to 1500 °C. The ceramics as well as YSZ and CaSZ single crystals were studied by IS and the obtained data were further analysed by newly developed algorithm in order to find the DRT function. ScSZ ceramics were also studied by SEM, DTA and XRD. The investigations led to the following conclusions:

1. The DRT function in oxygen ion conducting ceramics and single crystals contain nearly Gaussian-shaped curve in logarithmic time scale, which narrows with increasing temperature and decreasing dopant concentration.
2. The distribution of relaxation times in scandia-stabilized zirconia significantly broadens in the vicinity of structural phase transition.
3. The 10 mol% gadolinia-doped ceria ceramics, sintered at 1400 and 1500 °C, exhibit two relaxation frequencies attributed to the charge carrier relaxation in grain boundary medium, which indicates that the grain boundary medium consists of two phases with different electrical properties.
4. The width of the DRT function in oxygen ion conductors is related to the ratio of characteristic frequencies, which correspond to peak values of the imaginary parts of electric modulus and impedance.

References

[1] A. Kežionis, S. Kazlauskas, D. Petrulionis, A.F. Orliukas, Broadband Method for the Determination of Small Sample's Electrical and Dielectric Properties at High Temperatures, IEEE Transactions on Microwave Theory and Techniques 62, 2456-2461 (2014).

[2] S.M. Áron Varga, Fuel Cells, DoITPoMS, University of Cambridge (2006).

[3] E.J.L. Schouler, N. Mesbahi, G. Vitter, In situ study of the sintering process of yttria stabilized zirconia by impedance spectroscopy, Solid State Ionics 9–10(2), 989-996 (1983).

[4] S.P.S. Badwal, F.T. Ciacchi, Oxygen-ion conducting electrolyte materials for solid oxide fuel cells, Ionics 6, 1-21 (2000).

[5] S.P.S. Badwal, Grain boundary resistivity in zirconia-based materials: effect of sintering temperatures and impurities, Solid State Ionics 76, 67-80 (1995).

[6] H.G. Scott, Phase relationships in the zirconia-yttria system, Journal of Materials Science 10, 1527-1535 (1975).

[7] T.H. Etsell, S.N. Flengas, Electrical properties of solid oxide electrolytes, Chemical Reviews 70, 339-376 (1970).

[8] S.P.S. Badwal, Zirconia-based solid electrolytes: microstructure, stability and ionic conductivity, Solid State Ionics 52, 23-32 (1992).

[9] A. Nakamura, J.B. Wagner, Defect Structure, Ionic Conductivity, and Diffusion in Calcia-Stabilized Zirconia, Journal of The Electrochemical Society 127, 2325-2333 (1980).

[10] B.C.H. Steele, Appraisal of $Ce_{1-y}Gd_yO_{2-y/2}$ electrolytes for IT-SOFC operation at 500°C, Solid State Ionics 129, 95-110 (2000).

[11] N. Wang, H. Chen, H. He, W. Norimatsu, M. Kusunoki, K. Koumoto, Enhanced thermoelectric performance of Nb-doped $SrTiO_3$ by nano-inclusion with low thermal conductivity, Scientific Reports 3, (2013).

[12] O. Yamamoto, Solid oxide fuel cells: fundamental aspects and prospects, Electrochimica Acta 45, 2423-2435 (2000).

[13] E. Ivers-Tiffée, A. Weber, D. Herbstritt, Materials and technologies for SOFC-components, Journal of the European Ceramic Society 21, 1805-1811 (2001).

[14] D.W. Strickler, W.G. Carlson, Electrical Conductivity in the ZrO_2-Rich Region of Several M_2O_3—ZrO_2 Systems, Journal of the American Ceramic Society 48, 286-289 (1965).

[15] R. Ruh, H.J. Garrett, R.F. Domagala, V.A. Patel, The System Zirconia-Scandia, Journal of the American Ceramic Society 60, 399-403 (1977).

[16] O. Yamamoto, Y. Arati, Y. Takeda, N. Imanishi, Y. Mizutani, M. Kawai, Y. Nakamura, Electrical conductivity of stabilized zirconia with ytterbia and scandia, Solid State Ionics 79, 137-142 (1995).

[17] F.T.C. S.P.S Badwal, D Milosevic, Scandia–zirconia electrolytes for intermediate temperature solid oxide fuel cell operation, Solid State Ionics 136-137, 91-99 (2000).

[18] T.Y. Tien, Grain Boundary Conductivity of Zr0.84Ca0.16O1.84 Ceramics, Journal of Applied Physics 35, 122-124 (1964).

[19] S.P.S. Badwal, F.T. Ciacchi, K.M. Giampietro, Analysis of the conductivity of commercial easy sintering grade 3 mol% Y2O3–ZrO2 materials, Solid State Ionics 176, 169-178 (2005).

[20] S.P.S. Badwal, F.T. Ciacchi, S. Rajendran, J. Drennan, An investigation of conductivity, microstructure and stability of electrolyte compositions in the system 90 mol% (Sc2O3–Y2O3)–ZrO2(Al2O3), Solid State Ionics 109, 167-186 (1998).

[21] J.M. Ralph, A.C. Schoeler, M. Krumpelt, Materials for lower temperature solid oxide fuel cells, Journal of Materials Science 36, 1161-1172 (2001).

[22] H. Okamoto, Ce-O (Cerium-Oxygen), Journal of Phase Equilibria and Diffusion 29, 545-547 (2008).

[23] G.B. Balazs, R.S. Glass, ac impedance studies of rare earth oxide doped ceria, Solid State Ionics 76, 155-162 (1995).

[24] H. Inaba, H. Tagawa, Ceria-based solid electrolytes, Solid State Ionics 83, 1-16 (1996).

[25] M. Mogensen, N.M. Sammes, G.A. Tompsett, Physical, chemical and electrochemical properties of pure and doped ceria, Solid State Ionics 129, 63-94 (2000).

[26] M.A.F. Öksüzömer, G. Dönmez, V. Sariboğa, T.G. Altinçekiç, Microstructure and ionic conductivity properties of gadolinia doped ceria (GdxCe1−xO2−x/2) electrolytes for intermediate temperature SOFCs prepared by the polyol method, Ceramics International 39, 7305-7315 (2013).

[27] M.G. Chourashiya, J.Y. Patil, S.H. Pawar, L.D. Jadhav, Studies on structural, morphological and electrical properties of Ce1−xGdxO2−(x/2), Materials Chemistry and Physics 109, 39-44 (2008).

[28] S. Zha, C. Xia, G. Meng, Effect of Gd (Sm) doping on properties of ceria electrolyte for solid oxide fuel cells, Journal of Power Sources 115, 44-48 (2003).

[29] F.-Y. Wang, B.-Z. Wan, S. Cheng, Study on Gd3+ and Sm3+ co-doped ceria-based electrolytes, Journal of Solid State Electrochemistry 9, 168-173 (2005).

[30] X. Guan, H. Zhou, Z. Liu, Y. Wang, J. Zhang, High performance Gd3+ and Y3+ co-doped ceria-based electrolytes for intermediate temperature solid oxide fuel cells, Materials Research Bulletin 43, 1046-1054 (2008).

[31] V.V. Ivanov, V.R. Khrustov, Y.A. Kotov, A.I. Medvedev, A.M. Murzakaev, S.N. Shkerin, A.V. Nikonov, Conductivity and structure features of Ce1−xGdxO2−δ solid electrolytes fabricated by compaction and sintering of weakly agglomerated nanopowders, Journal of the European Ceramic Society 27, 1041-1046 (2007).

[32] T. Kudo, H. Obayashi, Mixed Electrical Conduction in the Fluorite-Type Ce1−x Gd x O2−x/2, Journal of The Electrochemical Society 123, 415-419 (1976).

[33] C. Peng, Z. Zhang, Nitrate–citrate combustion synthesis of Ce1−xGdxO2−x/2 powder and its characterization, Ceramics International 33, 1133-1136 (2007).

[34] Z. Tianshu, P. Hing, H. Huang, J. Kilner, Ionic conductivity in the CeO2–Gd2O3 system (0.05≤Gd/Ce≤0.4) prepared by oxalate coprecipitation, Solid State Ionics 148, 567-573 (2002).

[35] Y.-P. Fu, Y.-S. Chang, S.-B. Wen, Microwave-induced combustion synthesis and electrical conductivity of Ce1−xGdxO2−1/2x ceramics, Materials Research Bulletin 41, 2260-2267 (2006).

[36] G. Chiodelli, L. Malavasi, V. Massarotti, P. Mustarelli, E. Quartarone, Synthesis and characterization of Ce0.8Gd0.2O2−y polycrystalline and thin film materials, Solid State Ionics 176, 1505-1512 (2005).

[37] M. Gödickemeier, L.J. Gauckler, Engineering of Solid Oxide Fuel Cells with Ceria-Based Electrolytes, Journal of The Electrochemical Society 145, 414-421 (1998).

[38] A. Atkinson, Chemically-induced stresses in gadolinium-doped ceria solid oxide fuel cell electrolytes, Solid State Ionics 95, 249-258 (1997).

[39] M.H.I. Yasuda, Ionic and Mixed Conducting Ceramics III, The Electrochemical Society, Pennington, NJ, 1998.

[40] F.M.B. Marques, L.M. Navarro, Performance of double layer electrolyte cells Part II: GCO/YSZ, a case study, Solid State Ionics 100, 29-38 (1997).

[41] A. Tsoga, A. Gupta, A. Naoumidis, D. Skarmoutsos, P. Nikolopoulos, Performance of a double-layer CGO/YSZ electrolyte for solid oxide fuel cells, Ionics 4, 234-240 (1998).

[42] T. Matsui, M. Inaba, A. Mineshige, Z. Ogumi, Electrochemical properties of ceria-based oxides for use in intermediate-temperature SOFCs, Solid State Ionics 176, 647-654 (2005).

[43] S.H. Chan, X.J. Chen, K.A. Khor, A simple bilayer electrolyte model for solid oxide fuel cells, Solid State Ionics 158, 29-43 (2003).

[44] S. Hui, J. Roller, S. Yick, X. Zhang, C. Decès-Petit, Y. Xie, R. Maric, D. Ghosh, A brief review of the ionic conductivity enhancement for selected oxide electrolytes, Journal of Power Sources 172, 493-502 (2007).

[45] T. Kudo, H. Obayashi, Oxygen Ion Conduction of the Fluorite-Type Ce1−x Ln x O2−x/2 (Ln = Lanthanoid Element), Journal of The Electrochemical Society 122, 142-147 (1975).

[46] H. Yahiro, Y. Baba, K. Eguchi, H. Arai, High Temperature Fuel Cell with Ceria-Yttria Solid Electrolyte, Journal of The Electrochemical Society 135, 2077-2080 (1988).

[47] T.J. Kirk, J. Winnick, A Hydrogen Sulfide Solid-Oxide Fuel Cell Using Ceria-Based Electrolytes, Journal of The Electrochemical Society 140, 3494-3496 (1993).

[48] Ceramic Materials and Components for Energy and Environmental Applications: Ceramic Transactions, John Wiley & Sons, 2010.

[49] C.-W. Kuo, Y.-H. Shen, I.M. Hung, S.-B. Wen, H.-E. Lee, M.-C. Wang, Effect of Y2O3 addition on the crystal growth and sintering behavior of YSZ nanopowders prepared by a sol–gel process, Journal of Alloys and Compounds 472, 186-193 (2009).

[50] K. Reddy, K. Karan, Sinterability, Mechanical, Microstructural, and Electrical Properties of Gadolinium-Doped Ceria Electrolyte for Low-Temperature Solid Oxide Fuel Cells, Journal of Electroceramics 15, 45-56 (2005).

[51] B. Stawarczyk, M. Özcan, L. Hallmann, A. Ender, A. Mehl, C.F. Hämmerlet, The effect of zirconia sintering temperature on flexural strength, grain size, and contrast ratio, Clinical Oral Investigations 17, 269-274 (2013).

[52] S.M.L. You Na Ko, Jung Hyun Kim, Jung-Kul Lee and Yun Chan Kang, Sintering characteristics of nano-sized yttria-stabilized zirconia powders prepared by spray pyrolysis, Journal of Ceramic Processing Research 13, 405-408 (2012).

[53] M. Trunec, Effect of grain size on mechanical properties of 3Y-TZP ceramics, Ceramics-Silikáty 52, 165-171 (2008).

[54] L.D. Jadhav, S.H. Pawar, M.G. Chourashiya, Effect of sintering temperature on structural and electrical properties of gadolinium doped ceria (Ce0·9Gd0·1O1·95), Bulletin of Materials Science 30, 97-100 (2007).

[55] R.K. Lenka, T. Mahata, A.K. Tyagi, P.K. Sinha, Influence of grain size on the bulk and grain boundary ion conduction behavior in gadolinia-doped ceria, Solid State Ionics 181, 262-267 (2010).

[56] A. Arabacı, M.F. Öksüzömer, Preparation and characterization of 10 mol% Gd doped CeO2 (GDC) electrolyte for SOFC applications, Ceramics International 38, 6509-6515 (2012).

[57] A.I. Ioffe, M.V. Inozemtsev, A.S. Lipilin, M.V. Perfilev, S.V. Karpachov, Effect of the grain size on the conductivity of high-purity pore-free ceramics Y2O8–ZrO2, Physica Status Solidi (a) 30, 87-95 (1975).

[58] S.P.S. Badwal, J. Drennan, Yttria-zirconia: Effect of microstructure on conductivity, Journal of Materials Science 22, 3231-3239 (1987).

[59] X.J. Chen, K.A. Khor, S.H. Chan, L.G. Yu, Influence of microstructure on the ionic conductivity of yttria-stabilized zirconia electrolyte, Materials Science and Engineering: A 335, 246-252 (2002).

[60] T. van Dijk, A.J. Burggraaf, Grain boundary effects on ionic conductivity in ceramic GdxZr1–xO2–(x/2) solid solutions, Physica Status Solidi (a) 63, 229-240 (1981).

[61] I. Kosacki, T. Suzuki, V. Petrovsky, H.U. Anderson, Electrical conductivity of nanocrystalline ceria and zirconia thin films, Solid State Ionics 136-137, 1225-1233 (2000).

[62] I. Kosacki, H.U. Anderson, Microstructure — Property relationships in nanocrystalline oxide thin films, Ionics 6, 294-311 (2000).

[63] B.G. I. Kosacki, H.U. Anderson, Ionic and Mixed Conductors, Electrochemical Society, Pennington, New Jersey, 1998.

[64] A. Tschöpe, R. Birringer, Grain Size Dependence of Electrical Conductivity in Polycrystalline Cerium Oxide, Journal of Electroceramics 7, 169-177 (2001).

[65] M.C. Martin, M.L. Mecartney, Grain boundary ionic conductivity of yttrium stabilized zirconia as a function of silica content and grain size, Solid State Ionics 161, 67-79 (2003).

[66] X. Guo, Z. Zhang, Grain size dependent grain boundary defect structure: case of doped zirconia, Acta Materialia 51, 2539-2547 (2003).

[67] H.L. Tuller, Ionic conduction in nanocrystalline materials, Solid State Ionics 131, 143-157 (2000).

[68] P. Mondal, A. Klein, W. Jaegermann, H. Hahn, Enhanced specific grain boundary conductivity in nanocrystalline Y2O3-stabilized zirconia, Solid State Ionics 118, 331-339 (1999).

[69] C. Petot, M. Filal, A.D. Rizea, K.H. Westmacott, J.Y. Laval, C. Lacour, R. Ollitrault, Microstructure and ionic conductivity of freeze-dried yttria-doped zirconia, Journal of the European Ceramic Society 18, 1419-1428 (1998).

[70] P. Dahl, I. Kaus, Z. Zhao, M. Johnsson, M. Nygren, K. Wiik, T. Grande, M.A. Einarsrud, Densification and properties of zirconia prepared by three different sintering techniques, Ceramics International 33, 1603-1610 (2007).

[71] K. Hbaieb, Reducing sintering temperature of yttria stabilized zirconia through addition of lithium nitrate and alumina, Ceramics International 38, 4159-4164 (2012).

[72] J.E. Bauerle, Study of solid electrolyte polarization by a complex admittance method, Journal of Physics and Chemistry of Solids 30, 2657-2670 (1969).

[73] J.R. Macdonald, J.A. Garber, Analysis of Impedance and Admittance Data for Solids and Liquids, Journal of The Electrochemical Society 124, 1022-1030 (1977).

[74] C.J. Dias, Determination of a distribution of relaxation frequencies based on experimental relaxational data, Physical Review B 53, 14212-14222 (1996).

[75] J.R. Macdonald, Impedance Spectroscopy: Emphasizing Solid Materials and Systems, John Wiley & Sons, New York, 1987.

[76] J.R. Dygas, Dielectric function of ionic conductors studied by impedance spectroscopy, Solid State Ionics 176, 2065-2078 (2005).

[77] J.R. Macdonald, Dispersed electrical-relaxation response: discrimination between conductive and dielectric relaxation processes, Brazilian Journal of Physics 29, 332-346 (1999).

[78] M.E. Hasnaoui, M.P.F. Gra?a, M.E. Achour, L.s.C. Costa, Electric Modulus Analysis of Carbon Black/Copolymer Composite Materials, Materials Sciences and Applications 2(10), 6 (2011).

[79] M. Lalanne, P. Demont, A. Barnabé, Ac conductivity and dielectric properties of CuFe $1-$ x Cr x O 2 : Mg delafossite, Journal of Physics D: Applied Physics 44, 185401 (2011).

[80] J. Banys, J. Macutkevic, A. Matulis, Determination of the Distribution of the Relaxation Times from Dielectric Spectra, Nonlinear Analysis: Modelling and Control 9, 75-88 (2004).

[81] H. Schichlein, A.C. Müller, M. Voigts, A. Krügel, E. Ivers-Tiffée, Deconvolution of electrochemical impedance spectra for the identification of electrode reaction mechanisms in solid oxide fuel cells, Journal of Applied Electrochemistry 32, 875-882 (2002).

[82] B.A. Boukamp, Fourier transform distribution function of relaxation times; application and limitations, Electrochimica Acta 154, 35-46 (2015).

[83] E. Tuncer, S.M. Gubanski, On dielectric data analysis. Using the Monte Carlo method to obtain relaxation time distribution and comparing non-linear spectral function fits, IEEE Transactions on Dielectrics and Electrical Insulation 8, 310-320 (2001).

[84] A. Bello, E. Laredo, M. Grimau, A. Nogales, T.A. Ezquerra, Relaxation time distribution from time and frequency domain dielectric spectroscopy in poly(aryl ether ether ketone), The Journal of Chemical Physics 113, 863-868 (2000).

[85] A.B. Tesler, D.R. Lewin, S. Baltianski, Y. Tsur, Analyzing results of impedance spectroscopy using novel evolutionary programming techniques, Journal of Electroceramics 24, 245-260 (2010).

[86] A.N. Tikhonov, Regularization of ill-posed problems, DAN SSSR 153, 49-52 (1963).

[87] J.R. MacDonald, Exact and approximate nonlinear least-squares inversion of dielectric relaxation spectra, Chemical Physics 102, 6241-6250 (1995).

[88] J.R. Macdonald, On relaxation-spectrum estimation for decades of data: accuracy and sampling-localization considerations, Inverse Problems 16, 1561 (2000).

[89] E. Tuncer, J.R. Macdonald, Comparison of methods for estimating continuous distributions of relaxation times, Journal of Applied Physics 99, 074106 (2006).

[90] V.A. Stephanovich, E.V. Kirichenko, The physical mechanisms of relaxation times distribution in inorganic and organic disordered ferroelectrics, Journal of Non-Crystalline Solids 353, 4418-4421 (2007).

[91] F. Aslani, L. Sjögren, Relaxation rate distribution from frequency or time dependent data, Chemical Physics 325, 299-312 (2006).

[92] H.E. Atyia, Electrical conductivity and dielectric relaxation of bulk Se70Bi(0, 15) chalcogenide glasses, Journal of Non-Crystalline Solids 391, 83-90 (2014).

[93] A. Mikonis, J. Banys, R. Grigalaitis, A. Matulis, S. Lapinskas, G. Völkel, Determination of the two dimensional distribution of the attempt relaxation times and activation energies from temperature dependence of dielectric dispersion, Central European Journal of Physics 11, 206-212 (2013).

[94] A. Leonide, V. Sonn, A. Weber, E. Ivers-Tiffée, Evaluation and Modeling of the Cell Resistance in Anode-Supported Solid Oxide Fuel Cells, Journal of The Electrochemical Society 155, B36-B41 (2008).

[95] C. Endler-Schuck, A. Leonide, A. Weber, S. Uhlenbruck, F. Tietz, E. Ivers-Tiffée, Performance analysis of mixed ionic–electronic conducting cathodes in anode supported cells, Journal of Power Sources 196, 7257-7262 (2011).

[96] J.P. Schmidt, T. Chrobak, M. Ender, J. Illig, D. Klotz, E. Ivers-Tiffée, Studies on LiFePO4 as cathode material using impedance spectroscopy, Journal of Power Sources 196, 5342-5348 (2011).

[97] J. Illig, M. Ender, T. Chrobak, J.P. Schmidt, D. Klotz, E. Ivers-Tiffée, Separation of Charge Transfer and Contact Resistance in LiFePO4-Cathodes by Impedance Modeling, Journal of The Electrochemical Society 159, A952-A960 (2012).

[98] J.P. Schmidt, P. Berg, M. Schönleber, A. Weber, E. Ivers-Tiffée, The distribution of relaxation times as basis for generalized time-domain models for Li-ion batteries, Journal of Power Sources 221, 70-77 (2013).

[99] J. Hayd, H. Yokokawa, E. Ivers-Tiffée, Hetero-Interfaces at Nanoscaled (La,Sr)CoO3-δ Thin-Film Cathodes Enhancing Oxygen Surface-Exchange Properties, Journal of The Electrochemical Society 160, F351-F359 (2013).

[100] S. Hershkovitz, S. Baltianski, Y. Tsur, Harnessing evolutionary programming for impedance spectroscopy analysis: A case study of mixed ionic-electronic conductors, Solid State Ionics 188, 104-109 (2011).

[101] S. Hershkovitz, S. Baltianski, Y. Tsur, Electrochemical Impedance Analysis of SOFC Cathode Reaction Using Evolutionary Programming, Fuel Cells 12, 77-85 (2012).

[102] F. Ciucci, C. Chen, Analysis of Electrochemical Impedance Spectroscopy Data Using the Distribution of Relaxation Times: A Bayesian and Hierarchical Bayesian Approach, Electrochimica Acta 167, 439-454 (2015).

[103] B.A. Boukamp, Electrochemical impedance spectroscopy in solid state ionics: recent advances, Solid State Ionics 169, 65-73 (2004).

[104] A. Orliukas, P. Bohac, K. Sasaki, L. Gauckler, Relaxation dispersion of ionic conductivity in a Zr0·85Ca0·15O1·85 single crystal, Journal of the European Ceramic Society 12, 87-96 (1993).

[105] A. Orliukas, P. Bohac, K. Sasaki, L.J. Gauckler, The relaxation dispersion of the ionic conductivity in cubic zirconias, Solid State Ionics 72, Part 2, 35-38 (1994).

[106] A. Kežionis, P. Butvilas, T. Šalkus, S. Kazlauskas, D. Petrulionis, T. Žukauskas, E. Kazakevičius, A.F. Orliukas, Four-electrode impedance spectrometer for investigation of solid ion conductors, Review of Scientific Instruments 84, 013902 (2013).

[107] A. Kežionis, E. Kazakevičius, T. Šalkus, A. Orliukas, Broadband high frequency impedance spectrometer with working temperatures up to 1200 K, Solid State Ionics 188, 110-113 (2011).

[108] D.L. Gershon, J.P. Calame, Y. Carmel, T.M. Antonsen, Jr., R.M. Hutcheon, Open-ended coaxial probe for high-temperature and broad-band dielectric measurements, IEEE Transactions on Microwave Theory and Techniques 47, 1640-1648 (1999).

[109] S. Bringhurst, M.F. Iskander, M.J. White, Thin-sample measurements and error analysis of high-temperature coaxial dielectric probes, IEEE Transactions on Microwave Theory and Techniques 45, 2073-2083 (1997).

[110] M. Arai, J.G.P. Binner, and T. E. Cross, Comparison of techniques for measuring high-temperature microwave complex permittivity: measurements for the alumina/zirconia systems, Journal of Microwave Power and Electromagnetic Energy 31, 12-18 (1996).

[111] S. Bringhurst, M.F. Iskander, Open-ended metallized ceramic coaxial probe for high-temperature dielectric properties measurements, IEEE Transactions on Microwave Theory and Techniques 44, 926-935 (1996).

[112] E.L. Y. Zhou, G. Guo, Y. Gao, and T. Yang, Broadband complex permittivity measurement of low loss materials over large temperature ranges by stripline resonator cavity using segmentation calculation method, Progress in Electromagnetics Research 113, 143-160 (2011).

[113] T.A. Baeraky, Microwave Measurements of the Dielectric Properties of Silicon Carbide at High Temperature, Egyptian Journal of Solids 25, 263-273 (2002).

[114] M.N.M. Kehn, L. Shafai, S. Noghanian, Permittivity measurement of disk and annular dielectric samples using coaxial transmission line fixtures. part I: theory and formulation, Canadian Journal of Electrical and Computer Engineering 34, 21-29 (2009).

[115] J. Banys, S. Lapinskas, S. Rudys, S. Greicius, R. Grigalaitis, High Frequency Measurements of Ferroelecrics and Related Materials in Coaxial Line, Ferroelectrics 414, 64-69 (2011).

[116] A. technologies, S-parameter design, Appl. Note AN 154, 14 (2000).

[117] D.D. Macdonald, M. Urquidi-Macdonald, Application of Kramers-Kronig Transforms in the Analysis of Electrochemical Systems: I . Polarization Resistance, Journal of The Electrochemical Society 132, 2316-2319 (1985).

[118] P. Hansen, Regularization Tools version 4.0 for Matlab 7.3, Numerical Algorithms 46, 189-194 (2007).

[119] S. Kazlauskas, A. Kežionis, T. Šalkus, A.F. Orliukas, Electrical properties of YSZ and CaSZ single crystals, Solid State Ionics 231, 37-42 (2013).

[120] S. Kazlauskas, A. Kežionis, T. Šalkus, A.F. Orliukas, Charge carrier relaxation in solid VO•• conductors, Solid State Ionics 262, 593-596 (2014).

[121] S. Kazlauskas, A. Kežionis, T. Šalkus, A. Orliukas, Effect of sintering temperature on electrical properties of gadolinium-doped ceria ceramics, Journal of Materials Science 50, 3246-3251 (2015).

[122] S. Kazlauskas, A. Kežionis, E. Kazakevičius, A.F. Orliukas, Charge carrier relaxation and phase transition in scandium stabilized zirconia ceramics, Electrochimica Acta 134, 176-181 (2014).

[123] A. Kežionis, S. Kazlauskas, D. Petrulionis, A.F. Orliukas, Relationship between charge carrier relaxation and peculiarities of electric response in some solid oxygen ion conductors, Solid State Ionics, accepted 2015-07-12.

[124] S. Kuharuangrong, Ionic conductivity of Sm, Gd, Dy and Er-doped ceria, Journal of Power Sources 171, 506-510 (2007).

[125] T.I. Politova, J.T.S. Irvine, Investigation of scandia–yttria–zirconia system as an electrolyte material for intermediate temperature fuel cells—influence of yttria content in system (Y2O3)x(Sc2O3)(11−x)(ZrO2)89, Solid State Ionics 168, 153-165 (2004).

[126] S.P.S. Badwal, Electrical conductivity of single crystal and polycrystalline yttria-stabilized zirconia, Journal of Materials Science 19, 1767-1776 (1984).

[127] K.L. Ngai, Evidence of interaction between oxygen ions from conductivity relaxation and quasielastic light scattering data of yttria-stabilized zirconia, Philosophical Magazine Part B 77, 187-195 (1998).

[128] S. Ikeda, O. Sakurai, K. Uematsu, N. Mizutani, M. Kato, Electrical conductivity of yttria-stabilized zirconia single crystals, Journal of Materials Science 20, 4593-4600 (1985).

[129] M.B. M. Backhaus-Ricoult, Y. Thibault, Advances in Electronic and Electrochemical Ceramics, John Wiley & Sons, New Jersey, USA, 2006.

[130] A. Pimenov, J. Ullrich, P. Lunkenheimer, A. Loidl, C.H. Rüscher, Ionic conductivity and relaxations in ZrO2–Y2O3 solid solutions, Solid State Ionics 109, 111-118 (1998).

[131] J. Kondoh, H. Shiota, Frequency dispersion of the internal friction in tetragonal and cubic zirconia polycrystals stabilized with yttria, Journal of Materials Science 38, 3689-3694 (2003).

[132] M. Sillassen, P. Eklund, N. Pryds, N. Bonanos, J. Bøttiger, Concentration-dependent ionic conductivity and thermal stability of magnetron-sputtered nanocrystalline scandia-stabilized zirconia, Solid State Ionics 181, 1140-1145 (2010).

[133] P.O.L. Duwez, F. Odell, F.H. Brown, Stabilization of Zirconia with Calcia and Magnesia, Journal of the American Ceramic Society 35, 107-113 (1952).

[134] W.D. Kingery, J. Pappis, M.E. Doty, D.C. Hill, Oxygen Ion Mobility in Cubic Zr0.85Ca0.15O1.85, Journal of the American Ceramic Society 42, 393-398 (1959).

[135] V. Grover, A.K. Tyagi, Phase relations, lattice thermal expansion in CeO2–Gd2O3 system, and stabilization of cubic gadolinia, Materials Research Bulletin 39, 859-866 (2004).

[136] E. Jud, L. Gauckler, The Effect of Cobalt Oxide Addition on the Conductivity of Ce0.9Gd0.1O1.95, Journal of Electroceramics 15, 159-166 (2005).

[137] A.Z. Liu, J.X. Wang, C.R. He, H. Miao, Y. Zhang, W.G. Wang, Synthesis and characterization of Gd0.1Ce0.9O1.95 nanopowder via an acetic–acrylicmethod, Ceramics International 39, 6229-6235 (2013).

[138] K. Maca, J. Cihlar, K. Castkova, O. Zmeskal, H. Hadraba, Sintering of gadolinia-doped ceria prepared by mechanochemical synthesis, Journal of the European Ceramic Society 27, 4345-4348 (2007).

[139] T.H. Hsieh, D.T. Ray, Y.P. Fu, Co-precipitation synthesis and AC conductivity behavior of gadolinium-doped ceria, Ceramics International 39, 7967-7973 (2013).

[140] T. Shimonosono, H. Kimura, Y. Sakka, Effect of grain size on electrical properties of scandia-stabilized zirconia, Journal of the Ceramic Society of Japan 118, 1038-1043 (2010).

[141] P.M. Abdala, A.F. Craievich, D.G. Lamas, Size-dependent phase transitions in nanostructured zirconia-scandia solid solutions, RSC Advances 2, 5205-5213 (2012).

[142] F.S. Howell, R.A. Bose, P.B. Macedo, C.T. Moynihan, Electrical relaxation in a glass-forming molten salt, The Journal of Physical Chemistry 78, 639-648 (1974).

[143] N.H. Perry, T.C. Yeh, T.O. Mason, Temperature Dependence of Effective Grain Core/Single Crystal Dielectric Constants for Acceptor-Doped Oxygen Ion Conductors, Journal of the American Ceramic Society 94, 508-515 (2011).

[144] A.E. Kotp, Effect of Conductive Relaxation on Dielectric Relaxation in Poly (3-hydroxy butyrate) PHB Semi-Crystalline Polymer, International Journal of Basic & Applied Sciences 10, 20-22 (2010).